The Dissertation Committee for Haiyu Huang certifies that this is the approved version of the following dissertation:

Miniaturized Antenna and Transponder Based Wireless Sensors for Internet of Things in Healthcare

Committee:

Deji Akinwande, Supervisor

Ranjit Gharpurey, Co-Supervisor

Dean Neikirk

Ye Hu

Nanshu Lu

Miniaturized Antenna and Transponder Based Wireless Sensors for Internet of Things in Healthcare

by

Haiyu Huang, B.E., M.S.

Dissertation

Presented to the Faculty of the Graduate School of
The University of Texas at Austin
in Partial Fulfillment
of the Requirements
for the Degree of

Doctor of Philosophy

The University of Texas at Austin
December 2014

Dedication

Dedicated to My Parents

Acknowledgements

I would like to express my sincere gratitude to my advisor, Professor Deji Akinwande for his continuing support, encourage, and guidance during my Ph.D. study. The way that he shows me the light in research without restricting me from exploring broader possibilities shapes my doctoral work a truly exciting and enjoyable one. I would also like to thank my Co-advisor, Professor Ranjit Gharpurey, who has helped me building up the important expertise in radio frequency circuit and system for my researches.

Besides advisors from UT, my Ph.D. study has also been supported by my supervisors at the Methodist Hospital Research Institute, and here I would like to specially thank Dr. Tony(Ye) Hu, Dr. Xuewu Liu and Dr. Mauro Ferrari for generously guiding me at healthcare and biomedical side which makes my healthcare application driven interdisciplinary research possible. I would also like to extend my thank to my other committee members Professor Dean Neikirk and Professor Nanshu Lu, for their invaluable suggestions on my overall research work. My gratitude also goes to several other UT professors for useful discussions on my research, including Dr. Hao Ling, Dr. Ray Chen, and Dr. Allen Bard.

This thesis represents the work with collaboration of many scientists. Therefore, I would wish to thank my best friends and colleagues whom I collaborated closely in my research, particularly Dr. Pai-Yen Chen, Dr. Karl Nieman, Dr. Li Tao, Peisen Zhao, Li Ji, Dr. Kristen Parrish, Dr. Jongho Lee, Maryam Mortazavi, Milo Holt, Avinash Nayak, Nassibe Somayyeh Rahimi, Saungeun Park and other members in my research group Sherry Chang, Fahad Chowdhury, Alvin Lee, Ajith Gopalakrishnan, Wei Li, Maruthi Yogeesh, Jason Kim, and Weinan Zhu for their help, as well as their substantial contribution to our collaborative research efforts. I have mentored a UT undergraduate student Germaine Lemo supported by SRA program; here I would thank her for her support to my research during 2013. I also thank J. Wozniak and Texas Advanced Computing Center (TACC) for their help with the 3D illustrative rendering in some of the figures in the dissertation. Outside Texas, my appreciation goes to Professor Ada Poon at Stanford and Dr. Rahul Bhattacharyya at MIT, for their insightful comments and discussion on my research work. Last I would like to thank my whole family, my parents, uncles, aunts, and cousins in China and United States for their care, support and encouragement.

Miniaturized Antenna and Transponder Based Wireless Sensors for Internet of Things in Healthcare

Haiyu Huang, Ph.D.
The University of Texas at Austin, 2014

Supervisor: Deji Akinwande
Co-Supervisor: Ranjit Gharpurey

Future medical and healthcare systems will be largely improved by the wide-spreading of internet of things (IoTs). One of the crucial challenges of IoTs for healthcare is at the wireless sensors. Miniaturization of sensor node profile, minimizing power consumption as well as lowering down design/production cost of antenna, RF circuits and sensor modules have become the key issues for realizing more exciting applications in medical and healthcare fields that never seemed to be possible before.

In this dissertation work, we first focus on electrically small antenna (ESA) design and fabrication for medical telemetry. A comprehensive analysis of the radiation properties of a novel electrically small folded ellipsoidal ESA is presented, showing its ability to self-resonate and impedance match without external components. It will benefit various size-restricted applications especially with wireless medical implants. The second focus is on healthcare sensors using ESA as the sensing agent, which saves the power and cost by eliminating the need of extra sensing modules. Specifically, miniaturized helix ESAs are integrated with drug reservoirs to function as wireless transponder sensors for real-time drug dosage monitoring. We also introduce a system level innovation of a

frequency hopping spread spectrum (FHSS) harmonic transponder and harmonic sniffer based passive wireless sensing system. The μL- liquid level resolution and absolute-accuracy passive sensing is demonstrated in the presence of strong direct coupling, background scatters, distance variance as well as near-filed human body movement interference. Furthermore, we investigate how modern ubiquitous wireless sensor networks could take advantage of sensitive nanostructure materials for enhanced performance. Here we propose a new paradigm of chemically-gated mixed modulation on a single homogeneous graphene device in which the chemical exposure directly modulates an electrical carrier signal. To make the device ubiquitously reusable, a method of precisely tuning the charge neutrality point (V_{cnp}) is introduced by electrochemical calibration with gate voltage pulse sequence. Such chemically gated graphene modulator can be potentially used in a harmonic transponder as a passive ubiquitous sensor node for chemical and bio sensing applications. Overall the research work presented in the dissertation will help enable cost and power-efficient wireless sensor networks in future healthcare IoTs.

Table of Contents

List of Tables

List of Figures

Chapter 1: Introduction

1.1 GLOBAL AGING AND PARADIGM SHIFT IN HEALTHCARE

Computers, internet, wireless technologies combining with advanced micro/nano technologies have already changed the way people communicate and acquire information [1]–[4], and are continuing changing other aspects of the society, for instance, through the term "internet of things" (IoT) [5], [6]. As clearly explained by Kevin Ashton, who first used such phrase in 1999 at a business presentation, "Today computers—and therefore, the Internet—are almost wholly dependent on human beings for information. The problem is, people have limited, time, attention and accuracy—all of which means they are not very good at capturing data about things in the real world"[6], expanding the connectivity of internet to next generation will be empowered by devices that can gather information on their own, without human intervention. In the near future we are expecting to see advancing sensor technologies becomes the focus that efforts of a large variety of fields will shift to.

Although a range of industries such as automobile, home automation, transportation, and security have been significantly impacted by IoT [7]–[11], no field does the IoT offer greater promise to revolutionize than in healthcare [12]–[17]. One major reason is global aging [18]–[20]. Following Japan becoming an elderly dominant country (data shown in Figure 1.1) [21], almost all major countries will experience significant increase in aging population [22], as predicted by the data shown in Figure 1.2. Figure 1.3 shows the median age forecast for different regions of the world [23], which predicts that by 2050 all regions of the world will have median age above 40 years old, except Africa.

Source: National Institute of Population and Social Security Research

Figure 1.1: From pyramid to kite: huge demographic change of Japan from 1950 to 2055 [21].

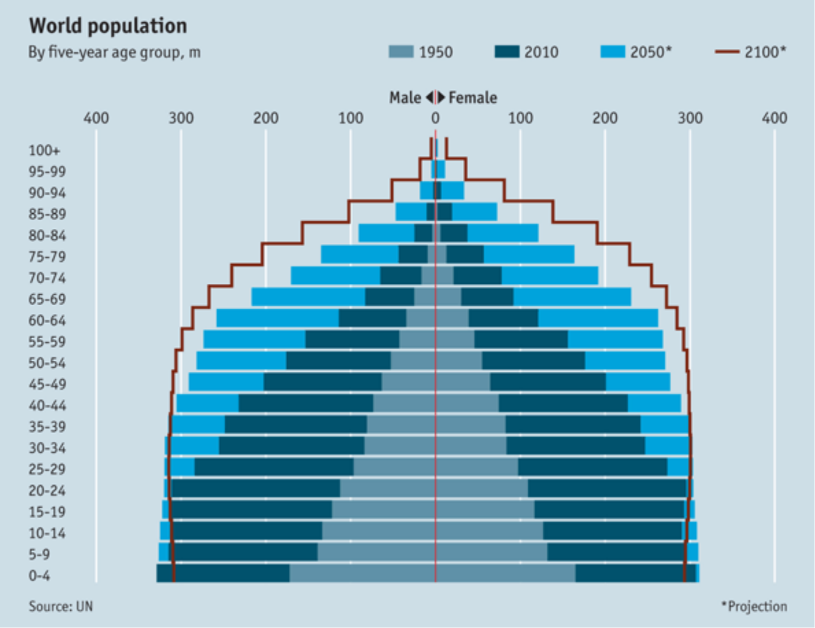

Source: UN

*Projection

Figure 1.2: Population pyramid revealing the trend of global aging [22].

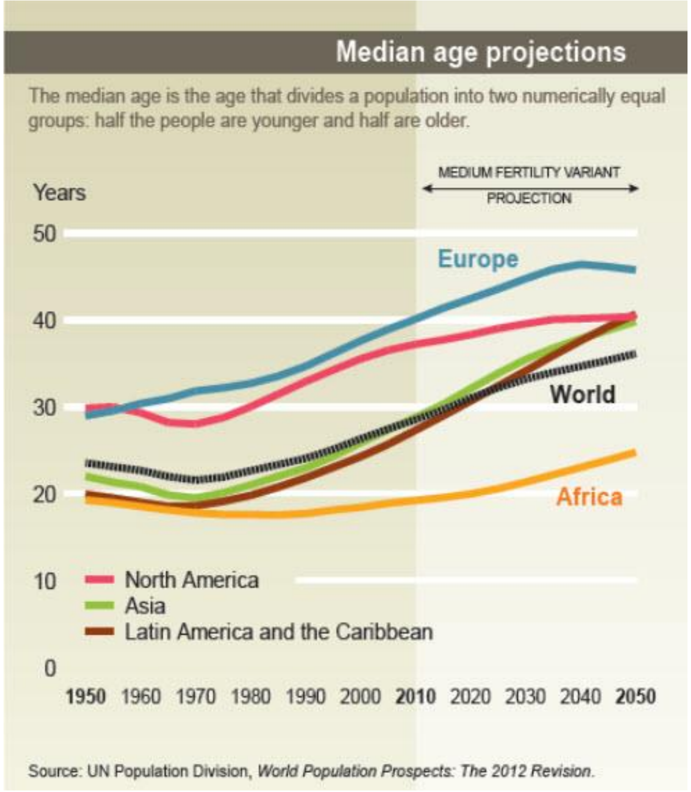

Figure 1.3: The median age forecast for different regions [23]; curves before 2010 are based on actual data.

Such demographic shift will have strong impact on the healthcare infrastructure and facilities. The data shown in Figure 1.4 indicates that higher median age countries have much more hospital beds per capita than lower median age countries [24]; however the number of physicians per capita has less variation from country to country. A very important observation from Figure 1.4 is that, in Mexico, a country with median age of 25.9 [25], one physician is in charge of 0.8 hospital bed on average; by contrast, in Japan, a country with median age of 44.6 [25], one physician needs to take care of 6.5 hospital beds. An aging society unavoidably faces the challenge of high patient-to-care giver ratio in healthcare system. In Japan and some other aging countries, networked infrastructure of nursing home and assisted living systems are very popular there [26], [27]. Normally one such chain nursing home or assisted living cooperation may have nearly 100 branches at locations all over the country [26], [27]. In fact, increasing life expectancy leads to an exploding cost of healthcare; and conventional hospital centered healthcare system is no longer suitable for aging society. Assisted living and nursing home system plays very important roles in decentralizing the burden of aging healthcare from hospitals.

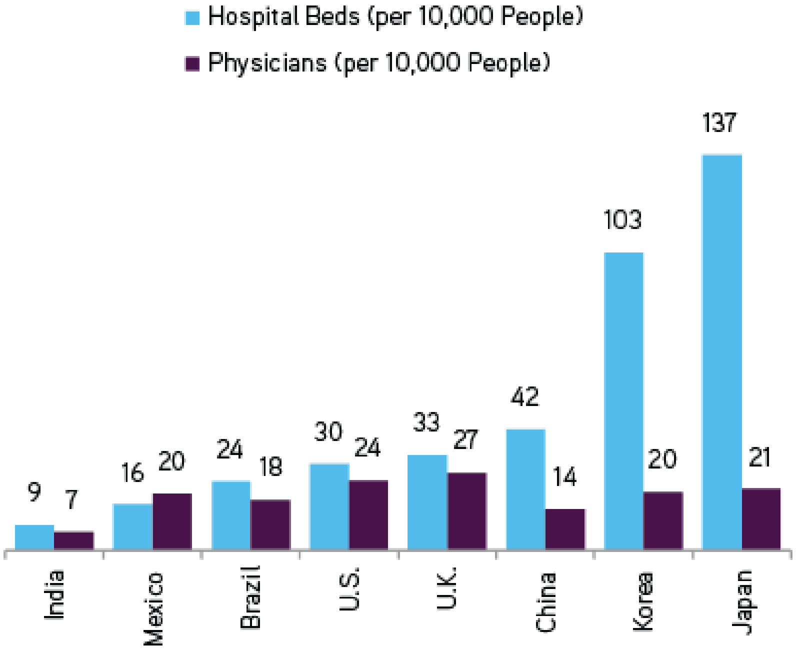

Figure 1.4: Numbers of hospital beds and physicians per 10,000 people in 2010 for countries with different median ages [24] (India median age: 25.9, Mexico: 26.7, Brazil: 28.1, U.S.: 36.9, U.K.: 40.5, China: 35.2, Korea: 37.9, Japan: 44.6) [25].

Although there have been a number of different predictions for future healthcare trends, the general target is undoubtedly to lower down the healthcare cost and utilizing healthcare resources efficiently. A good summary of the recent trends [28] in healthcare is shown in Figure 1.5. Driven by global aging and enabled by healthcare IoTs, healthcare is starting a paradigm shift from hospital centered care to ubiquitous care [28]–[31]. This is just like the shift of telephone booth centered telecommunication to ubiquitous communication driven by mobile cellular phone we have experienced from a decade ago (illustrated in Figure 1.6).

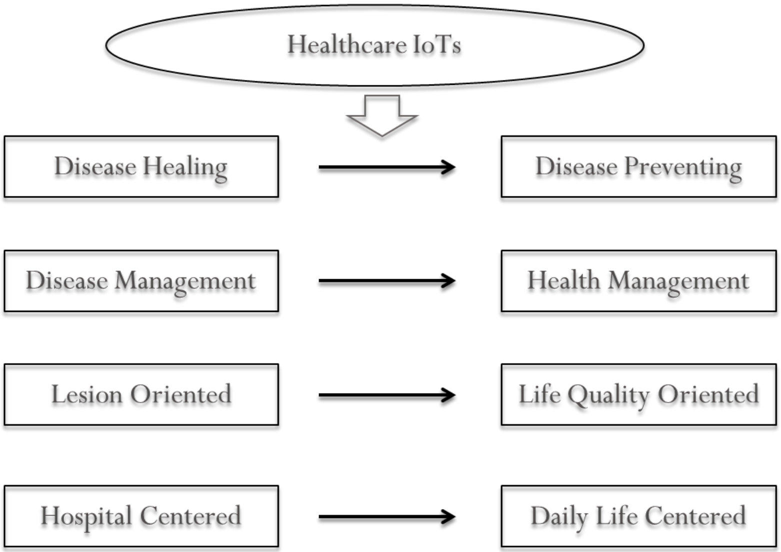

Figure 1.5: Trends in healthcare [28] driven by global aging and enabled by healthcare IoTs.

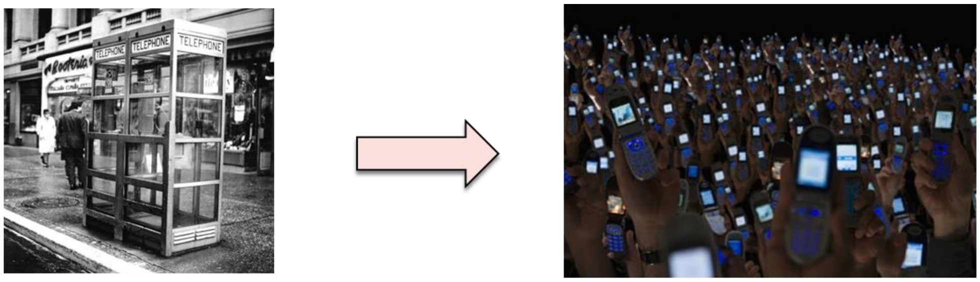

Phone booth centered telecommunication

Ubiquitous telecommunication

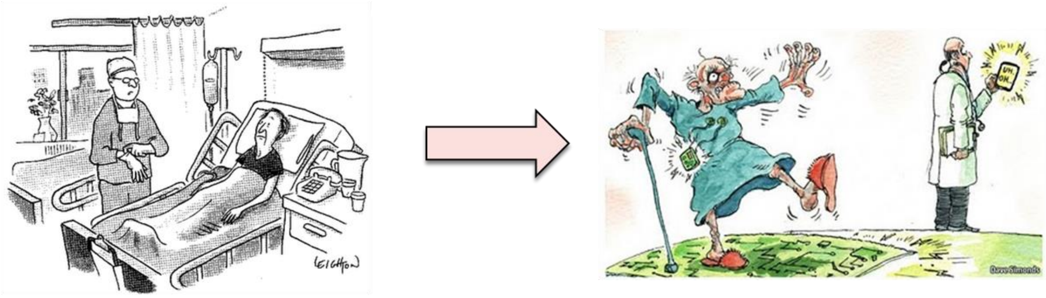

Hospital centered healthcare

Ubiquitous healthcare

Figure 1.6: Paradigm shifts in telecommunication (happened) and healthcare (happening now). Source of images: upper left [32]; upper right [33]; lower left [34]; lower right [35].

Overall, internet of things is an enabling technology. In healthcare it is enabling new terms such as telemedicine, e-hospital, e-health and u-health [28]–[31], [36], [37]. The major market driving force could be aging population, but it does not have impact only on senior people, it will benefit anyone of any age. The paradigm shift toward ubiquitous healthcare is not only made through nursing home chains and assisted living systems, but also though at-home care as well as neighborhood drugstores. Five years ago, hardly anyone went to a drugstore for a flu shot. Today, Walgreen's share of the $10 billion immunization market is 4%, and still fast growing. From a market research survey

[38], there are high percentages of customers prefer convenient care options cost less than the traditional choice: 54.8% of customers prefer to have their skin problem checked remotely by their dermatologists; 42.6% prefer to have a pacemaker or defibrillator checked at home wirelessly by their physicians; 43.6% prefer to have an electrocardiogram at home using a smart phone-linked device with results wirelessly sent to physicians; 41.7% prefer to do urinalysis test at home with a device attached to smartphone; 34.4% prefer to get a MRI at a retail store clinic; 36.7% prefer to have chemotherapy at home; 54.5% prefer to have vital signs checked at home with a device attached to their smartphone; and, very interestingly, 38.6% prefer to have a live visit with a physician via an app on their smartphone. There is about 100 billion dollar emerging market associated with the consumer migration to more affordable and convenient care options [38].

1.2 MINIATURIZED WIRELESS SENSORS FOR UBIQUITOUS HEALTHCARE

A key feature of healthcare IoT is ubiquitous wireless monitoring [29], [39]. As global demographic trend of aging will result in increasing healthcare work force shortage [40], [41], electronic healthcare monitoring is gradually taking over the role of human-based observation on both diagnostic and therapeutic sides [42]–[47]. It is predicted that wireless networked sensors with not only high sensitivity, but also small size, low power and minimum cost (in fabrication, deployment and maintenance) will receive growing popularity in healthcare industry [46], [48]. Currently healthcare workers spend more than half of their time on collecting and managing healthcare data, while pervasive sensing platform will free up doctors and nurses to spend more time on resolving critical patient care problems and less time on fetching information.

In order to build up the ubiquitous wireless sensor based monitoring platform for healthcare, challenges exist in both software and hardware sides. On the software side, how to turn the big data collected from the huge amount of networked sensors into clinical insight, and turn such insight into conclusion, becomes a major problem. Big data analytics is now a key factor toward healthcare IoT, as the U.S. healthcare data will soon reach the zettabyte (10^{21} gigabytes) scale and, not long after, the yottabyte (10^{24} gigabytes) [49]. The electronic health data sets become so large and complex that they are no longer possible to manage with traditional software [49]. On the hardware side, it is important to develop miniaturized sensors, antennas as well as power efficient wireless communication circuits and systems that are compatible with healthcare IoT. However, existing technologies are still far from sufficient to fit in the needs of future ubiquitous healthcare. As many companies in semiconductor and communication industries have recently proposed some high-level infrastructures [50]–[52] for healthcare IoT (two examples are shown in Figure 1.7), abundant innovation opportunities are brought out at device, circuit and system levels for variant applications. And that is the general motivation of the researches in this dissertation work.

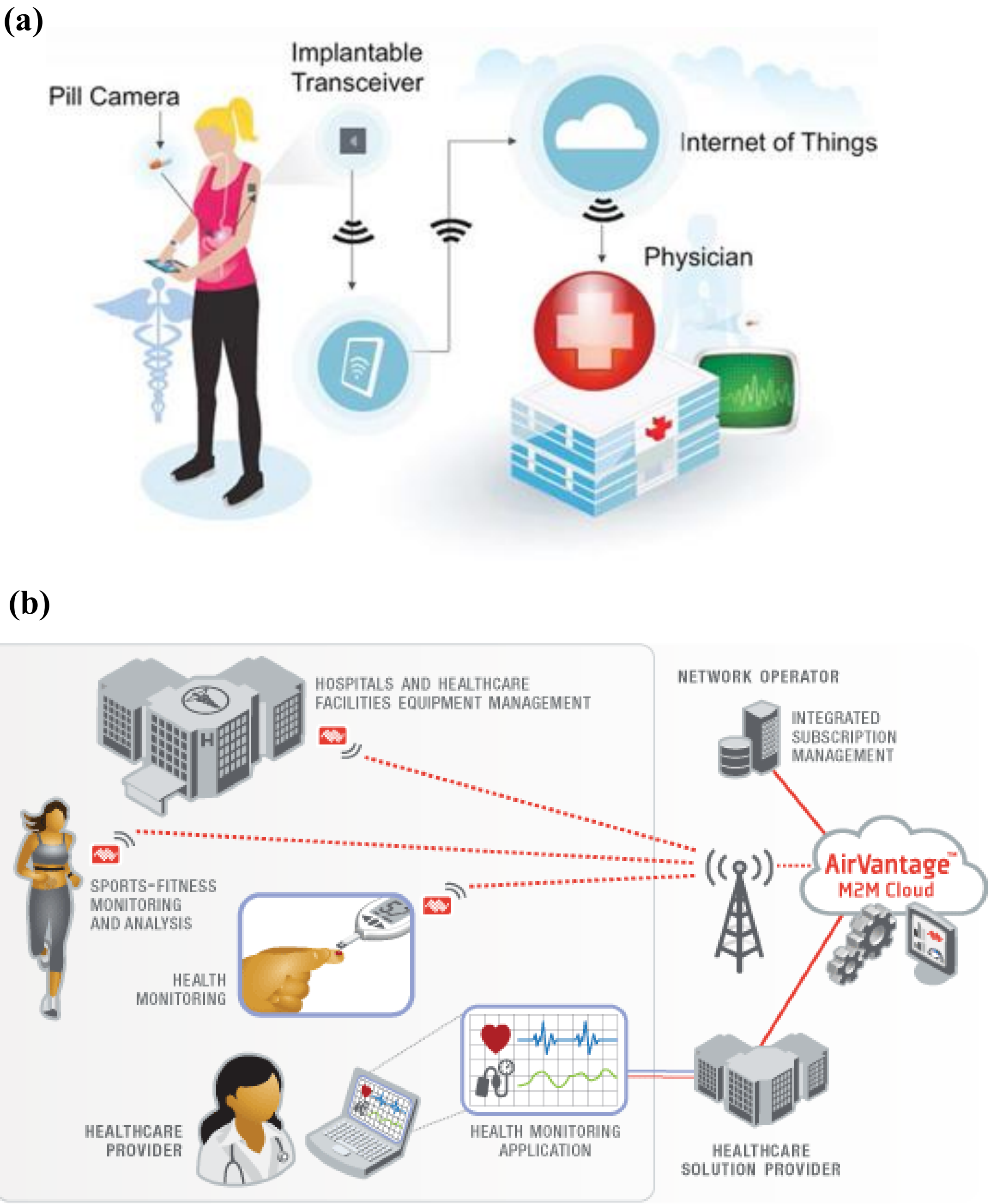

Figure 1.7: Examples of hardware infrastructures for healthcare internet of things proposed by companies from industries: (a) by Freescale Semiconductor [51], [52]; (b) by Sierra Wireless [50].

In this dissertation we describe the author's contributions to several aspects of ubiquitous wireless monitoring (mostly on the hardware side) for healthcare IoT. First novel design and fabrication of a 3-dimensional (3-D) electrical small antenna (ESA) is motivated by the special demands of wireless medical implants. Second a concept of using 3-D ESA is proposed based on the needs of wireless liquid level monitoring in healthcare. Furthermore, a new sensing and communication system utilizing a 3-D ESA equipped harmonic transponder is proposed, whose passive and low cost feature could be a key factor for populating the IoT based healthcare monitoring. Last but not least, a nanomaterial graphene based chemical modulation device is realized with the potential to be used as a chemical or bio sensor, which can be integrated with the harmonic transponder as a passive wirelessly networked sensor. All these subjects involved in this dissertation work, may altogether support the development of a cost effective and energy efficient wireless sensor platform for ubiquitous healthcare IoT.

1.3 OUTLINE

This dissertation report is organized as follows. In Chapter 2, in order to serve medical implant applications, we present the design and fabrication of a folded ellipsoidal helix ESA that affords improved tunability and design flexibility in matching and tailoring of its radiation properties compared to the conventional folded spherical ESA. A full simulation is performed to explore more generalized folded ellipsoidal helix geometries, and the radiation properties of these antennas are characterized with different sets of design parameters. In addition, we present a technique to tune the antenna feed-point resistance, while at the same time preserving a moderate bandwidth. We demonstrate three antennas with quite different volumes and shapes. Each is designed to work at the 2.4 GHz ISM band with input impedance of 50 Ω. The proposed antenna manufacturing method is a cost-effective and reliable selective laser sintering (SLS) based molding process, enabling massively and accurately fabricating folded wire or patch antennas with complicated geometries, such as the ellipsoidal designs. For the pacemaker antennas, we also explore a possible approach of designing a dual band electrically small ellipsoidal helix antenna by utilizing a non-uniform pitch structure.

In Chapter 3, we introduce a cost effective wireless drug dosage monitoring approach utilizing a miniaturized antenna sensor encapsulated within some biocompatible package as a fully assembled drug storage and delivery unit. The concept is using a three-dimensional helix antenna as a sensor to enable wireless monitoring of liquid volume. The general design procedure of this type of antenna sensor is proposed based on electromagnetic theory and finite element simulation. A cost effective fabrication process is utilized to encapsulate the antenna sensor within a biocompatible package layer using PDMS material, and at the same time form a drug storage or drug delivery unit inside the sensor. The in vitro experiment on two prototypes of antenna sensor-drug reservoir assembly have shown the ability to monitor the drug dosage by tracking antenna resonant frequency shift from 2.4-2.5-GHz ISM band with realized sensitivity of 1.27 μ l/MHz for transdermal drug delivery monitoring and 2.76- μl/MHz sensitivity for implanted drug delivery monitoring.

In Chapter 4, extending the work in Chapter 3, we propose a new sensing mechanism utilizing harmonic transponder with metamaterial-inspired compact antenna sensor to realize passive absolute high resolution wireless liquid-level monitoring. In our conceptual demonstration, the harmonic transponder comprises of a nonlinear frequency multiplier connected to two anennae, one of which is a metamaterial-inspired 3-D antenna designed to be sensitive to the liquid-level within a confined region. An interrogator transmits frequency-hopped 902-928 MHz UHF radio-frequency identification (RFID) signal to the transponder, and a sniffer receiver detects the harmonic signal and decodes its signal strength array at 1.804-1.856 GHz from the transponder. A 0.4 μL resolution absolute accuracy passive wireless liquid-level sensing is realized even in the presence of strong direct coupling, background scatters, distance variance as well as near-field human body movement interference. The concept of harmonic transponder, along with its sensing system with harmonic sniffer, enables highly efficient wirelessly networked passive monitoring in healthcare and other industrial applications.

In Chapter 5, we investigate how sensitive nanostructure materials could contribute to ubiquitous sensor networks in healthcare. Specifically, we report a new paradigm of chemically-gated mixed modulation on a single homogeneous graphene device in which the chemical exposure directly modulates an electrical carrier signal. To make the device ubiquitously reusable, a method of precisely tuning the charge neutrality point (V_{cnp}) is introduced by electrochemical calibration with gate voltage pulse sequence, which overcomes the inconvenience of conventional high temperature/high vacuum approaches. The experimental demonstration of graphene chemically-gated modulation along with its V_{cnp} calibration is realized through an example of air exposure-ethanol treatment modulation cycle on a photolithography-free large area graphene field effect transistor. Beyond that, we design a passive sensitive frequency multiplier consisting of four graphene chemically-gated modulation devices. Such nanomaterial frequency multiplier can be integrated with the harmonic transponder sensing system described in Chapter 4. It has promising potential for this chemically gated mixed modulation along with precise and convenient control of V_{cnp} to enable nanomaterial chemically sensitive modulation blocks for nanosensor networks in ubiquitous healthcare IoT.

In Chapter 6, we summarize our accomplishments and highlights conclusions drawn from our work, with suggestions for furthering these results and efforts.

Chapter 2: Electrically Small Antennas for Healthcare Applications[1]

2.1 ANTENNA DESIGN AND FABRICATION CHALLENGES IN HEALTHCARE TELEMETRY

The demand of miniaturization of wireless healthcare telemetry devices has driven a continual downsizing of antennas [53], [54]. Medical telemetry, especially for those devices implanted inside the human body or under the skin, often budget the amount of antenna volume for a given application on an ad hoc basis rather than through the use of electromagnetic analysis. Frequently the volume is driven by customer convenience and is small enough that performance trade-offs are inherent in the antenna solution. Many times the volume allotted may be such that only an electrically small antenna (ESA) can be used in the application. Early in a design cycle it is important to determine if the physical volume and geometry specified are, in theory, large enough electrically to allow the design of any antenna which can meet the impedance bandwidth requirements specified. There is a fundamental theoretical limit to the bandwidth and radiation efficiency of electrically small antennas. Attempting to circumvent these theoretical limits can divert resources in an unproductive manner to tackle a problem which is insurmountable [55].

---

[1] A large portion of the materials in this chapter were based on the following publications, to which all the co-authors have contributions:
H. Huang, K. Nieman, Y. Hu, D. Akinwande, "Electrically Small Folded Ellipsoidal Helix Antenna for Medical Implant Applications", *Proc. IEEE International Symposium on Antennas and Propagation (APS)*, pp. 769 - 771, Spokane, WA, July 2011
H. Huang, K. Nieman, P. Y. Chen, M. Ferrari, Y. Hu, D. Akinwande, "Properties and Applications of Electrically Small Folded Ellipsoidal Helix Antenna", *IEEE Antennas and Wireless Propagation Letters*. vol. 11, pp. 678 – 681, 2012
H. Huang, P.Y. Chen, M. Ferrari, Y. Hu, D. Akinwande, "Dual Band Electrically Small Non-Uniform Pitch Ellipsoidal Helix Antenna for Cardiac Pacemakers", *IEEE Radio & Wireless Symposium*, Austin, TX, Jan. 2013

For an electrically small antenna, an antenna whose largest dimension is less than one-tenth of its operating wavelength, it has an inherent minimum value of Q governed by the minimum spherical volume that contains the antenna [55]–[58]. This minimum Q places a limitation on the attainable impedance bandwidth of an electrically small antenna, as its bandwidth decreases as the third power of the radius of this spherical volume. Considering such performance limitation, it is preferred for an antenna to occupy as much of the volume as possible to provide higher bandwidth. A well-known example in the personal communication is the iPhone 4 antenna, which uses a stainless steel band around the perimeter of the handset as part of the antenna structure in order to provide improved reception over the internal antenna in the iPhone 3GS [59]. The trend is that, for size-restricted applications such as medical implants, the antenna is preferred to be three-dimensional which is more suitable to be packaged around the device comparing to two-dimensional planar antenna. As illustrated in Figure 2.1, the 3-D ESAs are more energy efficient choice over 2-D ESAs as the antenna geometry is constrained by the device associated with the ESA [60], [61]. Although 2-D planar antenna is less expensive to fabricate, in medical application, especially in medical implants, surgery and maintenance cost are dominant over the device cost itself. Energy efficiency and battery life time are more crucial factors to determine the overall cost. In addition, as 3-D printing and manufacturing techniques become matured and affordable nowadays [62], it is predictable that for wireless medical implants in future healthcare IoT, 3-D electrically small antenna design will be a key technology to support variant applications.

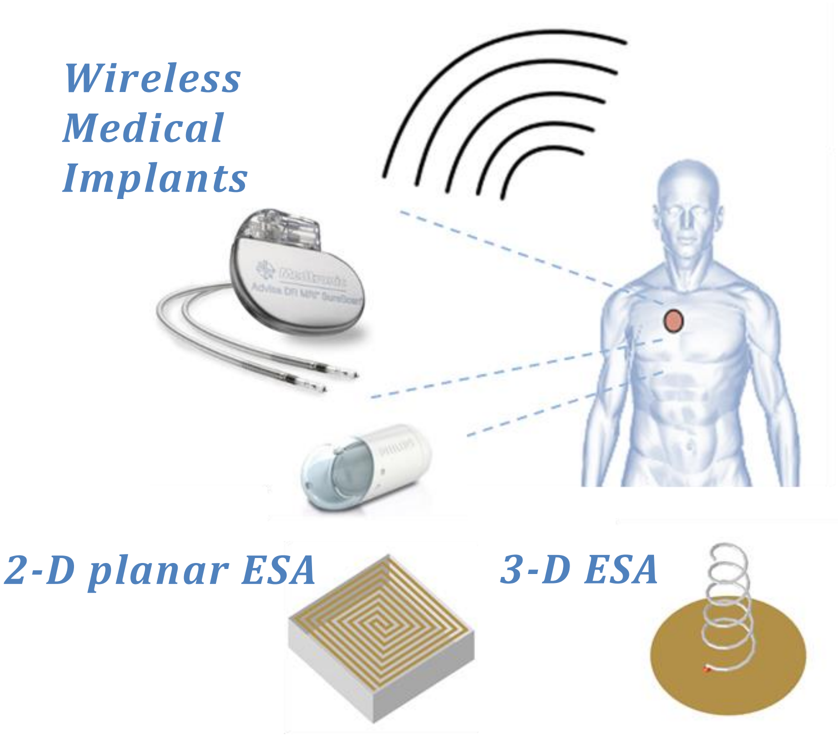

Figure 2.1: 3-D electrically small antenna is more suitable than 2-D planar antenna for wireless medical implant applications.

As most emerging wireless applications involve frequency higher than 300MHz and device size below 10 cm, the optimization of electrically small antenna is of high interest. Several different structures such as disk-loaded monopole, multi-armed spiral, folded design and also genetic algorithm design have been carried out to increase the bandwidth of electrically small antennas [63]–[67], which is limited by causality and passivity. Among them the electrically small spherical helix antenna is one of the most efficient designs to reach the theoretical bandwidth upper bound of an electrically small antenna. To utilize the spherical helix antenna for medical telemetry applications, however, there are three issues that need to be addressed. First, the shape of spherical helix antenna is always a sphere, thus it is incompatible to integrate with a medical telemetry device especially the implanted device, whose size and geometry is highly dependent on the surrounding environment. Second, tuning the antenna to self-resonance and matched impedance is essential because additional matching network will occupy a significant portion of volume, while the feed-point resistance of a spherical helix antenna is hardly controllable. The third issue is how to mass-produce such three dimensional antennas, as most of the matured miniaturized antenna manufacturing process are for flat and printed patch antennas. Innovations in novel cost-effective fabrication techniques for high performance dimensional electrically small antennas are the key to push advanced wireless medical telemetry to the future healthcare industry.

Besides the general challenges of medical telemetry antenna, different applications may have their own specific challenge in the antenna. For example, in modern artificial cardiac pacemakers, both wireless data transmission for cardiac pattern sensing and RF coupling for remotely rechargeable batteries are strongly desired [68]. For the cardiac data transmission 2.4~2.5GHz ISM band is usually used while for wireless power transmission, it has been shown that 1 GHz is the optimal frequency considering the through a dispersive dielectric of human body tissue [69]. Therefore the pacemaker application can be benefited from a multi-band antenna design.

The last but not the least challenge in the medical telemetry antenna development is the electromagnetic near-field interaction between the antenna and the human body. Such interaction has obvious impact on antenna performance when the antenna is implanted deeply inside human body, or placed in a body fluid surrounded environment. During antenna design and simulation, all the external objects need to be taken into consideration in order to compensate all the interactions and get accurate simulation results and hence get the correct antenna design parameters [54].

2.2 THEORY AND PRIOR WORK OF ELECTRICALLY SMALL ANTENNA

An electrically small antenna is defined as one whose maximum dimension, or in other words, the radius of the sphere enclosing the maximum dimension of the antenna, is less than λ/2π [55]. Where λ is the operating wavelength of the antenna in free space. It has been established that for an electrically small antenna, contained within a given volume, the antenna has an inherent minimum value of Q. This places a limit on the attainable impedance bandwidth of an electrically small antenna. The higher the antenna Q the smaller the impedance bandwidth. The minimum Q for an electrically small linearly polarized antenna in free space is expressed as [56]:

$$Q_L = \left(\frac{\lambda}{2\pi a}\right)^3 + \frac{\lambda}{2\pi a} \tag{1}$$

The minimum Q for an electrically small circularly polarized antenna in free space is expressed as [56]:

$$Q_{CP} = \frac{1}{2}\left(\frac{\lambda}{2\pi a}\right)^3 + \frac{\lambda}{2\pi a} \tag{2}$$

Equations (1) and (2) assume a perfect lossless matching network. However, in practice, external matching components will bring significant insertion loss and will occupy significant volume in the whole wireless transmission device. For space limited applications like medical telemetry, self-impedance matching is desired to eliminate bulky external matching components. However, the electrically small folded spherical helix antenna, which is recognized as one of the optimal antenna design to reach the theoretical electrically small antenna bandwidth, has its own limits in realizing arbitrary antenna feed impedance to match the device without any matching networks [67]. In this chapter an electrically small folded ellipsoidal helix antenna (EHA), which can be considered as an alternative form of electrically small folded spherical helix antenna, is introduced to address such issue.

2.3 ELECTRICALLY SMALL ELLIPSOIDAL ANTENNA AND ITS MEDICAL APPLICATIONS

A standard ellipsoid body in Cartesian coordinate system can be represented as

$$\frac{x^2}{a^2}+\frac{y^2}{b^2}+\frac{z^2}{c^2}=1 \tag{3}$$

where *a, b, c* are respectively the equatorial radius along the *x*, y, z axes. For convenience here we define Y aspect ratio *YAR=b/a* and Z aspect ratio *ZAR=c/a*.

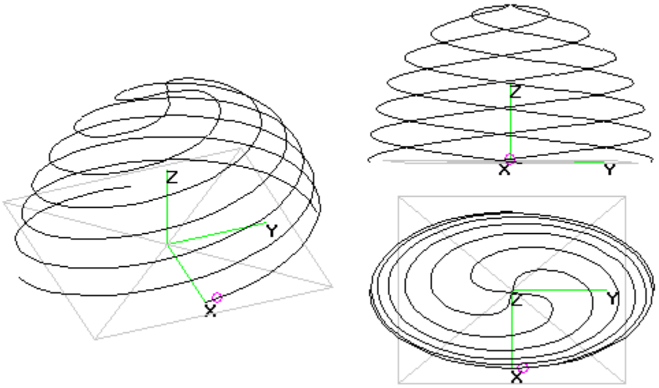

Figure 2.2: An example of a 4 arm, 1.5 turn EHA with *YAR*=1.5 and *ZAR*=2.

Figure 2.2 depicts the structure of a folded EHA. When *YAR*=1 and *ZAR*=1, the geometry degenerates to a spherical helix [67]. To model a *k*-turn, *M*-arm folded ellipsoidal helix antenna using the open source numerical electromagnetic code (NEC) [70], we divide each helical arm into *N* wires (*N*=60 is chosen) of uniform displacement in the *z* axis, and Matlab is used to conveniently generate the NEC input file. The overall design and verification procedure is shown in Figure 2.3. The coordinates of the n^{th} wire section in the m^{th} arm $(x_{m,n}, y_{m,n}, z_{m,n})$ can be expressed as:

$$x_{m,n} = a \sin\delta_n \sin\phi_{m,n} \tag{4}$$

$$y_{m,n} = YAR \cdot a \sin\delta_n \cos\phi_{m,n} \tag{5}$$

$$z_{m,n} = ZAR \cdot a \cos\delta_n \tag{6}$$

where

$$\delta_n = \cos^{-1}\frac{n}{N} \tag{7}$$

$$\phi_{m,n} = 2\pi k\frac{n}{N} + 2\pi\frac{m}{M} \tag{8}$$

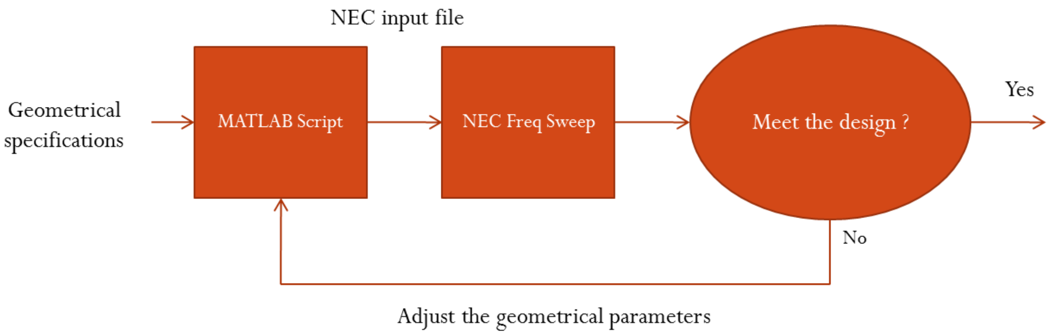

Simulation Parameter	**Value**
Wire diameter (cm)	0.1
Wire conductivity (S/m)	$5.8 \bullet 10^7$
Number of segments ***N***	60 • # *of arms*

Figure 2.3: The fast antenna design and verification process using Matlab and NEC.

Using the model described above, the antenna radiation properties can be simulated. Here we fix the number of arm (*M*) to 4, choosing *k*=1, *a*=1 cm, *YAR*=1, *ZAR*=1 as their initial values, and evaluate the effects of each parameter on the antenna's resonant characteristics. First the limitation of electrically small folded spherical helix antenna [67] is investigated through simulation. Table 2.1 shows the antenna input resistance variation when number of arms changes, with *a* adjustable to ensure zero antenna input reactance at 2 GHz. On the other hand, table 2.2 shows the antenna input resistance variation when number of turns changes, again with *a* adjustable to ensure zero antenna input reactance at 2 GHz. From these two sets of simulation, we can see that if under size compatibility restriction, electrically small spherical helix antenna cannot have flexible impedance tuning and achieve perfect matching. Even without size compatibility restriction, the spherical helix antenna can achieve perfect matching, but have to undergo complicated parameter tuning procedure on number of arms, number of turns and antenna size *a* altogether. And that is the major reason the electrically small folded ellipsoidal helix antenna is introduced here. From the simulation shown in Table 2.3, in which the antenna input resistance variation when *ZAR* changes with *a* adjustable to ensure zero antenna input reactance at 2 GHz. it can be noticed that *a* is almost within a variation of 2%, indicating that *ZAR* may tune the matching condition without affect the resonant frequency. Comparing to the results in Table 2.1 and Table 2.2, the folded ellipsoidal helix antenna is more suitable than its spherical helix counterpart for size restricted design.

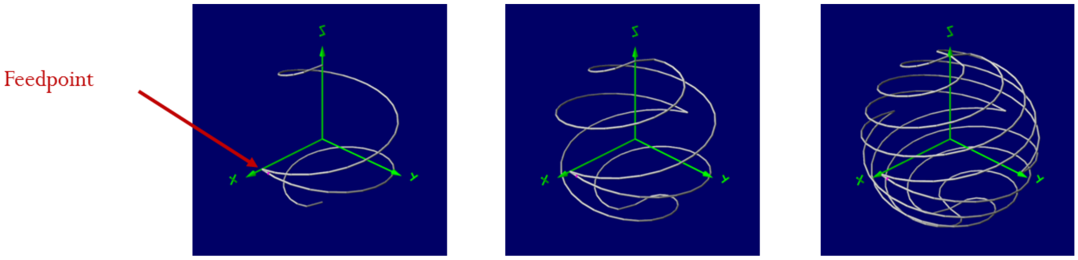

# of turns	1	1	**1**
# of arms	1	2	**4**
a (cm)	0.80	0.85	**0.91**
$2\pi a/\lambda$	0.338	0.359	**0.384**
Z_{in} (Ω)	3.82 + j0.11	16.8 – j0.08	**83.1 - j0.25**
BW(MHz/MHz)	22/2017.5 = **1.1%**	40/2017.5 = **2.0%**	**64/2017.5 = 3.2%**
Rad. Eff.	88.04%	88.71%	**89.07%**

Table 2.1: Comparison of simulated antenna performance (using NEC) of folded spherical helix antenna with different number of arms (Fixing number of turns *k*, varying number of arms *M* and *a* to ensure a zero imaginary part in antenna input impedance at 2 GHz)

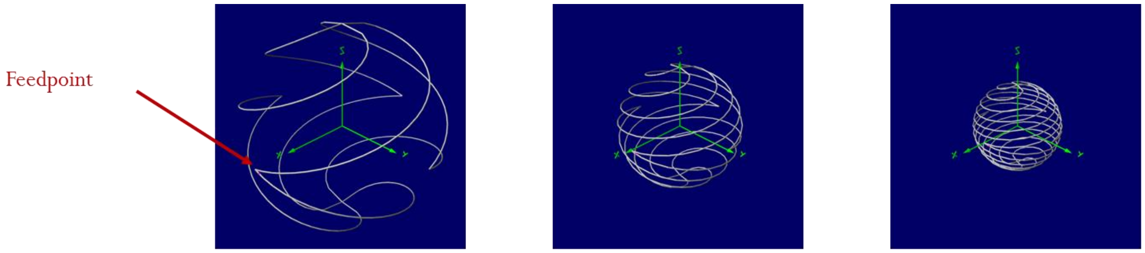

# *of turns*	0.5	**1**	1.5
# *of arms*	4	**4**	4
a (cm)	1.47	**0.91**	0.65
$2\pi a/\lambda$	0.62	**0.384**	0.275
Z_{in} (Ω)	210 - j0.67	**83.1 - j0.25**	46.9 - j0.94
BW (MHz/MHz)	212/2017.5 = **10.5%**	**64/2017.5 = 3.2%**	27/2017.5 = **1.3%**
Rad. Eff.	89.19%	**89.07%**	90.42%

Table 2.2: Comparison of simulated antenna performance (using NEC) of folded spherical helix antenna with different number of turns (Fixing number of arms *M*, varying number of turns *k* and *a* to ensure a zero imaginary part in antenna input impedance at 2 GHz)

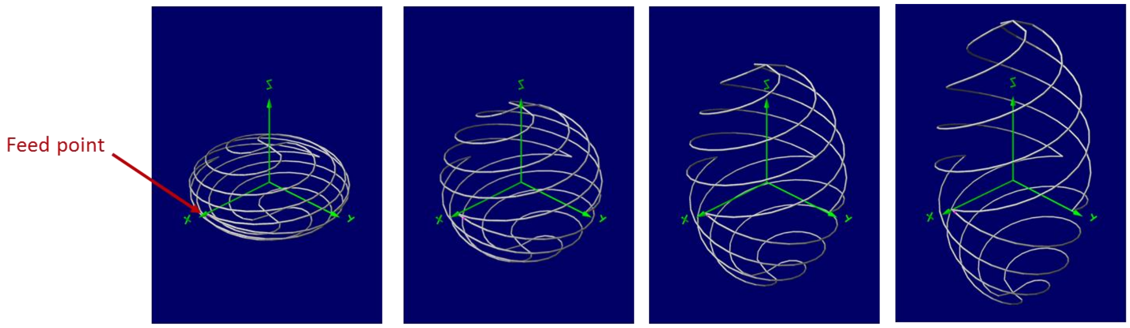

# of turns	1	**1**	1	1
# of arms	4	**4**	4	4
a (cm)	0.90	**0.91**	0.89	0.87
c (cm)	0.45	**0.91**	1.34	1.73
ZAR (*c:a*)	0.5:1	**1:1 (Spherical Helix)**	1.5:1	2:1
k *max {*a*, *c* }	0.380	**0.384**	0.566	0.731
Z_{in} (Ω)	18.5 + j0.35	**83.1 - j0.25**	188 + j0.21	338 + j0.58
BW (MHz/MHz)	20/2017.5 = **1.0%**	**64/2017.5 = 3.2%**	135/2017.5 = **6.7%**	217/2017.5 = **10.8%**
Rad. Eff.	100.00%	**89.07%**	87.59%	87.70%

Table 2.3: Comparison of simulated antenna performance (using NEC) of folded ellipsoidal helix antenna with different Z aspect ratio ZAR (Fixing number of arms *M*, number of turns *k*, varying *c* and *a* to ensure a zero imaginary part in antenna input impedance at 2 GHz)

A more detailed antenna impedance simulation is included in Figures 2.4 (a)-(d) with different parameter sets. Figure 2.4 (a) shows that as the number of turns increases, the resonance of the antenna, of which the net reactance is zero ($X = 0$), will shift to lower frequencies. However, the antenna resistance *R* at resonance will decrease as well. Note that there are two zero net reactance points; however we are only interested in the first, higher bandwidth resonant point accompanied with a reasonable resistance. If the design goal is an antenna operating at 2.40 GHz in a 50 Ω system, it is impossible to realize it by changing only the number of turns of the spherical helix. Therefore, another tuning parameter, either *a*, *YAR*, or *ZAR* is needed for compensating the resistance dependency. Figure 2.4 (b) shows that when fixing the values of all other parameters, both the resonant frequency and the input resistance will be shifted by varying the antenna radius *a*. As a result, it is practically difficult to design a spherical helix antenna with the desired size and frequency of operation, due to the poor matching of the real part of impedance. In this scenario, additional transformers, such as shunted stubs or quarter wavelength stubs, must be used to achieve a good matching between the feed probe and the loaded antenna over a finite bandwidth. However, this could increase the total volume, the fabrication complexity, and the circuit integration for a small antenna enclosing active and passive devices.

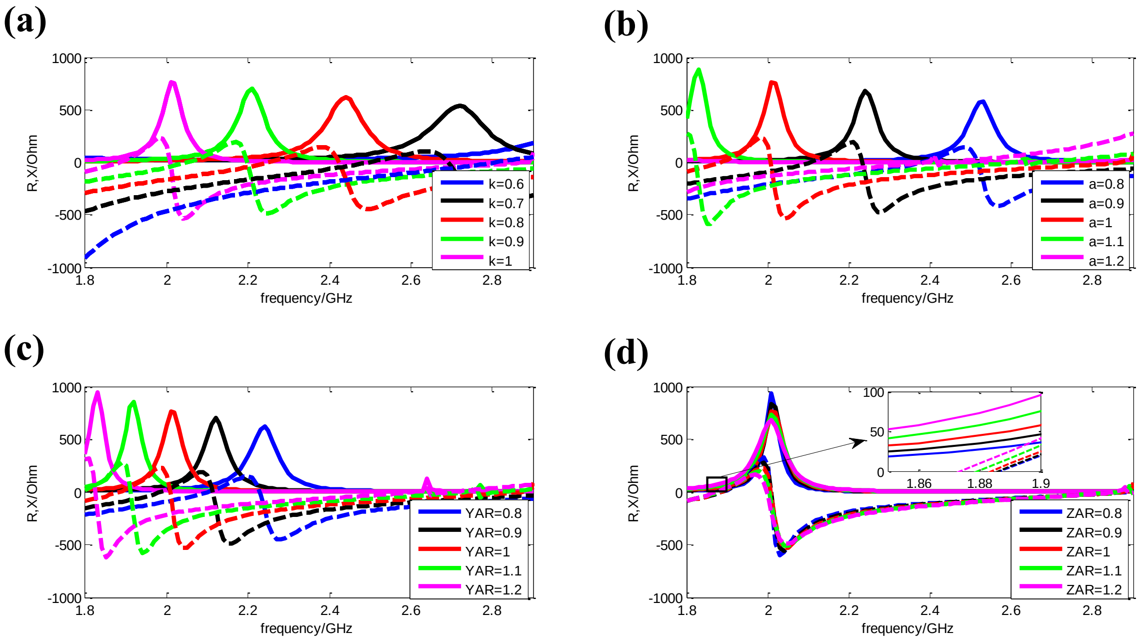

Figure 2.4: NEC simulation of the input impedance of folded EHA with varying design parameters: (a) number of turns k; (b) elliptic radius: a/cm; (c) Y aspect ratio *YAR*; (d) Z aspect ratio: *ZAR* ; here solid line and dashed line represent the real and imaginary part of input impedance, respectively.

In order to improve the poor matching properties of an electrically small 3-D spherical helix antenna, additional design degrees of freedom should be introduced. Here an ellipsoidal helix with more design flexibility, i.e. *ZAR* and *YAR*, may be a promising design. Figures 2.4(c) and (d) show the effect of *YAR* and *ZAR* on the antenna impedance. We notice from Figure 2.4(d) that *ZAR* has a special property that only changes the resistance without substantially affecting the reactance curve and the resonant frequency. This is because the effective inductance *L* and capacitance *C* of the folded EHA always ensure that the LC product is approximately a constant regardless of the relatively wide variations in ZAR. This property enables a self-tunable antenna impedance matching method without any external passive component. In practice, the designer can first tune the antenna resonant frequency by choosing a design parameter set of M, k, a, YAR, and then consider the impedance matching by tuning ZAR. For size restricted applications, a and YAR are first determined by the geometry and shape of the device and package, and a (M, k, ZAR) parameter combination can be optimized to obtain the best antenna performance.

Following the design procedure mentioned above, three antennas with different size restrictions were designed, as summarized in Table 2.4. In Design I and II, YAR=1, and the radius a is set to 5mm and 10mm, respectively, while Design III is geometrically restricted by a realistic pacemaker, as a more practical example. All the three antennas are designed to be operated at the 2.4GHz ISM band, and their antenna impedance are all matched to the 50 Ω system. The 3dB bandwidths of these three antennas are 95MHz, 200MHz and 195 MHz, respectively. The translated Q factors of design I and II are close to their theoretical limits for electrically small antennas due to passivity and causality [55]–[58]. We note that for design III, the antenna size is relatively large (with an electric size close to λ/10, where λ is the wavelength of operation) such that it is almost out of the electrically small region.

	Design I	Design II	Design III
a/mm	5	10	17.5
# of arms	4	4	2
# of turns	1.77	0.747	1.65
YAR	1	1	2.6
ZAR	1.43	0.82	3.28
Zin/Ω	48.8+ j0.25	48.1+ j0.38	51.5- j1.09
BW(MHz/MHz)	95/2400= 3.96%	200/2400= 8.7%	195/2450= 7.96%
Rad. Eff.	99.91%	99.93%	99.74%

Table 2.4: Summary of the parameters and simulated performance (using NEC) of the three EHA designs.

2.4 ELECTRICALLY SMALL ANTENNA FABRICATION USING SELECTIVE LASER SINTERING

Selective laser sintering (SLS) is a rapid and low cost 3-D prototyping method invented at the University of Texas [71], [72]. A high power laser is used to fuse small polyamide particles into a mass that has the desired 3-D shape. Taking advantage of SLS, a template with the desired 3-D antenna structure can be fabricated at a resolution of ~ 0.5 mm. Based on the antenna template, the metal antenna structure can be transferred through a number of different ways. In this demonstration, we taped out a template with grooved curves, and then filled in the copper wire in the grooves. The template can be released immediately after the whole antenna structure has been formed. All of the three antennas are manufactured through this method. Figure 2.5 shows the antenna of Design I and its polyamide template. Compared to some other newly developed 3-D small antenna fabrication methods [73], [74], the SLS based template method has a low cost for mass production.

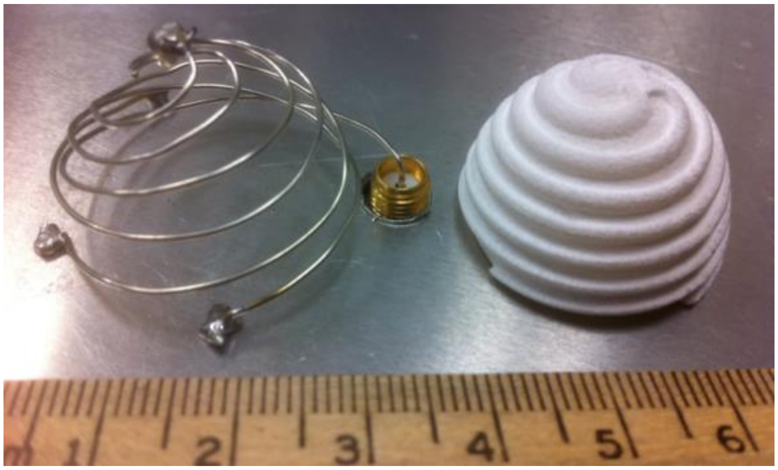

Figure 2.5: Picture of Antenna Design I (left) and its template (right) fabricated using selective laser sintering.

The three antennas were fabricated through the SLS based process described above, and measured using SMA connector on a ground plane. The calibration of the network analyzer is at the SMA port of the coaxial cable though the standard open-short-load one port calibration, in order to minimize the impact from the cable on the measurement. The resulting return loss (S_{11}) is shown in Figure 2.6. The measurement data shows a good agreement with the simulated data for all cases. The resonant frequency of Design I is shifted by 0.04 GHz, lower than the designed resonant frequency of 2.40 GHz. Design II and design III also have resonance down shift from the simulation of less than 1%. This is possibly induced by the fabrication error of the SLS machine (the SLS machine has a standard error of less than 0.2 mm during the manufacturing), and/or error introduced when transferring the antenna from the template. We are still improving the transferring step to minimize the fabrication error. The measured and simulated radiation patterns for designs I is shown in Figure 2.7. With an electric size much smaller than the wavelength, the pattern mainly follows a monopole like electrically small antenna radiation pattern. Design II also has a typical ESA radiation pattern while for Design III, the radiation pattern is quasi-dipolar according to the simulation results. The novel design holds great promise as a means to clinically assess a broad range of implant devices. Overall, the realized antennas of the three prototypes work at the desired 2.4 GHz ISM band in good agreement with the design and simulation, and with a moderate bandwidth of operation.

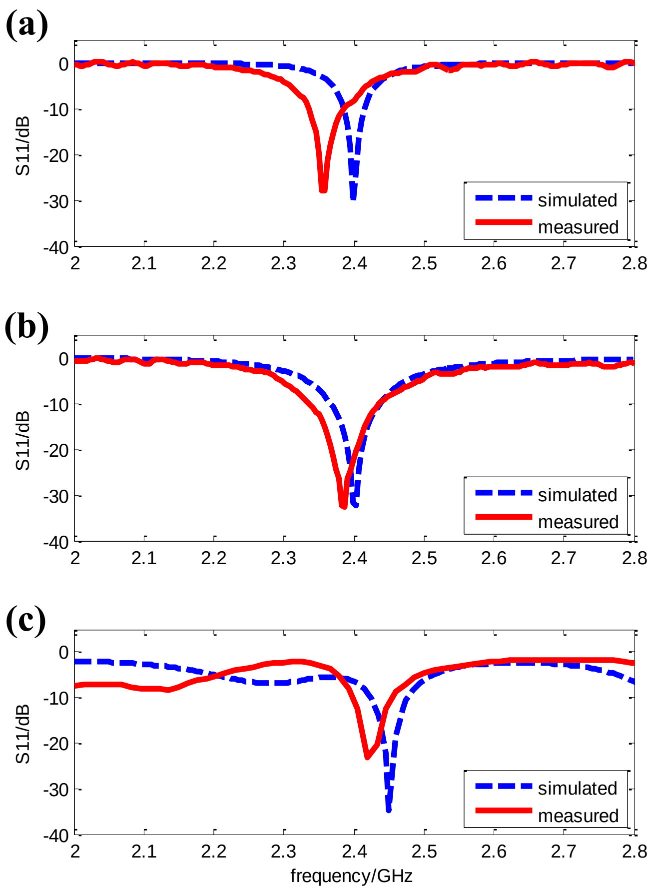

Figure 2.6: Simulated (using NEC) and measured return loss for (a) Design I, (b) Design II, and (c) design III.

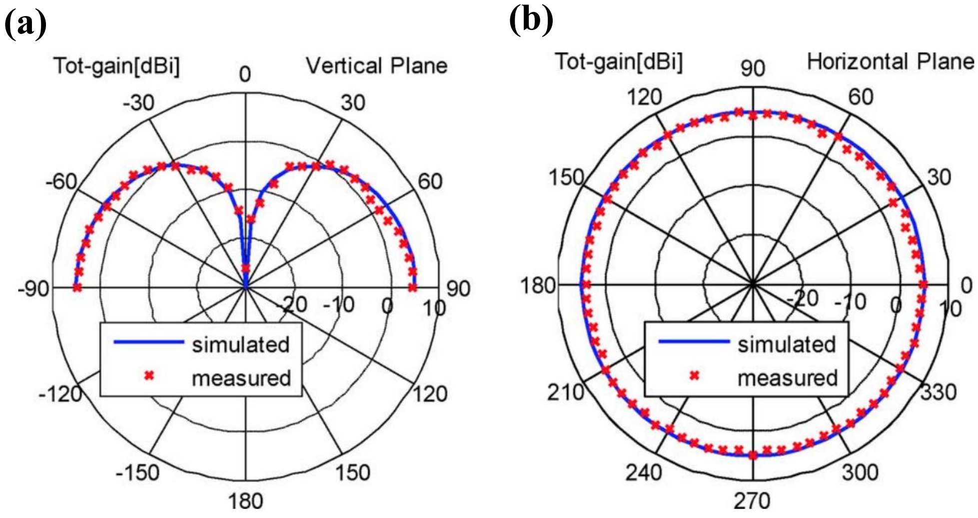

Figure 2.7: Simulated (using NEC) and measured radiation pattern for Design I: (a) E-plane; (b) H-plane.

2.5 DUAL BAND ANTENNA DESIGN

The electrically small folded ellipsoidal helix antenna can be further adjusted to fit specific healthcare application needs such as multiband operation. In cellular communication antenna design, to design a dual band cylindrical helix antenna to any dual frequencies need, variable pitch has been adapted because the total length of the antenna will largely determine the low band while adjusting the details in pitch angles will shift the resonant frequency at the high band [75], [76]. Here in order to design a dual band antenna for pacemaker wireless powering and data communication, we apply a similar concept of variable pitch to the spherical and ellipsoidal helix antenna.

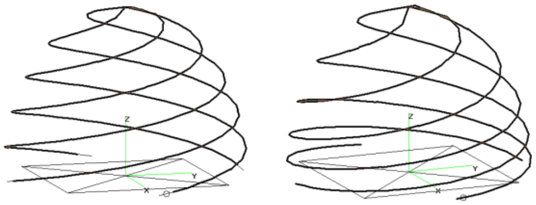

Figure 2.8: A 4-arm folded ellipsoidal helix antenna with α = 0 (left) and α = 0.6 (right).

The modeling of the dual band antenna starts with a general ellipsoid body in Cartesian coordinate, similar as the model shown in the section 2.3. The difference is that the coordinates of the nth wire section in the *m*th arm $(x_{m,n}, y_{m,n}, z_{m,n})$ is expressed as

$$x_{m,n} = a \sin\delta_n \sin\phi_{m,n} \tag{9}$$

$$y_{m,n} = YAR \cdot a \sin\delta_n \cos\phi_{m,n} \tag{10}$$

$$z_{m,n} = ZAR \cdot \left(\alpha \frac{n^2}{N^2} + (1-\alpha)\frac{n}{N}\right) \cdot a \tag{11}$$

where

$$\delta_n = \cos^{-1}\left(\alpha \frac{n^2}{N^2} + (1-\alpha)\frac{n}{N}\right) \tag{12}$$

$$\phi_{m,n} = 2\pi p \frac{n}{N} + 2\pi \frac{m}{M} \tag{13}$$

Here α can be any real number from zero 0 to 1, it varies the distribution of the wire segments along the *z* axis, representing the uniformity of the pitch angle of the ellipsoidal helix. Figure 2.8 shows the comparison of ellipsoidal helix antennas with uniform and non-uniform pitch.

The basic design procedure of an ellipsoidal helix antenna has been described in subsection 2.3 , which can be applied to determine the low band by initially setting up the parameters of p and ZAR with a fixed radius a, corresponding to the size of a pacemaker. The effect of the pitch angle uniformity α is mostly on the high band. In fact, we found that a constant wire length design will keep the low band resonant frequency unmoved. As shown in Figure 2.9, as α varies from 0 to 0.6, the value of k is adjusted correspondingly to keep the total wire length at 45.5cm. As a result, the resonant frequency of the low band almost stay at 930MHz while the high band resonance shifted from 2300MHz to 2400MHz. This implies the importance of the variable α in designing an antenna to any desired dual band.

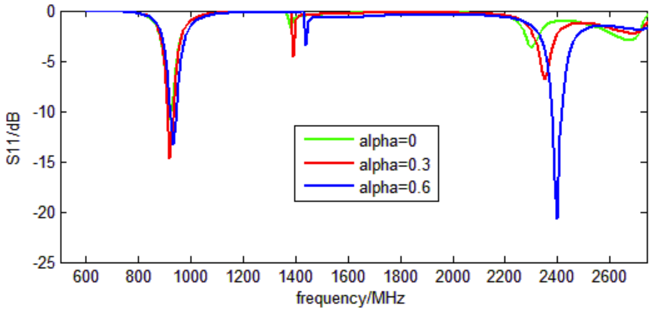

Figure 2.9: NEC simulation of the effect of pitch angle uniformity variable α on the antenna resonance.

The value of α does impact the feedpoint impedance of the antenna at the high band according to Figure 2.9. Although the matching condition can be further compensated by fine tuning the value of *ZAR* and *p*, at the same time the impedance at the low band will be affected. The self-impedance matching design principle described in [67] is valid for electrically small antenna, while the antenna here has a dimension more than 2 cm so at 2 GHz it is already out of the electrically small region. The matching condition and resonant frequency at the high band is quite sensitive to parameter changes and this work won't be focused on perfect self-impedance matching at both frequencies. Some minor empirical tuning can lead to a reasonable design for the 930 MHz and 2.4 GHz dual band with an impedance of 54.9- j22Ω at the low band and 53.8- j8.78 Ω at the high band. The corresponding design parameters are m=4, p=1.09, a=1.76cm, *ZAR*=1.65 and α=0.6. The total wire length including all 4 arms is 45.5cm.

Figure 2.10 (a) and (b) show the current distributions of ellipsoidal helix antennas with different geometrical factors α at the operating frequencies 900 MHz and 2400 MHz, respectively. We notice in Figure 2 the first resonant frequency (900 MHz) is quite robust to the geometrical variations, provided that the total length of helix is fixed. This is also reflected in Figure 2.10 (a), in which similar current distributions are obtained from our numerical results. Since the current is radiating, the absolute value of current decays smoothly along the helix wire. On the other hand, we find that the second resonant frequency (2400 MHz) is tunable by varying the values of α. From Figure 2.10 (b), we observe a standing-wave region and rapid local variation of surface current at 2400 MHz. The deviation between different cases gives rise to the much increased electrical size and enlarged current path at the higher frequency, for which the current density modes are rather sensitive to the shape variation controlled by the value of α.

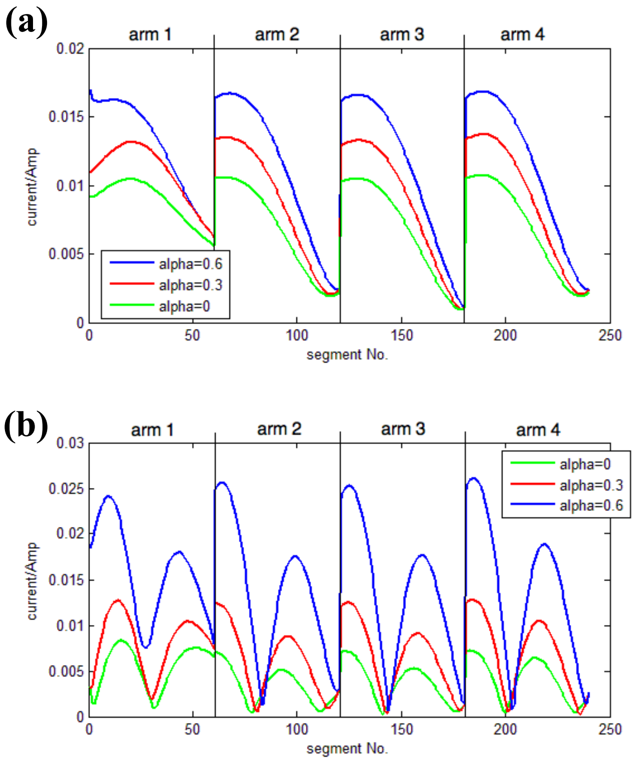

Figure 2.10: Simulation of current distribution (using NEC) along the helix wire for all the four arms at (a) 930MHz (b) 2400MHz. There are 60 wire segments on each helix arm, with a feeding point at segment No.1, arm 1.

At 930 MHz, the antenna possesses a very small electrical size, following a monopole radiation pattern as shown in Figure 2.11 (a), for which the resonant frequency is determined only by the length of helix wire and the total inductance resulting from the densely packed helix. For the high band at 2.4 GHz, the pattern on the vertical plane shows a highly distorted monopole pattern as shown in Figure 2.11 (b). At the high band, it is out of the electrically small region for which $2\pi a/\lambda<0.5$.

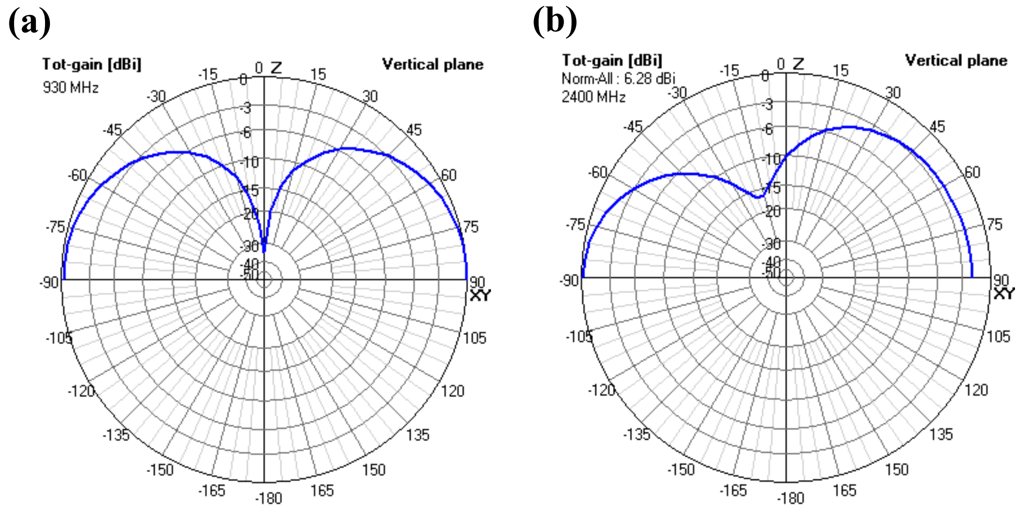

Figure 2.11: Simulated vertical plane far field radiation pattern (using NEC) at: (a) 930 MHz :, (b) 2400MHz.

The dual band antenna was fabricated using the selective laser sintering process as described in subsection 2.4. For multi-arm designs, soldering at the junction is necessary for a reliable electrical connection. Figure 2.12 shows that the fabricated antenna has a comparable size as a Medtronic cardiac pacemaker.

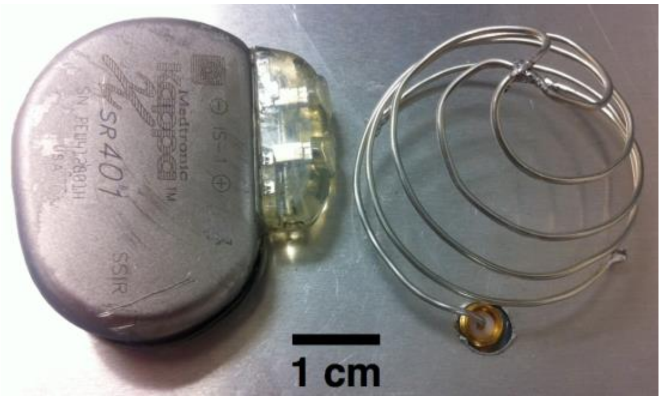

Figure 2.12: The fabricated antenna with a matched size of an artificial cardiac pacemaker.

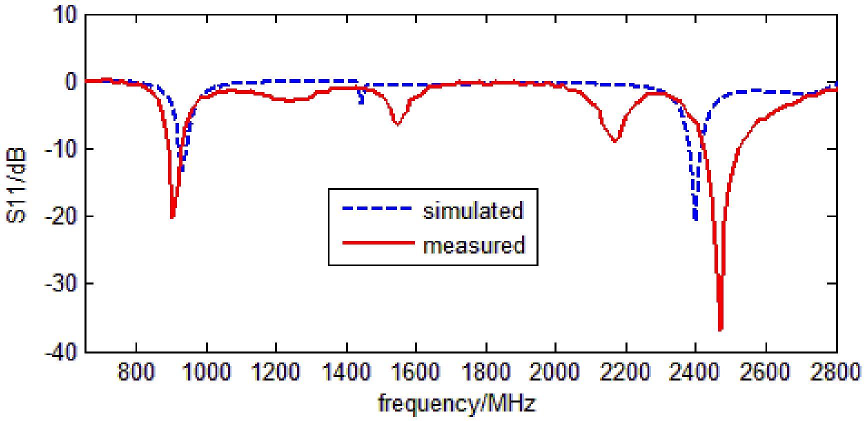

Figure 2.13: Simulated (using NEC) and measured S_{11} of the dual band antenna design.

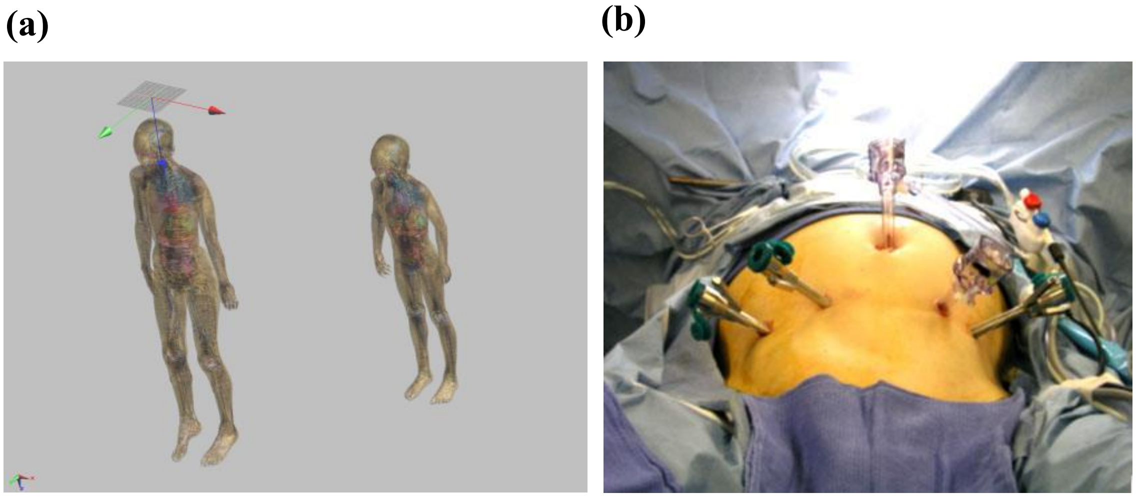

Figure 2.14: Potential application of ellipsoidal helix ESA in deep medical implants: (a) Human body models with different age and size in the SEMCAD X simulation environment. (b) Minimally invasive surgery procedure which can incorporate with the tuning of *ZAR* of an implanted ellipsoidal helix ESA to compensate anatomical diversity.

The measurement S_{11} shown in Figure 2.13 has good agreement with the simulation at the low band. However, at the high band the antenna properties are sensitive to fabrication defects and errors. To some extent, a constant wire length will keep the low band unaffected, which makes on site manual fine-tuning during the experiment possible in order to get a desired high band. The realized resonant frequency is 910MHz at the low band and 2.46GHz at the high band, with 100MHz and 200MHz bandwidth, respectively, which is well suitable for operation on the 910~930 MHz ISM band and 2.4~2.5GHz ISM band.

2.6 SURGICALLY TUNABLE ESAS FOR MEDICAL IMPLANTS

All the simulation results sofar are based on environmental permittivity $\varepsilon_r = 1$, corresponding to free space. If the surrounding environmental permittivity is set to a different value, for example, $\varepsilon_r = 78$ (corresponding to water), the resonant frequency of the antenna will scale by a factor of $1/\sqrt{\varepsilon_r}$ [77], and it is verified by NEC simulation. However, this is based on the assumption that the surrounding material occupies an infinitely large volume and has a uniform material property. For most implant applications, the surrounding human body fluid environment can barely cover the near field region or Fresnel region of the implanted antenna. Therefore simply changing the environmental permittivity setting will not predict the performance correctly.

For implanted antenna design, most literatures have been seeking approaches to predict antenna performance with some human body model in the electromagnetic analysis and simulation [54], [60], [61]. In reality, however, anatomical diversity of human body (illustrated in Figure 2.14(a)) will make such antenna design impractical. In other words, a universal design may not be possible for all users. One approach is to have different models representing different body anatomy types. A group of high resolution human body models from IT IS Virtual Population Database have been realized after five years development [78], which can only be used in SEMCAD X simulation software [79]. Alternatively, as medical implant will involve a surgery procedure any, if utilizing a tunable antenna such as the ellipsoidal helix ESA presented in this chapter, an empirical tuning of *ZAR* parameter on site as part of the surgery protocol would be more efficient approach to compensate the anatomical diversity (illustrated in Figure 2.14(b)).

2.7 CHAPTER SUMMARY

In this chapter an electrically small folded ellipsoidal helix antenna is proposed for size-restricted wireless medical telemetry applications. From extensive simulations, we find that the additional Z aspect ratio of a folded EHA provides the ability to tune the antenna resistance, without affecting the reactance, implying that the folded EHA could reduce or eliminate the need for external matching components. Additionally, three practical EHAs with different sizes and geometrical requirements are designed to operate at the 2.4GHz ISM band and are fabricated using an SLS-based templating method. Measurement results are in good agreement with simulations, demonstrating a bandwidth more than 100MHz and an omnidirectional monopolar radiation pattern for all three designs. Another design of variable pitch-angle, multi-arm folded ellipsoidal helix antenna is also proposed for dual band medical implant applications, especially for wireless cardiac pacemakers. By fixing the total wire length, the antenna can lock its first band, while adjusting the high band resonance by varying the pitch angle uniformity of the helix. A 917 MHz and 2.46GHz dual band antenna is fabricated and further optimized through experimental tuning, realizing a bandwidth of about 10% at each band. One additional benefit that the folded ellipsoidal helix ESA may bring to wireless medical implants is its compatibility to be tuned on site of implantation surgery, in order to compensate anatomical diversity of human body as well as any other uncertainties unpredictable during the initial design.

Chapter 3: Miniaturized Wireless Drug Monitoring RFID Transponder Antenna Sensors[2]

3.1 INTRODUCTION TO DRUG DELIVERY MONITORING ANTENNA SENSORS

Driven by the rise of micro and nano technologies, controlled rate and micro-patterned drug deliveries have been playing major roles to overcome the limitations of conventional burst-release dosage forms [80]. Instead of injecting drugs at the maximum tolerable dose (MTD) once in a treatment period, contemporary drug delivery paradigms maintain the constant release and administer it within some desired therapeutic range, providing minimized side effects and increased therapeutic efficacy [81], [82]. The existing drug delivery systems have different control mechanisms [81]–[86]. No matter what control mechanism is adopted, drug dosage monitoring is crucial to provide feedback as well as to prevent unexpected in-vivo fluctuation and leakage. In addition, dosage monitoring will also benefit personalized medical tracking and chronic disease management.

During the past decade, various drug delivery monitoring technologies have been developed such as photoacoustic tomography [87], electron paramagnetic resonance [88],

---

[2] A large portion of the materials in this chapter were based on the following publications, to which all the co-authors have contributions:
H. Huang, P. Zhao, D. Fine, Y. Ren, M. Ferrari, Y. Hu, D. Akinwande, "Bio-compatible Miniaturized Helix Antenna Sensors For Wireless Drug Delivery Monitoring", *First IEEE Healthcare Technology Conference: Translational Engineering in Health & Medicine*, Houston, TX, Nov. 2012
H. Huang, P. Zhao, P. Y. Chen, Y. Ren, X. Liu, M. Ferrari, Y. Hu, D. Akinwande, "RFID Tag Helix Antenna Sensors for Wireless Drug Dosage Monitoring", *IEEE Journal of Translational Engineering in Health and Medicine*, Vol.2, 2014

and fluorescence based imaging [89]. Even though the size and cost of drug delivery system are continuously going down, most of the existing monitoring methods still involve bulky equipments and expensive test process, not suitable for ubiquitous healthcare IoT. Here we propose a cost effective wireless drug dosage monitoring sensor utilizing 3-D miniaturized antenna as its sensing agent. The concept of the wireless drug dosage monitoring system is shown in Figure 3.1. With properly designed and customized antenna sensors, the drug volume inside any transdermal drug delivery device from IontoPatch$^{\text{TM}}$ [90] to Empi Action Patch$^{\text{TM}}$[91], or any implanted drug delivery device from SmartPill$^{\text{TM}}$[92], Philips iPill $^{\text{TM}}$[93] to MicroCHIPS$^{\text{TM}}$ [94], can be wirelessly tracked in real-time. The external control and monitoring unit can be any small portable device, including tablet and smart phone. This would be a major attractive feature because it potentially makes up some part of the nodes in wireless healthcare network [95], while the challenge in realizing such system is how to design a miniaturized drug dosage sensor with minimized extra cost and also make it fully integratable with the drug delivery device.

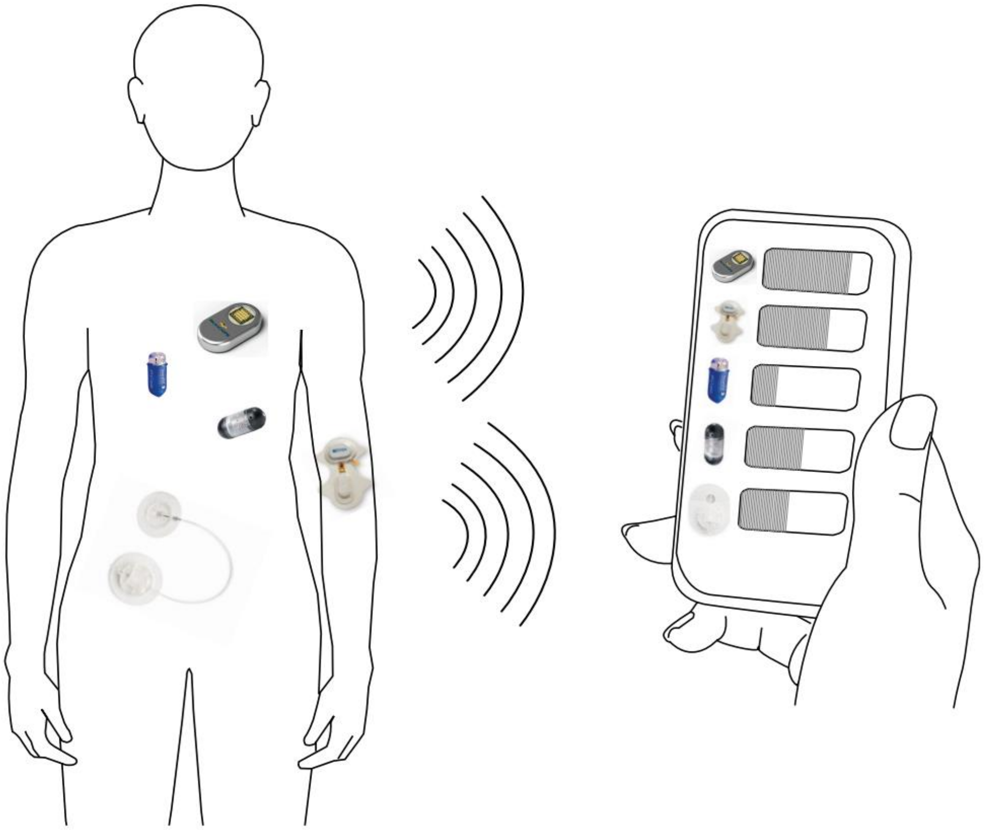

Figure 3.1: Illustration of the proposed real time drug delivery monitoring system. Utilizing the antenna drug dosage sensors, a portable device can remotely track the drug volume in drug delivery devices.

3.2 THE ANTENNA SENSOR DESIGN

3.2.1 Perturbation Theory

A helix antenna wrapped around a core of dielectric material is called dielectric-loaded helix antenna [77]. Different core materials with different effective permittivity will affect the radiation properties of the antenna. For liquids like water, body fluids and liquid drugs, the relative permittivity is high, usually at 60--80 range at RF and microwave frequencies [96]; by contrast, solid-state organic powders have much lower relative permittivity at the range of 1--5. With the same helix antenna, when the core are loaded with liquids, the resonant frequency of the antenna is lower than when air or powders are filled in. For transdermal drug deliveries [85], since the drugs are in liquid state (large permittivity ε), the antenna resonant frequency will shift up as the drug releases. For implanted drug deliveries [81], [82], the initial state is full of powders (small ε). As the drug releases, body fluids (large ε) will fill in, and the resonant frequency will shift down. The comparison of transdermal and implanted drug deliveries is depicted in Figure 3.2.

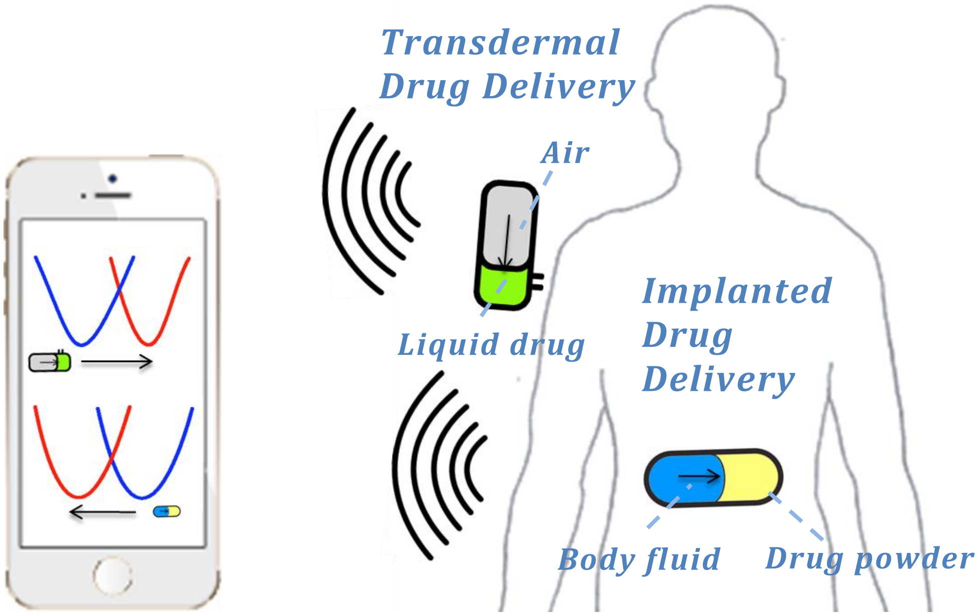

Figure 3.2: Comparison of antenna based drug delivery monitoring in transdermal and implanted drug delivery applications.

During drug delivery process, whether it is liquid-air exchange or powder-liquid exchange, there is large contrast of permittivity between the exchanging materials. The dielectric-loaded antenna itself can be considered as a cavity resonator. When the interface between the high ε material (liquid) and the low ε material (air or powder) shifts, its resonant frequency change can be initially analyzed by the perturbation theory for resonators [77], [97].

Suppose a small shape perturbation ΔV is applied to a dielectric resonator V_0 resonating at f_0 , the resulting resonant frequency f will satisfy [88]:

$$\frac{f-f_0}{f_0}=\frac{\int_{\Delta V}(\mu\|\overrightarrow{H_0}\|^2-\epsilon\|\overrightarrow{E_0}\|^2)\,dv}{\int_{V_0}(\mu\|\overrightarrow{H_0}\|^2+\epsilon\|\overrightarrow{E_0}\|^2)\,dv} \tag{14}$$

where ε and μ are the permittivity and permeability of the liquid material. In addition, the electromagnetic field inside a helix coil is intense and almost constant along the cylinder direction z , namely

$$\|\overrightarrow{H_0}\|=H(x,y),\|\overrightarrow{E_0}\|=E(x,y) \tag{15}$$

Then when liquid level shifted from h_0 to h

$$\frac{f-f_0}{f_0}=\frac{\int_{\Delta h}[\int_S(\mu H^2(x,y)-\epsilon E^2(x,y))\,dx\,dy]\,dz}{\int_{h_0}[\int_S(\mu H^2(x,y)+\epsilon E^2(x,y))\,dx\,dy]\,dz}$$

$$=\frac{\int_{\Delta h}A\,dz}{\int_{h_0}B\,dz}=C\frac{h-h_0}{h_0}$$

(16)

Equation (16) is valid for electrically small helix antennas, of which the inner field distribution is almost uniform. From (16), we know that the resonant frequency shift will be linearly dependent on the liquid surface level shift. In practice, however, the core inside dielectric-loaded helix is not a perfect cavity resonator, and the electric field along the cylinder is also varied. The perturbation theory can only conceptually predict the variation of resonant frequency with respect to the filling ratio of dielectric core. Accurate and reliable antenna sensor design needs to be evaluated by full-wave electromagnetic simulations.

3.2.2 FEM Simulation and Design Environment Validation

The radiation properties of the helix antenna sensor are simulated using Ansoft High Frequency Simulation Structure (HFSS). HFSS is an electromagnetic simulation software based on the finite element method (FEM) [98]. The simulation interface in HFSS is shown in Figure 3.3(a). The purpose of this simulation is to understand the impacts of helix parameters on the performance of the antenna as a drug dosage sensor. In general cases, the diameter of the helix antenna is determined by the reservoir's dimension and therefore is fixed. So the number of turns, the helix pitch angle, and the relative position of the helix along the device are the tuning variables for the sensor design. The design goal is to maximize the sensitivity and linearity across the test range; however, it is important to comply with Federal Communications Commission (FCC) regulations and only use the frequency bands that are allocated for medical applications. In this demonstration, we target the 2.4--2.5GHz ISM band (the industrial, scientific and medical radio band). Therefore the design challenge is to ensure the antenna resonant frequency shifts between 2.4 and 2.5GHz when the drug dosage varies within the range of interest, which is usually from 0% -100% of the volume of the drug reservoir. Drug reservoirs with different sizes and geometries need customized antenna sensors for optimized drug dosage monitoring performance, so there is no universal design.

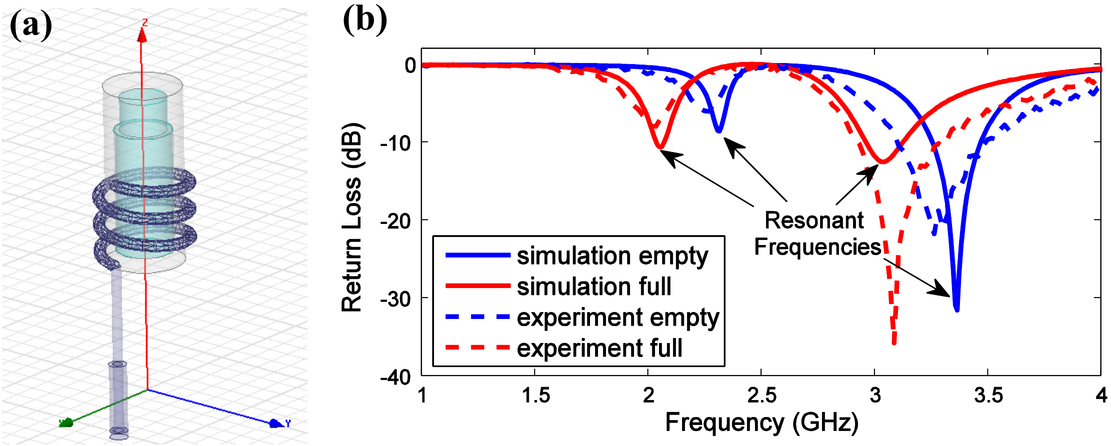

Figure 3.3: A simulation-experiment comparison to validate the initial setup: (a) The antenna sensor in the HFSS simulation interface; (b) The simulated and measured return loss of the antenna sensor at full state (loaded with liquid drugs) against empty state.

The first step of antenna sensor design is to set up the right design environment in HFSS, including the right material parameters and boundary conditions. This can be validated by some simple initial tests. The details of the measurement procedure will be included in Section 3.3 , while here in the initial test the helix antenna is simply wrapped around a cylinder reservoir without any packaging materials. The antenna has 3.5 helix turns with 1.5mm pitch gap between the adjacent turns. A comparison between the simulation of the antenna return loss S_{11} and the tested S_{11} is shown in Figure 3.3(b). Two resonances can be observed, one is around 2.35 GHz, the other is around 3.4 GHz when the reservoir is empty. After the cylinder is filled in with liquid, the two resonant frequencies shift to 2.0 GHz and 3.0 GHz, respectively. It can be seen that the simulation result matches the measurement result well at both resonant frequencies, showing similar patterns of S_{11} profile and resonance shift after the material changes inside the reservoir, which validates the accuracy of the simulation environmental parameter settings. Although there is a small difference in the dB value of S_{11} between simulation and measurement data at some resonances, in practice this value could be controlled properly with tuned matching.

3.2.3 Tuning of Helix Parameter

A cylindrical helix antenna is defined by its radius, number of turns and pitch gap between adjacent turns. Normally the radius needs to be consistent with the size of the reservoir of the device the antenna sensor integrated with, so the impact of three other helix parameters on antenna sensor performance is investigated through HFSS simulation. The results are in terms of sensitivity curves showing the resonant frequencies under 0%--100% normalized drug dosage levels which is included in Figure

3.4. Figure 3.4(a) shows the sensitivity curves of an antenna sensor with 2.5mm pitch gap and varying number of turns. As the number of turns increases, the whole curve moves downward to lower frequencies. Whereas in Figure 3.4(b), the whole curve moves upward to higher frequencies as the pitch gap increases. Such result can be explained by modeling the helix as a solenoid coil. Hence the performance of the antenna sensor can be properly adjusted by changing its number of turns and pitch gap.

(a)

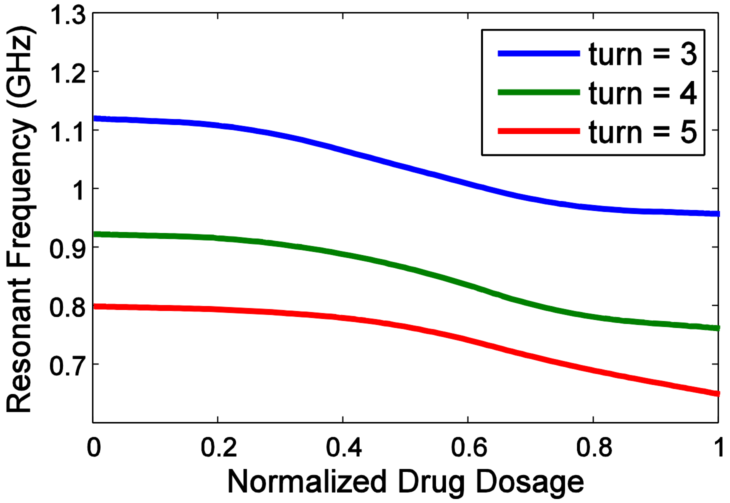

(Figure 3.4 continued next page)

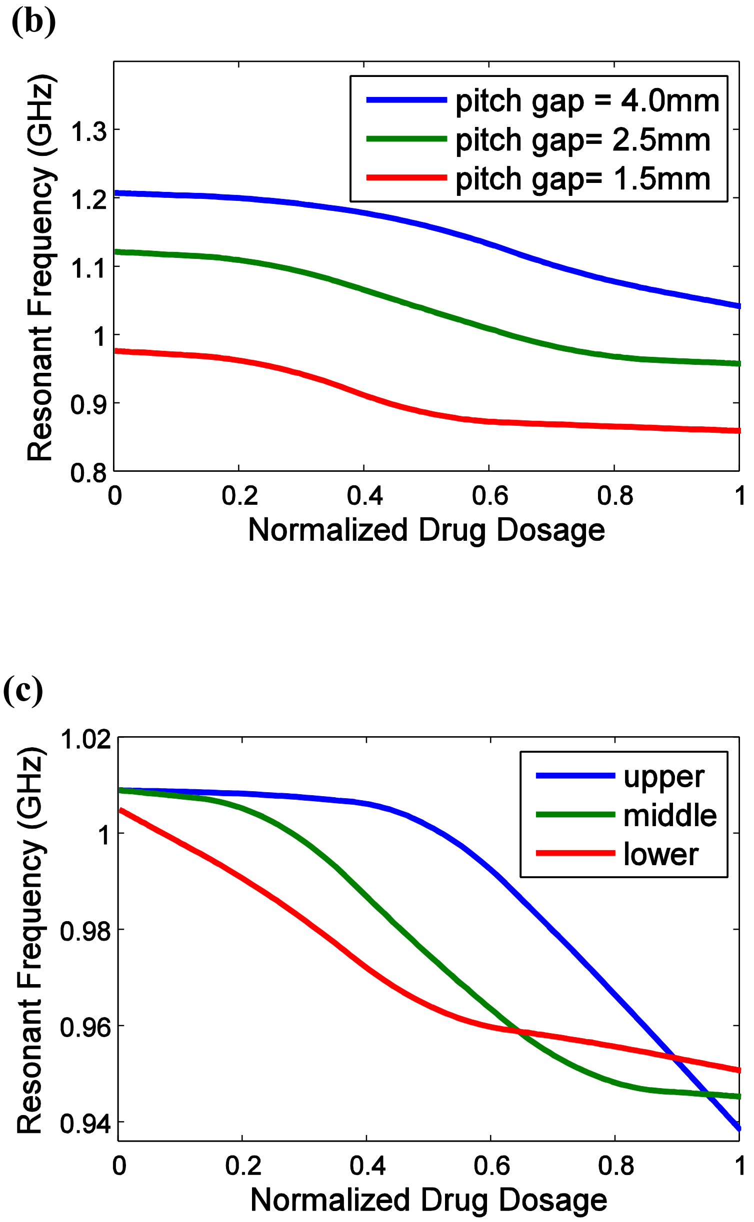

(Figure 3.4 continued next page)

(d)

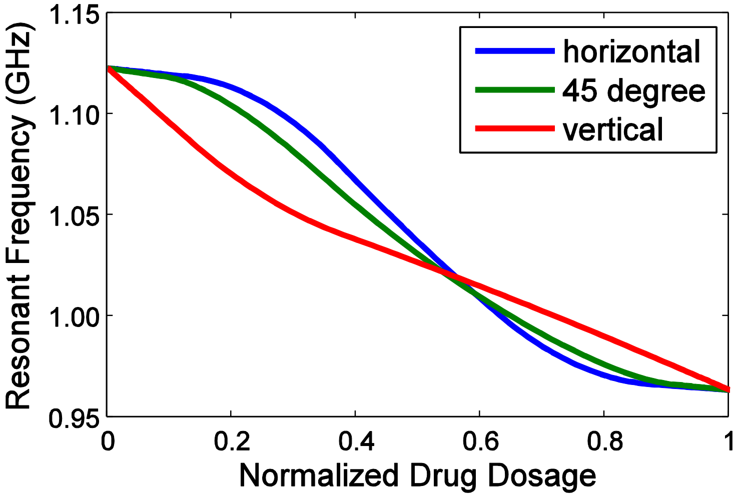

Figure 3.4: Simulation of the sensitivity curves of the helix antenna sensor with different design parameters: (a) Tuning number of turns. (b) Tuning pitch gap. (c) Tuning the helix position along the reservoir. (d) The influence of antenna sensor orientation.

It is interesting to point out that when the number of turns or the pitch gap is large enough to make the whole helix antenna to cover the whole cylinder body, the sensor is mostly linear, as predicted from the theory in Section 3.1. When helix antenna is not long enough to cover the cylinder completely, the relative position of the antenna is important to optimize the sensor performance. Figure 3.4(c) shows the simulation result of an antenna that only covers half of the cylinder, and is placed at three different spots alongside the cylinder. It can be seen that the antenna sensor is less sensitive when the liquid-air interface is out of the helix coil covered region.

Another important fact is, under different situations, the drug container may be placed at different angles, and the impact of the helix orientation must be identified. The sensitivity curves of a long helix antenna covering the whole cylinder placed at different orientations is shown in Figure 3.4(d). In this simulation, the liquid-air interface is set to be horizontal, vertical and 45 degree against the ground. The differences among the curves indicate that the antennas are vulnerable to rotation, with an error up to 25%. So it is important to take the placement angle of antenna into consideration when designing the antenna sensor.

3.3 SENSOR-PACKAGE ASSEMBLY FABRICATION

The miniaturized 3-dimensional antennas can be fabricated using different techniques, for example, laser printing [73] and molding process [99], [100] as described in Chapter 2. In this chapter, we use molding process for the antenna sensor demonstration. First, a mold with the designed geometrical parameters is fabricated using the selective laser sintering (SLS) machine, then copper wire antennas can be duplicated out from the mold. Due to the special structure of helix antenna, sometimes screws with proper parameters can be directly used as the mold to make the miniaturized helix antenna. Therefore, the cost of the antenna manufacturing can be negligibly low for mass production.

The antenna on package concept has also been described in Chapter 2. The larger volume an electrically small antenna occupies, the higher bandwidth the wireless channel will have. For any implanted electronic device, it is beneficial to have a three-dimensional antenna placed around the implant package in order to provide higher bandwidth for the antenna, in contrast of having a two dimensional planar antenna placed inside the package. Especially for implanted drug delivery devices, an antenna-package assembly design can also save a significant portion of the device volume for the drug reservoir, thus extending the effective time span of the drug delivery implant.

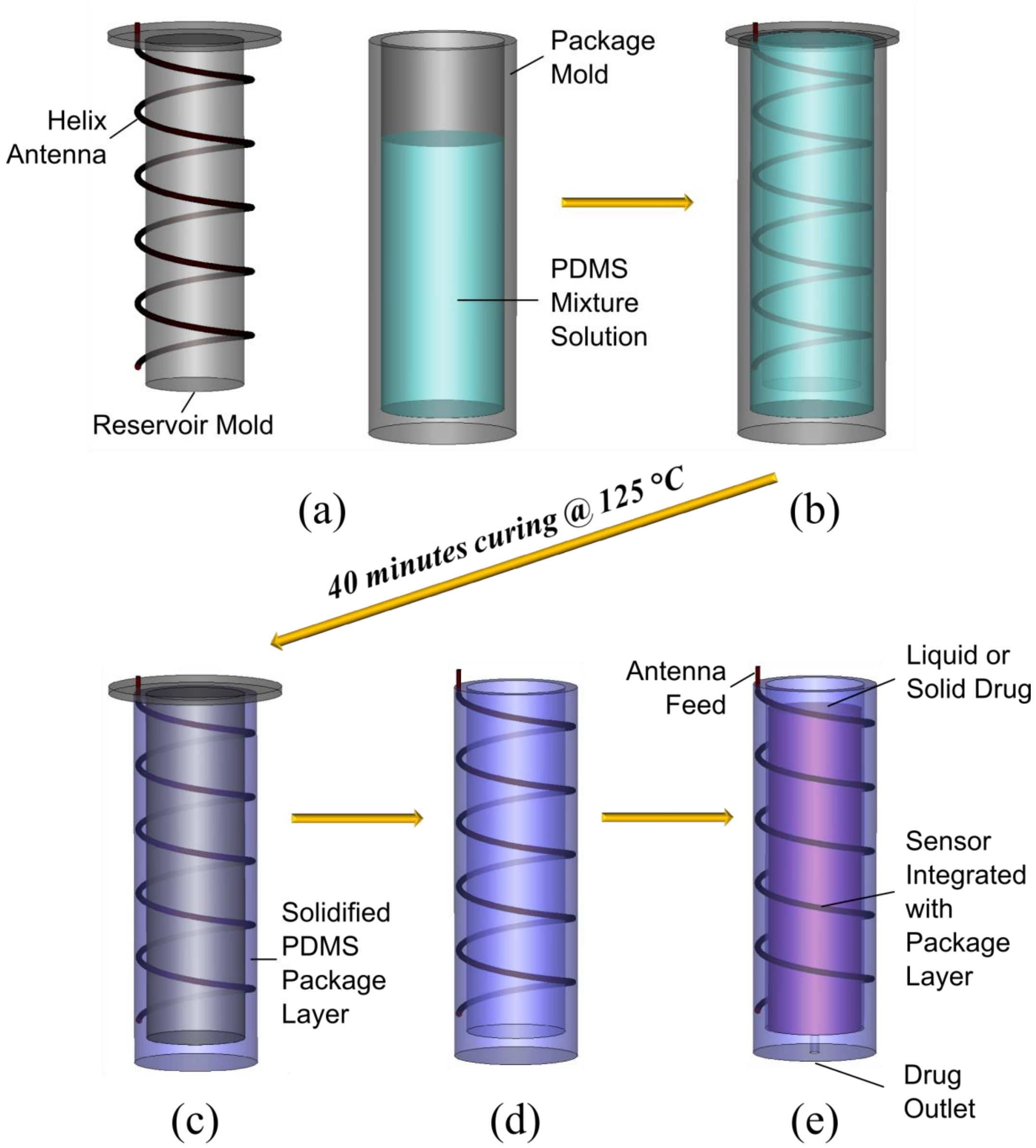

Figure 3.5: The fabrication process of the antenna-package assembly.

Figure 3.6: The manufactured antenna sensors with PDMS packaging.

In this demonstration, we utilize a package-antenna assembly configuration in which the antenna is embedded inside the package layer. For implanted drug delivery usually a biocompatible packaging material is required in order to prevent metal leaching into the body. In the antenna sensor demonstration, copper wire antenna and Polydimethylsiloxane (PDMS) package are used for the antenna-package assembly. PDMS is a Si based organic polymer widely used in micro fabrication and device encapsulation. Its bio-compatibility, high chemical inertness, as long as its mechanical property--flexible, but sturdy enough to tolerate bending across macroscopic scales, make it a very suitable and safe material [101]. Even for the transdermal drug delivery where the device is attached to the skin and there is less space restriction and less bio-safety consideration, the antenna- PDMS packaging assembly is still an advantageous solution.

The fabrication process of the antenna-package assembly is shown in Figure 3.3. First the helix antenna feed tip is fixed at the top of a reservoir mold in order to stabilize the antenna, allowing the helix wire winding around the cylinder part of the reservoir mold without touching the mold. As shown from Figure 3.5(a) to Figure 3.5(b), the reservoir mold along with the wire antenna is then placed into a package mold filled in with PDMS mixture liquids (ten parts PDMS base and one part curing agent). The whole set is then kept in a desiccator for one hour to eliminate all the trapped air bubbles, followed by 40 minutes curing in a 125 °C oven. After the PDMS is solidified and cross linked, the package mold can be released as shown in Figure 3.5(c). The device was cooled down at -5 °C in the refrigerator, in order to take off the reservoir mold. When both molds have been taken off as shown in Figure 3.5(d), the final step for the demonstrative device is to drill some holes at the bottom as outlets for the drugs, as shown in Figure 3.5(e). A picture of two fabricated antenna sensors with different reservoir capacities and antenna parameters are shown in Figure 3.6. The antenna sensor at the left has 11 turns and 1.5 mm pitch, with a 0.117 ml reservoir inside. The helix antenna sensor at the center has 8 turns and 2 mm pitch, with a 0.221 mL reservoir inside.

The PDMS package layer also has impact on the performance of the antenna sensor. Generally, thinner package layer is preferred in order to reduce the intrinsic loss of PDMS, though a very thin layer raises the risk of package breakage and exposing the antenna metal wire to the body. An optimized thickness takes both wireless transmission power efficiency and the bio-safety into account, and it is important to study the role of package layer thickness in the whole sensor design. Therefore, HFSS simulation of an antenna sensor with the PDMS package layer is shown in Figure 3.7. In Figure 3.7(a), varying inner radius leads to different sensitivity curves when the outer radius is set to be 4.8mm. We can see that the inner radius makes a noticeable difference when liquid drug dosage is high; while from Figure 3.7(b), it can be seen that the influence of package outer radius on the sensor is minimal. And Figure 3.7(c) shows the impact of the relative permittivity value of PDMS material on sensitivity curves, which only moves the curve without affecting the local sensitivities. After the package impacts have also been taken into consideration as part of the sensor design parameter optimization, in our final devices, the copper wire is fixed at 1mm in diameter and the package layer is chosen to be within 1.8 mm to 2.0 mm thickness range.

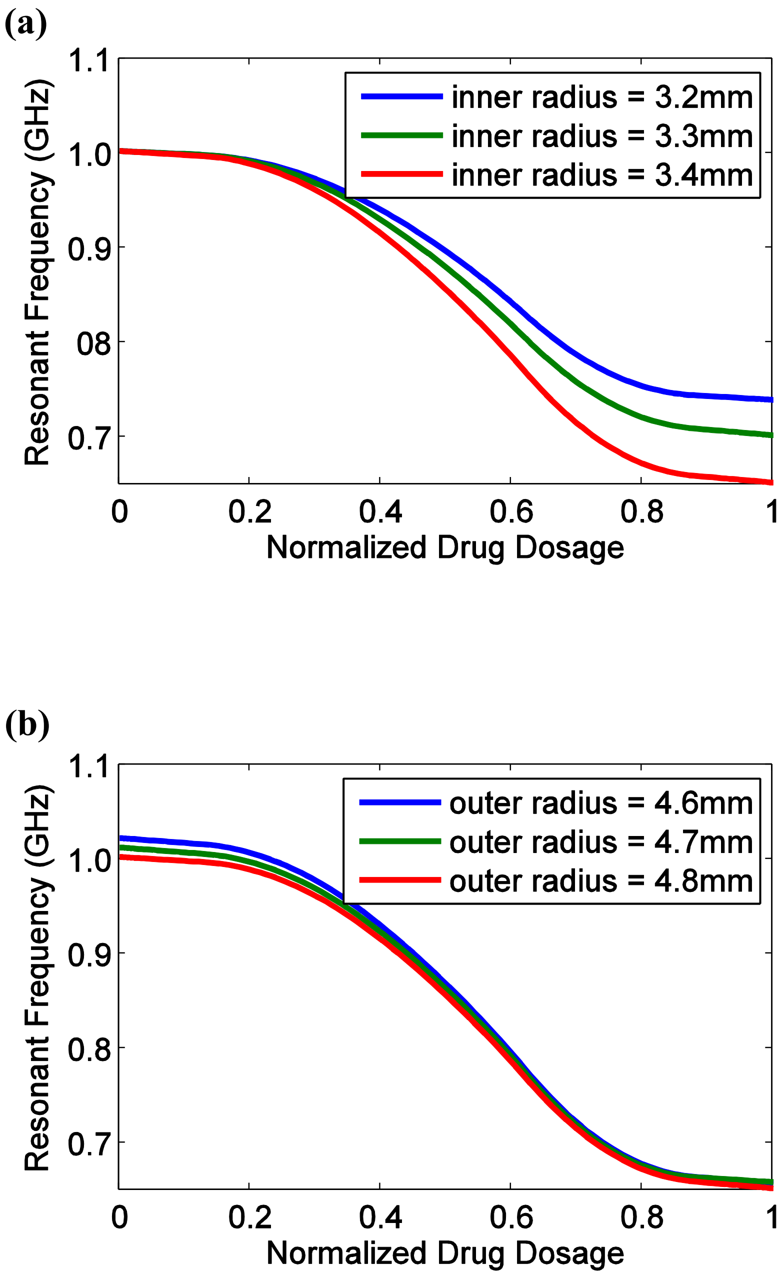

(Figure 3.7 continued next page)

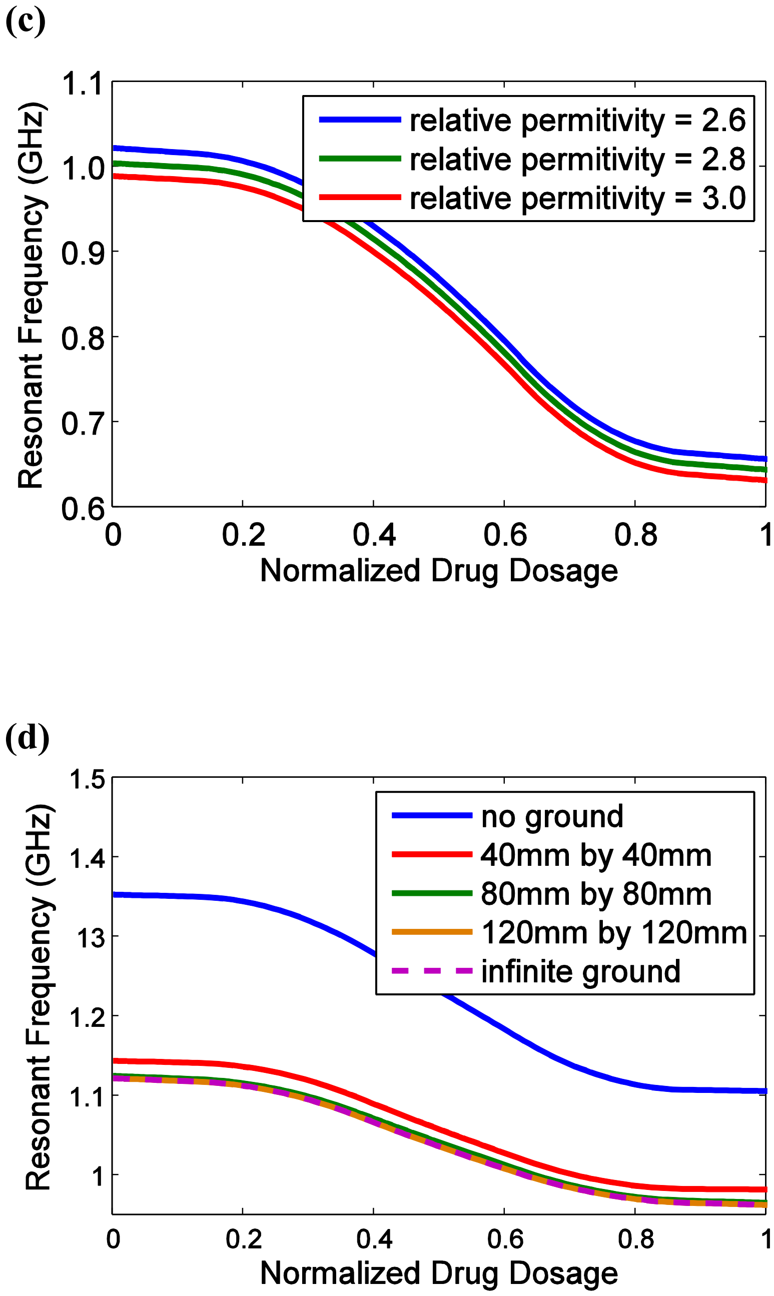

(Figure 3.7 continued next page)

Figure 3.7: Simulation of the sensitivity curves of the helix antenna sensor-PDMS package assembly under variant conditions: (a) The influence of inner radius of the PDMS cylinder. (b) The influence of outer radius of the PDMS cylinder. (c) The influence of relative permittivity of the PDMS material. (d) The influence of metal ground plane size.

For the helix antenna, an infinite ground plane is usually assumed to be presented to make it a perfect monopole type antenna. In practice for drug delivery devices there is limited space to place the ground plane. In order to examine the impact of finite ground plane, a simulation study is shown in Figure 3.7(d). We can see that without ground plane the whole sensitivity curve will move upward to higher frequencies. It can be also observed that when the ground plane is larger than 80 mm by 80 mm, the sensitivity curve will be almost identical as the one with infinite ground plane. For real products, a small circular metal plane can be added at the bottom of the cylinder reservoir to adjust the antenna sensor performance. However, to simplify the design and fabrication, our demonstrative devices do not contain any ground plane, similar to the end-fed half wave dipole antenna.

3.4 THE IN-VITRO TEST

The in-vitro experiment to test the antenna sensor performance is carried out using an Agilent E8361C 10MHz--67 GHz PNA network analyzer connected with a DC--40 GHz co-axial RF cable. A female-to-female SMA adapter is connected with antenna and RF cable at each side for feeding the helix from the end tip. The experimental setups are different for transdermal drug delivery and implanted drug delivery demonstrations. For transdermal drug delivery it is air surrounding environment. In the demonstration, the reservoir was initially empty and gradually filled in with liquid drugs from a syringe, as shown in Figure 3.8(a). This is the reverse process of releasing the liquid drugs out of the reservoir, but because it is quasi-static process the test results will represent the actual drug dosage level. For implanted drug delivery it is body fluids surrounded environment. Instead of real serum or blood, we use phosphate buffered saline (PBS) solution to mimic the body fluids. The device is tested inside PBS and the reservoir is initially filled with drug powders. Through the outlets, drug powders will naturally diffuse into the PBS solution and at the same time the incoming PBS solution will gradually replace the volume inside the reservoir as shown in Figure 3.9(a). These experiments are not intended to include any advanced drug delivery system but solely provide different drug dosage levels to test the real time monitoring ability of the helix antenna sensors. In order to slow down and control the diffusion rate, any additional filter, membrane or micro-fluidic chip can be applied at the outlet.

Based on the simulation and fabrication process discussed in previous sections, optimized antenna sensors can be designed and fabricated for different reservoir sizes. During the in-vitro experiments the sensor performance is more predictable in the air-surrounded environment than in the fluid-surrounded environment. The effect of surrounding liquid materials is difficult to accurately represent in the simulation. For the implanted drug delivery monitoring demonstration, even though factors like the shape of the beaker, have all been included in the simulation, fine tuning of the feeding line is still necessary during experiment. It can be expected that for in-vivo test and for real applications inside human body, the implanted antenna sensor design will be even more challenging.

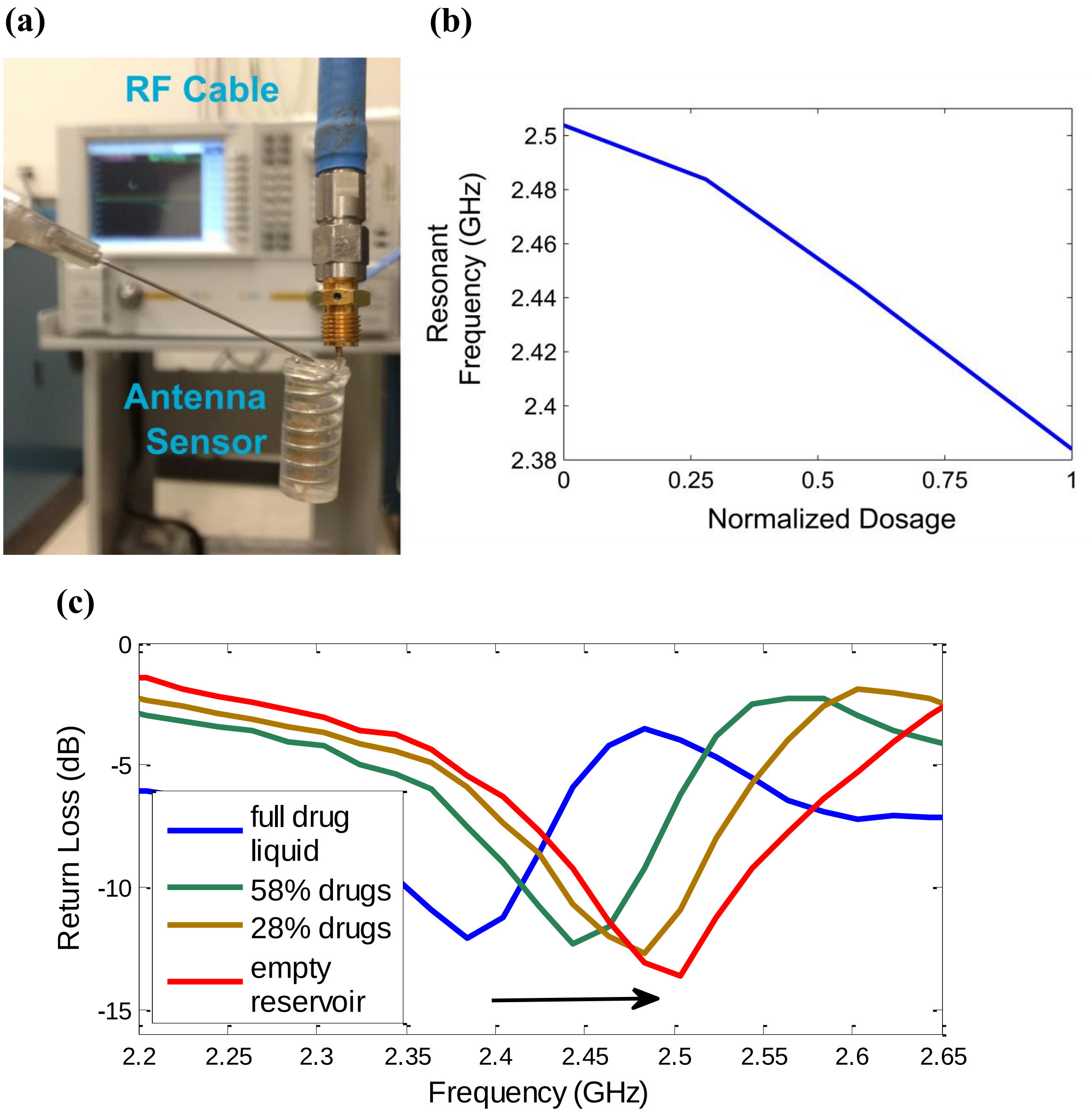

(Figure 3.8 continued next page)

Figure 3.8: In-vitro experiment on the dosage monitoring sensor for intradermal drug delivery applications: (a) The test equipment with for an 7 turn helix antenna sensor with liquid drugs (5% glucose solution) injected. (b) The measured sensitivity curve of the sensor. (c) The measured return loss of the sensor with different volumes of drugs filled in the reservoir.

One transdermal drug delivery monitoring sensor and one implanted drug delivery monitoring sensor have been realized. The transdermal one is a 7-turn helix antenna sensor with a 0.127 mL reservoir. It was designed to resonate at 2.4 GHz as the initial full liquid state and gradually shift up toward 2.5 GHz as the release process goes on. The whole procedure is a quasi-static process and the actual drug dosage in the reservoir is tractable throughout the experiment. The linearity of the antenna sensor is noticeable from the sensitivity curve shown in Figure 3.8(b), and Figure 3.8(c) shows the measured S_{11} of the antenna sensor at four different dosage levels. The sensitivity of the sensor is about 1.27µl/MHz.

The implanted sensor is a 8-turn helix antenna with a 0.221 ml reservoir. The measurement results show that throughout the drug release the antenna resonance frequency shifts from 2.5 GHz down to 2.41 GHz as shown in Figure 3.9(b). The sensor linearity is not tested because in the fluid environment the drug release is driven by natural diffusion so that the actual drug dosage inside the reservoir is hardly tractable during the release process. The average sensitivity of this sensor for implanted drug delivery is about 2.76 µl/MHz. Measurement results of Figure 3.8(b) and Figure 3.9(b) also indicate a relatively low Q for the antenna, which is possibly due to conduction loss introduced by the PDMS material and surrounding liquids as the return loss shows some global offset down from 0 dB across the whole frequency band.

(a)

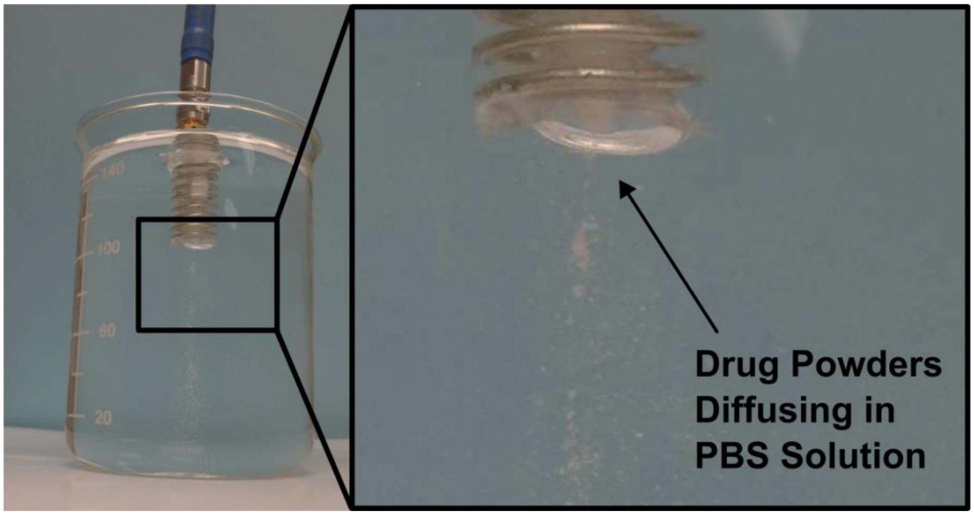

(b)

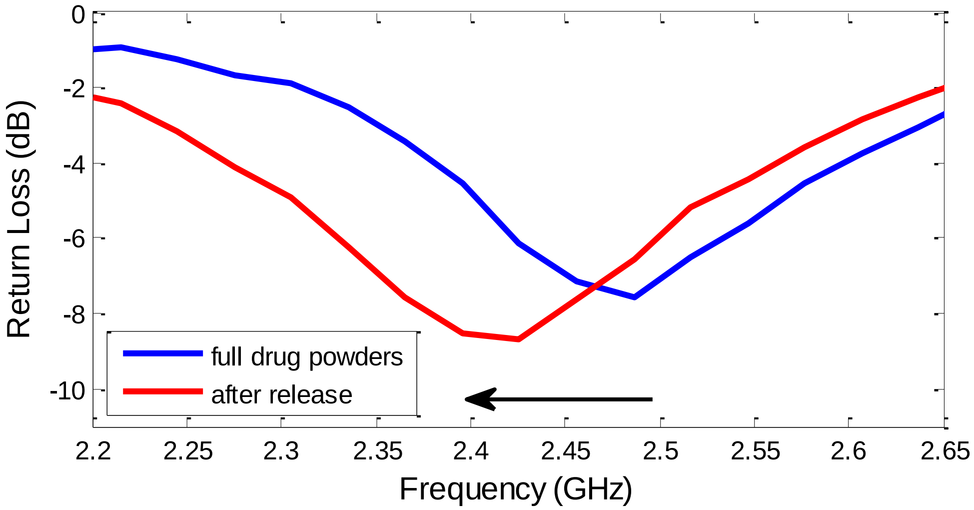

(Figure 3.9 continued next page)

Figure 3.9: In-vitro experiment on the dosage monitoring sensor for implanted drug delivery applications: (a) The experimental setup for an 8 turn helix antenna sensor loaded with solid drugs (resveratrol powders) inside a PBS solution surrounding environment. (b) The measured return loss of the sensor before and after the drugs released in the PBS solution.

3.5 RFID TRANSPONDER CIRCUITS AND MICROSYSTEM FOR ANTENNA BASED SENSORS

In the in-vitro test described in Section 3.4, test equipment like a network analyzer has been used for the comprehensive measurement of the antenna sensor performance. In practice, the complete system also needs specifically designed low cost RFID reader and transponder circuits integrated with the antenna sensor. Considering the fact that most controllable drug delivery devices also require some receiving antenna and receiver circuits for the drug delivery control, in this section a RFID transponder circuit architecture is proposed to combine the functionalities of drug dosage monitoring transmitter and drug delivery control receiver.

As shown in Figure 3.10, the antenna sensor itself is also served as a RFID transponder data communication antenna for the drug delivery control system. The power management unit contains some wake-up circuit to turn on the transponder if it has a battery, or some energy harvesting circuit if it is completely relying on external power source. After the transponder gets turned on, like any standard RFID system [102], [103], the reader first sends some commends to identify the transponder in which the identification information is stored in the state machine or memory unit. The central digital logic in the transponder will then follow and generate some reply signal, which will be modulated and sent back to the reader through the helix antenna. During the next step, the reader will send commend to the transponder to start monitoring the drug dosage level inside the transponder drug capsule, and it will enable the frequency synthesizer to sweep the frequencies within the band of interest. The reader will then compare the received power at those frequencies and determine the transponder antenna resonant frequency, which represents the drug dosage level. The detailed frequency synthesizer circuitry and sensor decision mechanism can be varied depends on the application precision requirements. The reader can also send commends to control the drug delivery process as the control unit is integrated.

As both drug control unit and frequency synthesizer in the transponder will be power consuming, comparing to general purpose RFID transponders, the power budget for the RFID transponder sensor/controller is prohibitively high. The state-of-art miniaturized battery technology, wireless powering technology, and ambient energy harvesting technology will help resolve such challenge and push the RFID drug delivery monitoring/control transponder into practice. In the next chapter, a novel harmonic transponder sensing system is realized enabling antenna based monitoring without the need of battery or specific energy harvesting circuits at the transponder.

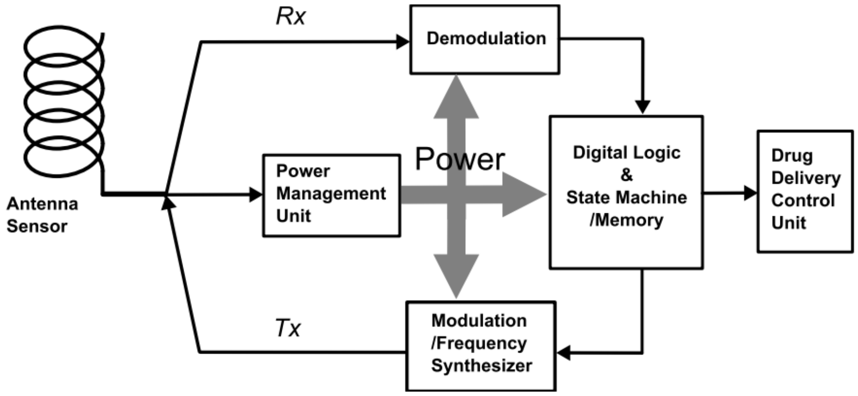

Figure 3.10: Block diagram of an RFID transponder microsystem integrated with antenna sensor and drug delivery control.

3.6 CHAPTER SUMMARY

This chapter proposed the concept of using miniaturized helix antenna as a RFID transponder wireless sensor to directly track the drug dosage inside a reservoir integrated with the antenna sensor. The sensor was designed based on cavity resonator perturbation theory and electromagnetic simulation using HFSS, fabricated with the PDMS packaged drug reservoir by utilizing a low cost molding process with the help of selective laser sintering, and tested in-vitro using an Agilent PNA network analyzer. The measurement results have shown high sensitivity and good linearity. Transponder microsystem block diagram is also specifically designed to be integrated with the antenna sensor and some drug delivery control unit. Such transponder sensor/controller can be used as a multifunctional node in the wireless health networks.

Chapter 4: Passive Harmonic Transponder Based Wireless Sensing System for Healthcare Ubiquitous Liquid Monitoring with μL Resolution

4.1 THE DEMAND AND CHALLENGE OF UBIQUITOUS WIRELESS LIQUID MONITORING IN HEALTHCARE

Dynamically and accurately monitoring the liquid-level is of importance in various home clinic and wireless healthcare applications, because a large number of medical care practices are related to liquid manipulation [104], [105]. For instance, for nutritional or therapeutic liquid intake, the liquid-level inside a container is usually checked each time for pharmaceutical compliance. For intravenous therapy, it requires the process being monitored to avoid any hazardous incident, such as the air embolism when the medicine is fully dispensed in the drip chamber or syringe. For controlled drug delivery or smart pills, the amount of drug remained in the capsule is a critical feedback information to assure the delivered dosage within certain therapeutic ranges that maximize the efficacy and also minimize side effects [106]–[109]. However, conventional monitoring, either for large container or small syringe, is based on human visual observation. High resolution liquid-level monitoring for miniaturized containers, on the other hand, are mostly performed by expensive detectors, such as optical sensors [110]. Therefore, low cost automatic real-time wireless monitoring of liquid-level would be helpful to alleviate the load of healthcare workers and to improve the overall healthcare efficiency. Such clinical function will be highly demanded especially in future aging society.

For ubiquitous wireless healthcare monitoring applications, battery is a major hurdle to further downsize the wireless sensor node and minimize the cost; thus for short distance applications, passive sensors are preferred over active sensors [111]. Passive radio frequency identification(RFID) transponder sensors have gained attention from academia and industry [112]–[118]. Especially, instead of having extra sensor modules, antennae on commercial RFID transponders can be used as the sensing agent for beverage liquid-level monitoring [117], [118]. However, these RFID transponder antenna sensors suffer from inability of absolute value sensing [117], [118]. For instance, the background interference (which commonly exists in the indoor environment), the sensing distance, and the input power will affect the sensor output. To achieve high-resolution and reliable wireless liquid-level sensing, alternative sensing transponders and systems are desired.

Another challenge for healthcare wireless liquid monitoring is sensor design. Unlike beverage bottle monitoring [117], [118], commercial RFID transponder antenna would not be suitable for most healthcare liquid monitoring applications, which have much higher miniaturization and sensing resolution requirements. For that the sensing antenna on the transponder must be specifically designed to serve the applications in healthcare. In chapter 3 a general 3-D helix antenna sensor design procedure has been presented, in this chapter we are seeking improvement to boost its sensitivity and resolution performance. Recently, metamaterials, which are artificial materials with engineered electromagnetic responses, have been proposed to make various miniaturized antennae based on the substrate[119], or coverage [120] of single/double negative materials. Moreover, the metamaterial-inspired electrically small antennas (ESAs), comprising of the LC resonant structures inspired from the unit element of metamaterials, can be more readily designed and physically realized compared to those metamaterial-based ESAs. It has been demonstrated that a driven electrically-small electric or magnetic antenna covered by metamaterial-inspired structures in its near field can be matched to a 50 Ohm source and have high overall efficiency. A similar concept of metamaterial cover or the so-called “cloaking device” has also currently proposed to maximize the received power of a small dipole antenna [121]. In this case, a reactive metamaterial cover can control the scattering cross-section of the ESA system associated with the antenna resistance (which inherently has a small value for an ESA) and cancel the reactive energy in the near field of ESA. Therefore, the conjugate matching can be achieved for the ESA system, providing the maximum power efficiency and potentially maximum sensitivity to liquid materials filled inside the antenna.

4.2 Frequency Hopping Enabled Passive Harmonic Transponder Antenna Sensing System

Here we propose a new sensing mechanism utilizing harmonic transponsor (transponder-sensor) comprising of a metamaterial-inspired compact 3-D liquid sensitive antenna to realize passive high resolution absolute accuracy wireless liquid-level monitoring. Historically, harmonic radar with electronic nonlinear tags has been used for tracking moving insects [122]. In our sensing system, the harmonic transponder converts the received frequency hopped signal 928 MHz band from an interrogator to its second harmonic at 1.804-1.856 GHz band. The harmonic tones containing liquid-level sensing information, can be potentially detected and decoded by a portable sniffer device (e.g. smart phone with 3G and LTE antenna covering 1.8 GHz) and therefore avoid direct coupling, background scatters and clutters at the fundamental frequencies. In addition, taking advantage of the FHSS (required by the communication protocol of UHF RFID signals[123]), its output becomes high dimensional data rather than single point data. This enables algorithm based post processing and machine learning, like in computer vision[124], [125], to achieve absolute accuracy sensing and decision because additional dimensions of the output bring redundant information that can tolerate variation of other factors, such as transponder sensor location and interference from near-field objects. We apply those concepts to realize a wireless medical saline liquid-level monitoring with μL resolution on a metamaterial-inspired ESA, which is, in some sense, similar to a miniaturized monopole antenna with a metamaterial-surface cover. The high quality-factor (Q-factor) feature of such subwavelength antenna would leak to a strong field localization[119], [126] and therefore the ability of reliably and sensibly detecting the liquid-level within the micro-liter range. This battery and digital circuit free sensing mechanism shows great potential in a broad range of healthcare applications, including pharmaceutical management, drug delivery control, drug compliance assurance, clinical research, as well as other non-healthcare fields which have the need of dynamically monitoring the liquid-level.

A high level illustration of the passive harmonic transponder and sniffer based liquid-level sensing system is shown in Figure 4.1. An interrogator transmits a frequency hopped signal with a predefined pseudo-random hopping pattern. Various kinds of liquid containers like bottle, dripping chamber, syringe, drug capsule or insulin pump, with different geometries and functionalities, can be equipped with a passive harmonic transponder to receive signals from the interrogator. The harmonic transponder has a nonlinear module that converts the signal to harmonic frequencies [$2f_1$, $2f_2 \ldots 2f_n$]. Such harmonic output is emitted from a specifically designed 3-D antenna operating at the corresponding harmonic band, whose radiation property across the band is highly sensitive to the liquid-level in the container which the antenna is attached to or packaged within. The re-transmitted harmonic signal is then detectable and decodable by a sniffer receiver operating in the harmonic band. In practice, the interrogator could be a 902.5-928.5 MHz UHF RFID reader with 50 frequency hop channels and a smart phone or tablet with the 1.8 GHz antenna could be utilized as the sniffer receiver. Nowadays either RFID interrogators or smart phones are accessible to cloud based computation and database, therefore the passive harmonic transponders can be wirelessly networked altogether to serve cloud sensing database and healthcare management.

The sensing mechanism of the harmonic transponder is illustrated in Figure 4.2. The interrogating signal among frequency hopping channels [f_1, $f_2 \ldots f_n$] has constant signal strength. Assuming other than the sensitive harmonic antenna, the rest of components in the system, such as interrogator antenna, transponder fundamental antenna, frequency multiplier, and sniffer receiver antenna, all have fixed frequency responses, then the received signal strength indicator (RSSI) at the sniffer receiver over the corresponding harmonic channels will discretely represent the sensing antenna resonant profile from $2f_1$ to $2f_n$, which is sensitive to the liquid-level shift. Frequency conversion on the transponder is necessary because at the fundamental frequencies there is strong direct coupling from the interrogator to the sniffer receiver, as well as background scattering in the environment; while at second harmonic the signals are exclusively from the harmonic transponder, thus are much clean signals with higher signal-to-noise ratio. Also, comparing to sensors with one-dimensional data, the n-dimensional RSSI vector provides abundant information to enable intelligent algorithm based decoding, therefore achieves robust and absolute accuracy liquid-level sensing even in the presence of moving human body interference nearby (which is very common in healthcare environment for implanted or on-body applications).

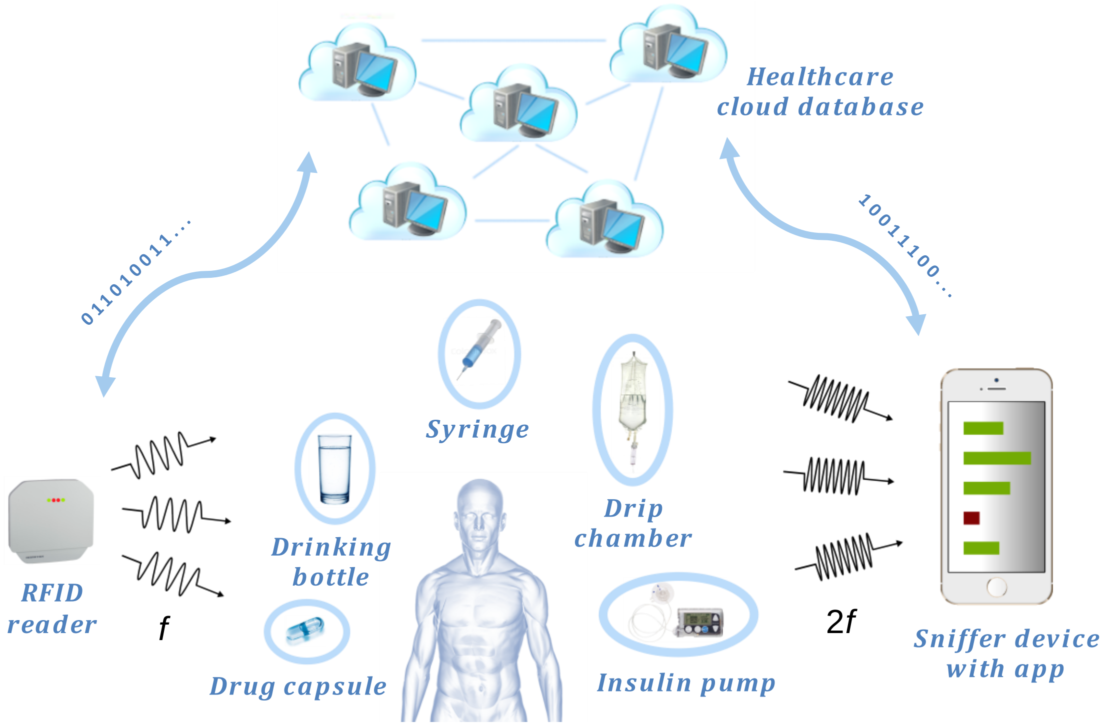

Figure 4.1: Application of passive harmonic transponder and sniffer based liquid level sensing system in a frequency hopped personal area network. In the sensing system, an interrogator transmits frequency hopped signals. Each medical liquid container is enclosed with a passive harmonic transponder that converts the signals to their harmonic band and retransmits them through a liquid sensitive 3-D antenna. A portable device may serve as a harmonic sniffer receiver to detect and decode the re-transmitted sensing signals at the harmonic bands from each transponder. Cloud based computation and database is connected to both the interrogator and the harmonic sniffer, serving as the hub for storing the sensing information and managing healthcare liquid manipulations in a whole healthcare facility.

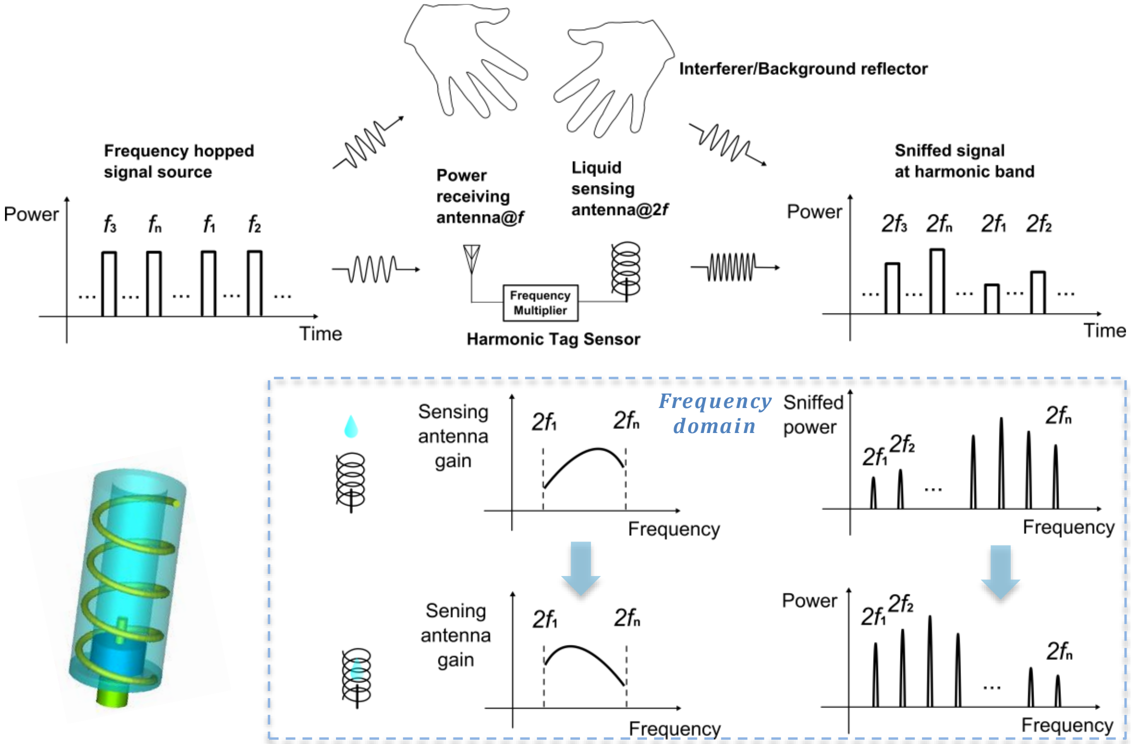

Figure 4.2: Passive harmonic transponder based liquid level sensing system sensing mechanism: The signal from the interrogator is frequency hopping among a set of channels [f_1, $f_2 \ldots f_n$] with constant signal strength; at the sniffer receiver end, the received signal strength indicator (RSSI) array profile over the harmonic spectrum represents the overall antenna gain of the sensing antenna, which is affected by the liquid level shift inside the container.

4.3 METAMATERIAL-INSPIRED COMPACT ANTENNA SENSOR IN HARMONIC TRANSPONDER

The liquid sensitivity boosting and sensor miniaturization are benefited from a metamaterial-inspired ESA-based design, where a short-stub monopole is surrounded by a helical coverage [119]. A conducting ground plane leads to the half-sized monopole and the helical coverage, due to the mirror effect. The advantage of this structure is shown through an electric field comparison of a monopole with (shown in Figure 4.3(a)) and without such helical coverage (shown in Figure 4.3(b)). In fact, for an asymmetric helical structure with direction of helix is reversed at the center [127], such as the structure in Figure 4.3(b), the magnetic dipole component is canceled at the resonance, and only the electric dipolar radiation polarized parallel to the helix axis is achieved, which is somehow similar to the lowest order spherical harmonic (TM_{10} mode) of a polarized subwavelength epsilon-negative (ENG) or plasmonic rod from the Mie scattering theory [119], creating the inductance necessary to establish the resonance within the electrically small structure. The small monopole stub at the center of the helical structure therefore provides a strong capacitive coupling between the coaxial feeding and resonant mode of the reactive cover.

Simulation of the antenna sensor with metamaterial-inspired (or “cloak”) structure is based on frequency-domain finite-element method (FEM) using the commercial software CST microwave studio software [128]. In the full-wave simulation, the package material with relative permittivity of 2.8 and loss tangent of 0.0035, were considered, and the short monopole and helical coverage are made of coppers with conductivity of 5.8×10^7 S/m. The liquid material in the simulation has a permittivity of 80, corresponding to most biomedical liquids such as phosphate buffered saline (PBS) buffer. The sensor nominal operation frequency is determined by the selection of helix parameters such as helical radius, number of turns and helical pitch angle determines the operating frequency range, and the length of short stud [119] also plays an important role to fine tune the antenna resistance and match the frequency multiplier circuit. The short stud length and its relative position to the helical cover also affect the local sensitivity and resolution performance of the sensor. In practice, the short stud length can be empirically tuned.

From the full-wave simulations in Figure 4.3(c), we found electric fields are anti-phase, intense and uniform within the helix, showing striking similarities to the resonant mode of an ENG-metamaterial rod [127] or a plasmonic particle at optical frequency [129]. Here the spatially distributed inductance of helical coverage may tune out the large capacitance of the electrically-small monopole stub when immersed in the liquid solution as shown in Figure 4.3(d). Since ESAs are typically characterized by large values of Q-factor and the dielectric liquid drug inside the coverage is immersed in strongly localized electric fields, according to the cavity perturbation theory, its resonant frequency may sensibly depends on the liquid level condition. Especially, the local liquid level sensitivity around the rod is boosted. For our antenna sensor designed at 1.85 GHz, 1uL liquid level change may cause a 2.5 MHz resonant frequency shift, according to the simulation result in Figure 4.3(e). In addition, like any ESA, the spatial radiation pattern of the antenna sensor is a typical isotropic one as shown in Figure 4.3(f).

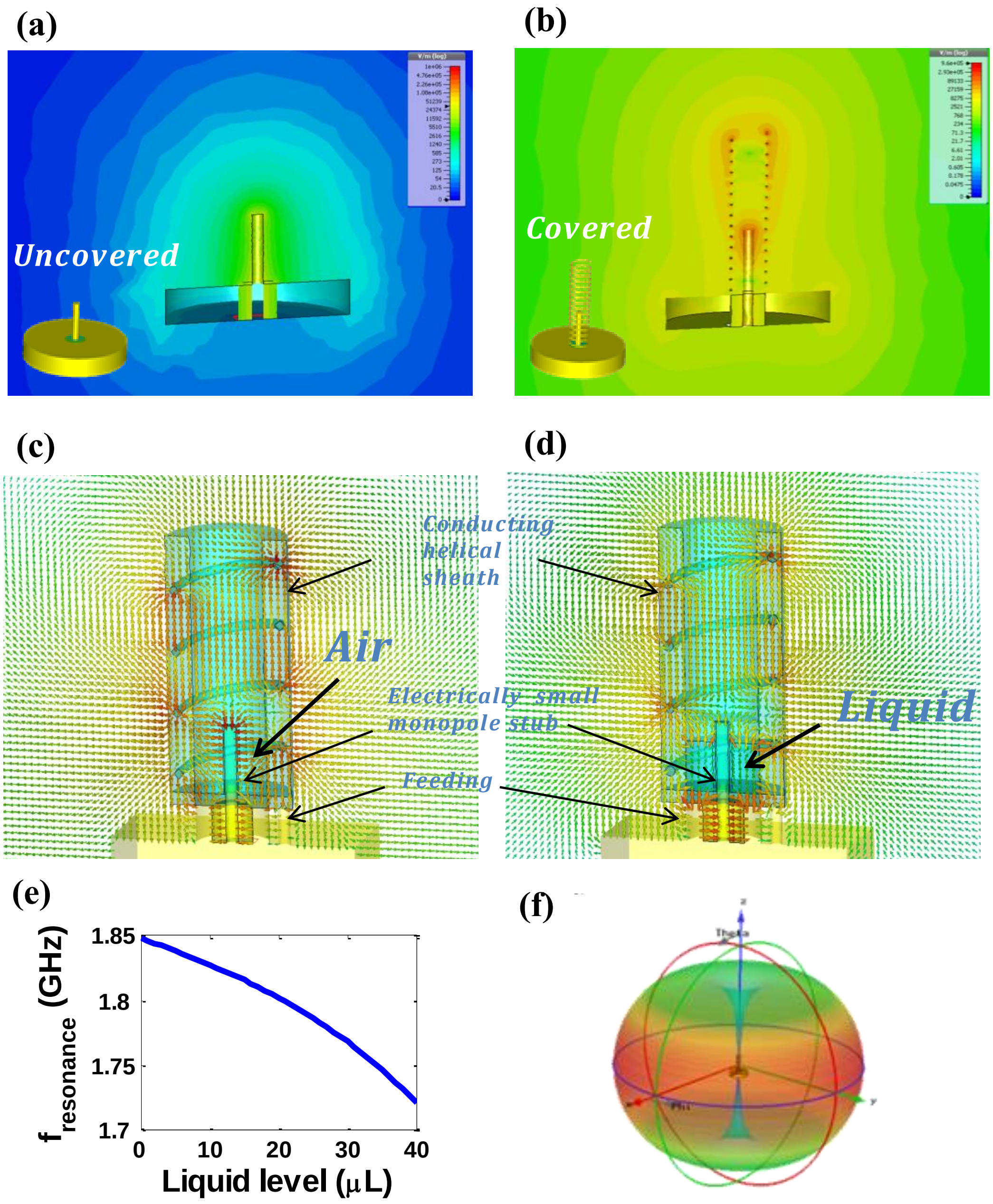

(Figure 4.3 continued next page)

Figure 4.3: Metamaterial inspired antenna sensor simulation (using CST Microwave Studio): (a) Geometry and simulated field distribution of monopole stud without the metamaterial-surface coverage. (b) is similar to (a), but for a cloaked monopole stud; now the field is significantly enhanced and strongly confined within the region around the stud, boosting sensitivity on detecting the amount of liquid filled inside the metamaterial-surface coverage. (c) Simulated electric field vectors for an empty metamaterial-inspired antenna sensor. (d) With liquid filled around the electrically small monopole stub, the resonant frequency becomes highly sensitive to the liquid-level. (e) The 3-D view of far field pattern at 1.85 GHz resonant frequency. (b) Simulated resonant frequency dependence of the antenna on liquid-level applied within.

The resonant frequency shift behavior of the meta-material inspired near-filed parasitic antenna can be also understood through a RLC resonant circuit model [130]. As shown in Figure 4.4(a), the monopole stub along with its near-filed surrounding structure forms a RLC resonator, in which the resistance R and capacitance C are affected by the liquid level ΔV and liquid permittivity ε_r [131]. Here ΔV is denoted the relative liquid volume inside the sensor reservoir to simplify the expression (ΔV=1 when liquid level is full). Both R and C are divided into two serially connected parts, one has permittivity of 1 as for free space, the other has permittivity ε_r as for the liquid occupied region. Because the antenna sensor is designed to be perfectly match to 50 Ω at 1.85 GHz, we could first determine that R_0=50 Ω and $1/(2\pi\sqrt{L_0C_0})$=1.85 GHz. The value of C_0 and L_0 can be further selected based on the realized quality factor Q of the antenna sensor. Having the initial model parameters, S_{11} variation of the circuit model can be calculated as shown in Figure 4.4(b), assuming full liquid level at 300 μL. The complete antenna sensor structure including the effect of liquid level not only on monopole stub but also on the helical cover[132] can be modeled as a more complicated circuit as shown in Figure 4.4(c), in which the simple RLC resonator represents the monopole stub, while the helical cover is modeled as an impedance transformer with its own RLC circuit (R_1,L_1,C_1) feeding to a load Z_L representing the overall load looking from the helical cover which radiates to the free space. Here the mutual inductance M is modeling the near-field evanescent wave coupling between the monopole stub and the helical cover. The simulated S_{11} and S_{21} (using Agilent ADS) under different liquid level are shown in Figure 4.4(d) and Figure 4.4(e), respectively. Even though the capacitance C_1 on the helical cover side is also set to be dependent on the liquid level, Figure 4.4(d) shows very similar S_{11} curves as Figure 4.4(b), indicating that the contribution to the frequency shifting behavior mainly comes from the monopole stub side. Comparing to the measured S_{11} variation of a realized antenna sensor shown in Figure 4.4(f), we can see that the simple circuit model can well predict the behavior of resonance shift, and roughly suggest the matching condition variation affected by liquid level shift. More accurate equivalent circuit model can be potentially achieved through further measurement data correlation investigation on the antenna geometry as well as package material conduction loss.

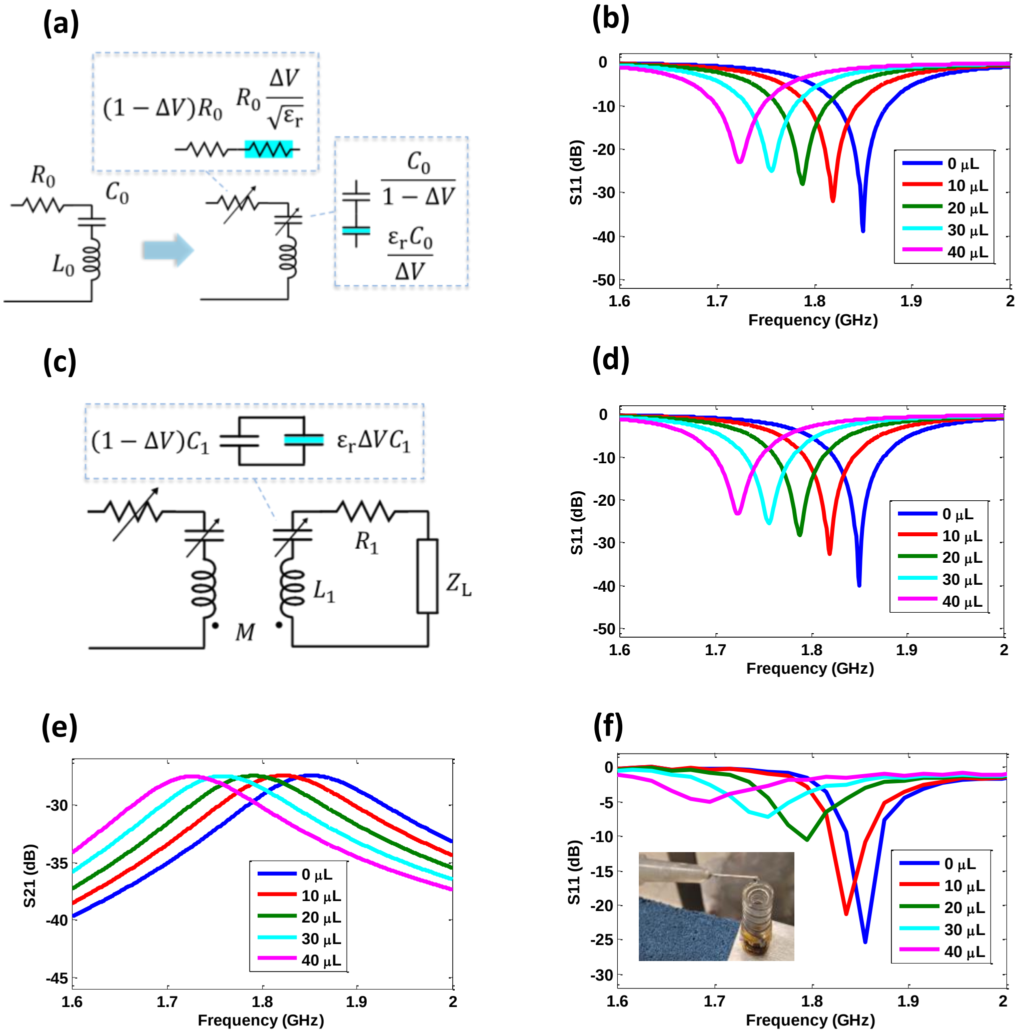

(Figure 4.4 continued next page)

Figure 4.4: Equivalent resonant circuit model of the antenna sensor. (a) the monopole stub along with its surrounding structure forms a RLC resonator, in which *R* and *C* are affected by the liquid level ΔV and liquid permittivity ε_r. (b) Calculated S_{11} of the circuit model with varying liquid level. (c) A complete circuit model including both monopole stub and helical cover structure. (d) The simulated S_{11} (using ADS software[133], with port 1 as the input coaxial feed) of the circuit in (c), which shows very similar results as in (b), indicating that the resonant shift is mainly affected by the stub and its surrounding structure, while the contribution from the helical cover is minor. (e) The simulated S_{21} (port 2 as Z_L) of the circuit in (c) affected by liquid level change. (f) Measured S_{11} of a realized antenna sensor structure with finite ground plane to compare with predictions from the circuit models.

4.4 EXPERIMENTAL REALIZATION OF PASSIVE UL LIQUID-LEVEL MONITORING

Similar to the fabrication process described in Section 3.3 of Chapter 3, the metamaterial-inspired (or “cloak”) structure is assembled within Polydimethylsiloxane (PDMS) package to save real estate for liquid reservoir. The metal wire antenna is fabricated using selective laser sintering based mold process in order to precisely produce the helical structure [109]. Starting with a reservoir mold and a package mold, the PDMS mixture liquids are filled in with the metal helix structure. PDMS with the molds are first cured at room temperature in a desiccator for more than one hour and then in a 125°C oven for about 40 minutes [109]. Putting the whole assembly in an environment with temperature below 0°C will help release the molds. The passive frequency multiplier selected here is a MiniCircuit MK-5 [134] with a low conversion loss from 20 MHz to 2 GHz. This frequency multiplier was packaged with metal shield which can also provide antenna ground plane. One end of the metal wire has to be connected to the ground, either through soldering it to the metal cover of the frequency multiplier or through Ohmic contact of the metal wire with the outside thread of the SMA connector on the frequency multiplier. The metal stud length can be adjusted to fine tune the matching condition from antenna to frequency multiplier output port.

Figure 4.5 shows the sensor prototype and the experimental setup in an indoor environment. The fabricated antenna sensor was connected to the output port of the passive frequency multiplier. The input port of the frequency multiplier connected to a folded monopole antenna designed at 900 MHz for fundamental tone receiving. Because the fundamental tone antenna may have loading effect to the frequency multiplier, this antenna was characterized together with the frequency multiplier, as shown in Figure 4.7. The transmitting module in the demonstration is a commercial RFID reader antenna connected to a signal generator, which emulates the frequency hopped ASK signal source as from an UHF RFID reader. The sniffer receiver module was emulated by a wideband horn antenna connected to a PXA spectrum analyzer to detect and characterize the harmonic sensing signal reradiated from the tag. Standard medical purpose PBS solution was injected to the PDMS reservoir from a syringe with 10 μL per liquid load as the smallest increment during the liquid-level sensor demonstration.

A Labview program is controlling the signal generator to produce a narrow band ASK signal with its carrier frequency hopping at least every 400 ms, compatible with the Class 1, generation 2 (C1Gen2) UHF RFID protocol [135]. The allocated band in U.S. is 902.5-928.5 MHz with 500 kHz channel bandwidth (excluding the two guarding bands) with totally 50 channels for frequency hopping [135]. The hopping is following a predefined random permutating pattern. The base band data used for test is PRBS9 pseudo random binary sequence with 100 kHz symbol rate. As a result, the output harmonic signal will be hopping among 1.805-1.857 GHz with 1 MHz channel bandwidth under the same permutating order. The hopping range can be changed by the Labview program, for example, from 850 MHz to 950 MHz for wide band demonstration. In addition, the modulation type can be also set to FSK,PSK, FM, AM or PM for more general demonstration.

The measured sensing data is summarized in Figure 4.6. Figure 4.6 (a)-(c) are the 3-D bar charts of RSSI against both time and frequency under frequency hopping. The frequency hopping sequence is set to be randomly permutated among the 50 channels from 902.75-927.75 MHz and the resolution bandwidth of the sniffer receiver is set to be 0.5 MHz to match the ASK signal channel width [135]. The received harmonic signal thus has the same hopping pattern at harmonic frequencies from 1.8055-1.8555 GHz. Variations of harmonic signal strength can be represented by observing the frequency spectrum as the RSSI sequence is recorded and shown in Figure 4.6(d)-(f). The sensor response is fine tuned to fix the peak around 1.855 GHz when the reservoir at the sensor is empty (Figure 4.6(d)). By adding 10 μL and 20 μL of liquid, the second harmonic peaks are shifted to 1.83 GHz (Figure 4.6(e)) and 1.805 GHz (Figure 4.6(f)), respectively. Therefore, the realized sensitivity is about 25 MHz/10 μL. If the channel index of the harmonic peak is used as a digital output, the sensor resolution is 0.4 μL.

Previous demonstration is compatible with C1-Gen2 protocol in United States; while worldwide operating band ranges from 840 MHz to 960 MHz and some commercial products actually covers the whole UHF RFID band. For that a comprehensive sensor performance is tested when the frequency hopping has a wider range of 850 MHz to 950 MHz without being restricted by specific local protocol. Figure 4.10(a) shows the measured RSSI array by the sniffer receiver over the whole UHF RFID band and the corresponding harmonic band. The RSSI array variation at the fundamental frequency band is hardly perceptible because the received power at those frequencies is dominated by the direct coupling from the RFID reader antenna and the scattering from nearby objects. In contrast, as the liquid-level increased from 0 μL to 50 μL, the RSSI array at the second harmonic shows distinct profile variation for each 10 μL increment. This validates the advantage of the harmonic transponder over conventional transponders as a passive sensing platform.

However, the harmonic RSSI peak shift is distorted as the liquid-level reaches 40 μL. This phenomenon is caused by the narrow band effect from the interrogator and transponder fundamental tone antenna in the signal path, and the casue is verified through a detailed characterization along the signal path (shown in Figure 4.7 and Figure 4.8). To eliminate this effect and increase sensor dynamic range, in principle, any antenna in the sensing system other than the sensing antenna has to be wideband. Here, instead of using high cost wideband antennae, we take advantage of its multi-dimensional nature of the output and utilize a data smoothing and narrow band effect compensation algorithm for the sensor decoding and get an overall linear sensing performance over a large range.

The multi-dimensional RSSI array data is first smoothed by a robust local regression using weighted linear least squares and a 2nd degree polynomial model. This regression assigns zero weight to data outside six mean absolute deviations to rule out abrupt interference from the environment. Secondly, the peak channel frequency $\mathrm{f_{peak}}$ of the smoothed RSSI data is identified through a peak detection algorithm. Thirdly, a compensated peak channel frequency $\mathrm{f_{peak\_comp}}$ is calculated by a narrow-band-effect compensation algorithm:

$$\mathrm{f_{peak\_comp}} = \begin{cases} \mathrm{f_{peak}} - w(\mathrm{f_{LB}} - \mathrm{f_{peak}})/{\alpha_\mathrm{L}}^2, & \mathrm{f_{peak}} < \mathrm{f_{LB}} \\ \mathrm{f_{peak}}, & \mathrm{f_{LB}} \le \mathrm{f_{peak}} \le \mathrm{f_{HB}} \\ \mathrm{f_{peak}} + w(\mathrm{f_{peak}} - \mathrm{f_{HB}})/{\alpha_\mathrm{H}}^2, & \mathrm{f_{peak}} > \mathrm{f_{HB}} \end{cases}$$

where w is a constant weight coefficient, α_L and α_H are the first order polynomial fitting coefficients for the data in the range of ($\mathrm{f_{peak}}$ - Δf, $\mathrm{f_{peak}}$) and ($\mathrm{f_{peak}}$, $\mathrm{f_{peak}}$ + Δf), correspondingly, where Δf can be assigned with a reasonable value, e.g. 25 MHz, for slope tangent calculation. Having the compensated peak channel frequency, the final step is to map $\mathrm{f_{peak\_comp}}$ on the resonant frequency to liquid-level dependence curve associated with the antenna sensor like the one shown in Figure 4.4(b), and get the readout liquid-level value in μL. The final sensor readout result is summarized in the embedded subplot of Figure 4.10(a).

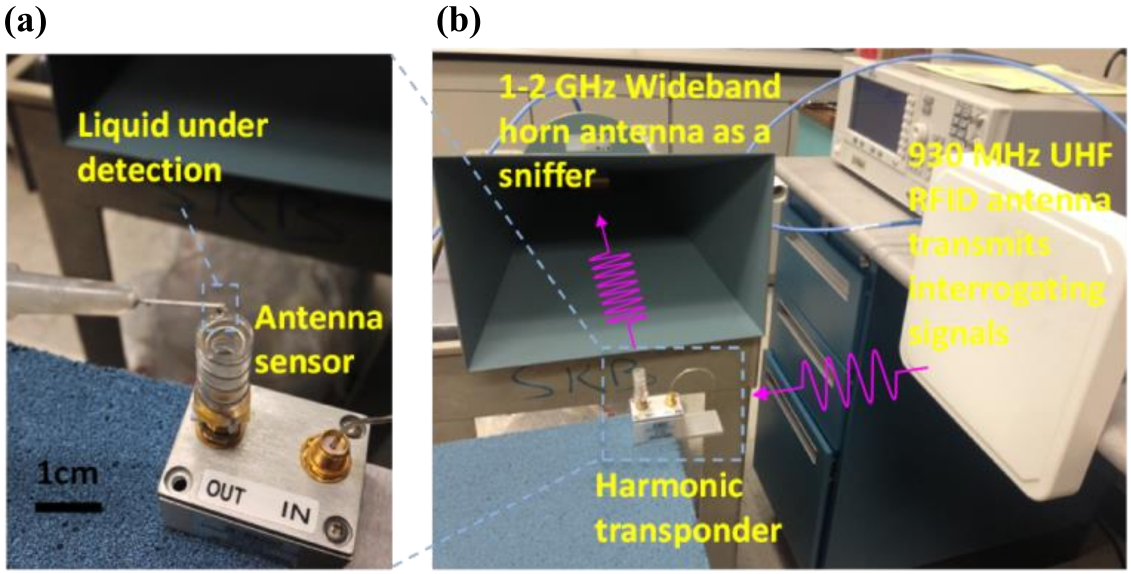

Figure 4.5: Experimental setup for conceptual demonstration of Passive harmonic transponder based liquid level sensing system: (a) Picture of a fabricated enhance wave meta-material cloak antenna sensor, which can detect μL level liquid applied from a syringe (with 30-gauge needle) to the enclosed PDMS packaged cylinder container; (b) picture of a passive wireless liquid monitoring system tested in indoor environment.

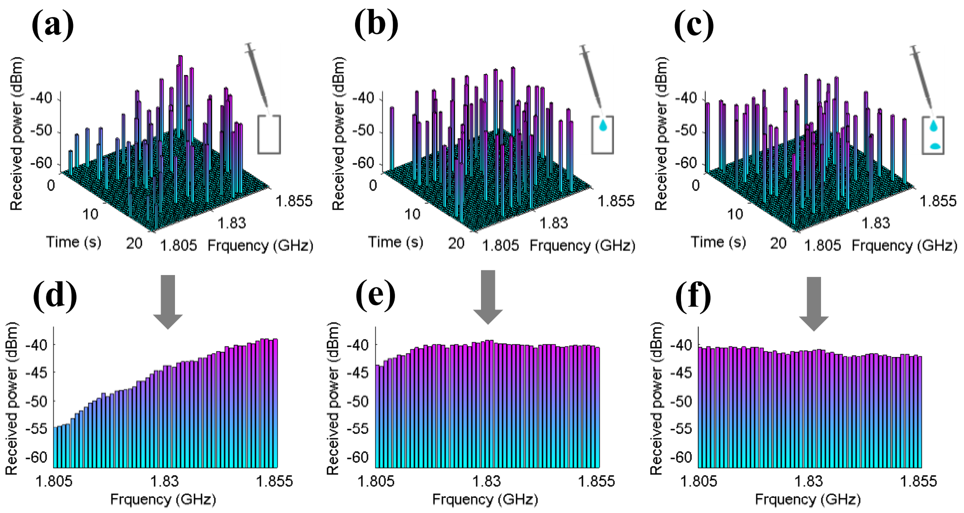

Figure 4.6: Demonstration of passive harmonic transponder wireless liquid monitoring with frequency hopped 902.75-927.75 MHz UHF RFID signal. (a) When there is no liquid in the reservoir, the 3-D bar chart shows the RSSI array on both time and frequency domain. (b) The 3-D bar chart of the second harmonic RSSI array when there is 10 μL PBS solution in the reservoir (c) The 3-D bar chart of the second harmonic RSSI array when applying 20 μL PBS solution to the reservoir. (d) The corresponding 2-D bar chart of (a) showing the RSSI array on frequency domain, with peak at 1.855 GHz. (e) The corresponding frequency domain 2-D bar chart of (b), the peak is shifted to around 1.83 GHz. (f) The corresponding frequency domain 2-D bar chart of (c), the peak is now 1.805 GHz. For a 50-channel frequency hopping signal, this result indicates a 0.4 μL resolution if the index of the peak channel is used as the digital indicator.

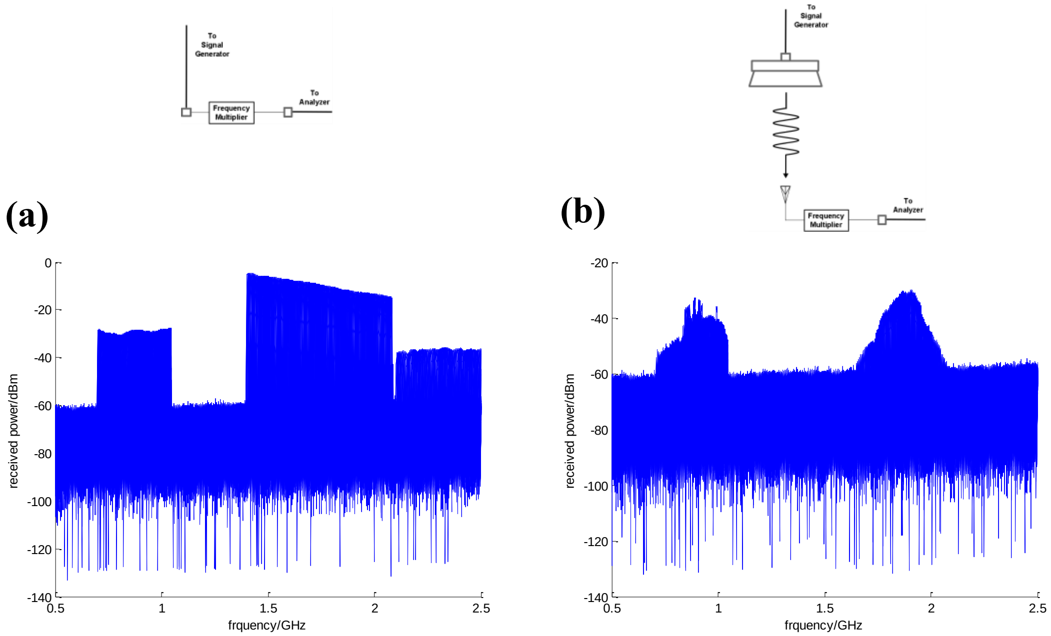

Figure 4.7: Interrogator and fundamental antenna characterization. (a) Frequency multiplier test under frequency sweep from 700 MHz – 1.05 GHz; the overall conversion gain (including cable loss and other system loss) over the second harmonic band is from -18 dB to -27 dB; the gain at fundamental bands and third harmonic band is around -40 dB and -50 dB, respectively; (b) Adding the RFID reader antenna and fundamental tone receiving antenna at the tag, the overall spectrum response under frequency sweep; now the overall conversion gain generally shows narrow band feature with relatively flat peak around 1.8-1.9 GHz, which is good for UHF RFID sensor. As the RFID reader antenna not broadband, there is no need to design a wideband receiving antenna at the tag. A coarse 3 MHz resolution bandwidth is used here to allow a faster frequency sweep, so the noise floor levels up to -60 dBm; but it in general won't affect the signal characterization.

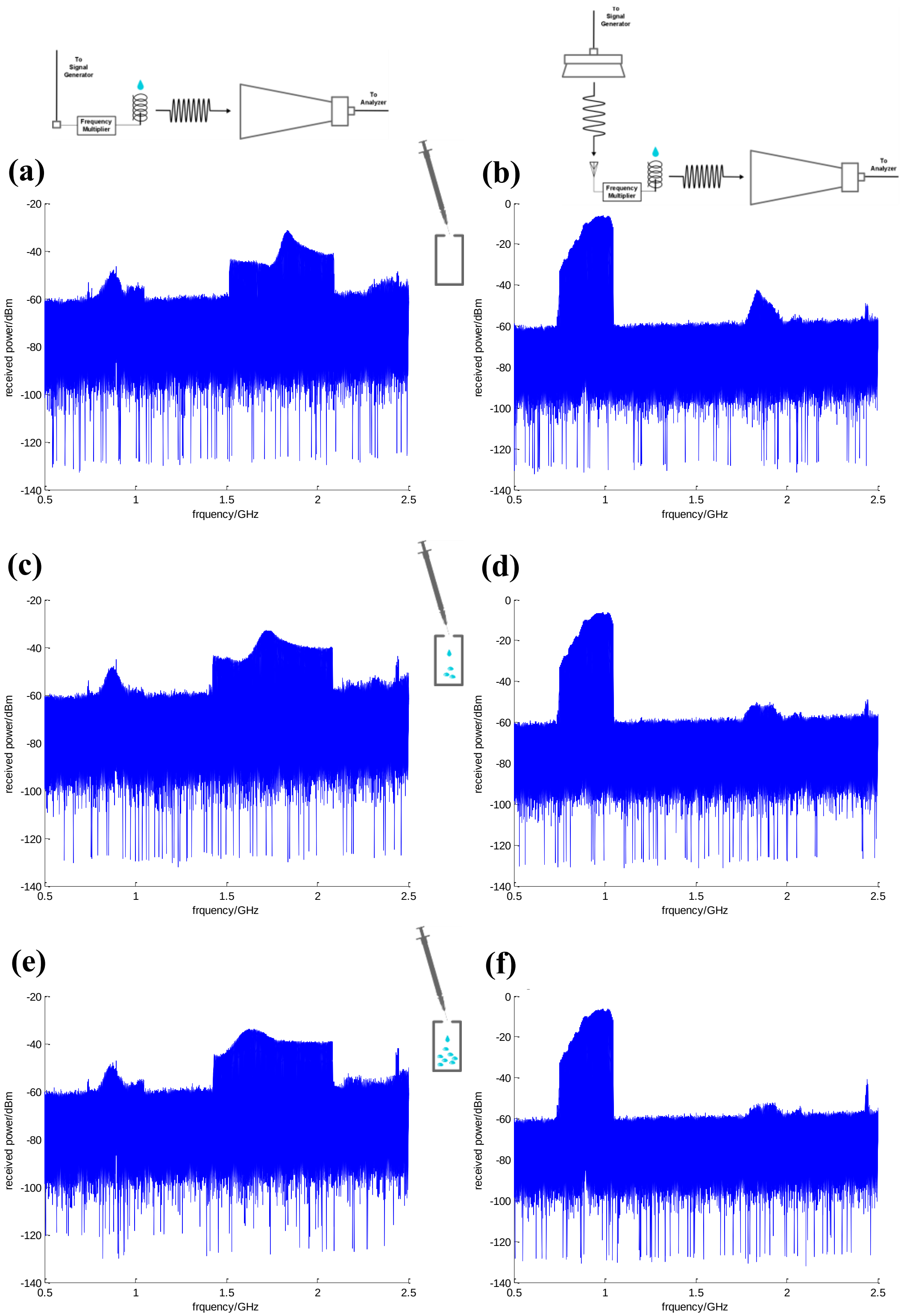

(Figure 4.8 continued next page)

Figure 4.8: Broadband range transponder re-transmitting antenna sensor characterization. (a) Antenna transponder sensor test with frequency multiplier under frequency sweep from 700 MHz – 1.05 GHz; the harmonic peak is around 1.85 GHz with an empty reservoir; (b) Adding the RFID reader antenna and fundamental tone receiving antenna at the transponder to complete the passive wireless sensing system test. The overall spectrum response under frequency sweep shows a peak around 1.85 GHz, which matches the peak in (a). (c) After applying 40 μL liquid to the reservoir, the peak of the antenna sensor response shifts to 1.72 GHz; (d) The complete passive wireless sensing system now shows a relatively weak and flat response due to the narrow band effect from the interrogator and fundamental antenna as shown in Figure 4.7(b). (e) After the liquid level added up to 80 μL in the reservoir, the peak of the antenna sensor response further shifts to 1.62 GHz, while the profile above 1.8 GHz is almost flat; (f) The complete the passive wireless sensing system does not change significantly from (d), this can be explained by the comparison of (c) and (e), which has similar response from 1.8 to 1.9 GHz as the peak already shifted toward much lower frequencies.

4.5 ROBUST HIGH DIMENSIONAL DATA PASSIVE WIRELESS SENSING WITH ABSOLUTE ACCURACY

The high dimensional received harmonic RSSI array sensing data contains redundancy for liquid-level sensing decision. In fact only after a few hops a correct decision of the peak frequency can be made through the regression algorithm. As shown in Figure 4.9, after 10 hops, 20 hops and 50 hops, the regression curve and peak channel decision shows similar results for liquid level of both 0 μL and 10 μL. Such “free” redundancy is provided by the FHSS feature which is a requirement of the UHF RFID protocol. Similar to computer vision which turns the imaging sensing data into insight, here more redundancy means better robustness liquid level sensing with absolute accuracy that tolerates other variations.

The first problem it resolved in passive wireless sensing is distance dependence, i.e. absolute signal strength depends on the receiver-to-sensor distance. For multidimensional output, the sensor decoding, by contrast, is based on relative signal strength. As shown in Figure 4.10(b), when the receiver is moved away from the sensor, the profile and the peak frequency of harmonic RSSI array is largely preserved even though the absolute signal strength decreases drastically. Communication channel fading becomes observable at a 2.5 m sniffer-to-interrogator distance. But as the sensor output is a 50 element array, the data smooth algorithm can minimize the sensing error and still retrieve the correct liquid-level data. The noise level in our demonstration under 0.5 MHz resolution bandwidth is -75dB and the signal generator provides a 10 dBm power signal, which enables a sensing range over 3 meters according to Friis’ equation [77]. If with maximum available UHF RFID interrogating power at 30 dBm, the sensing range can cover even longer distance.

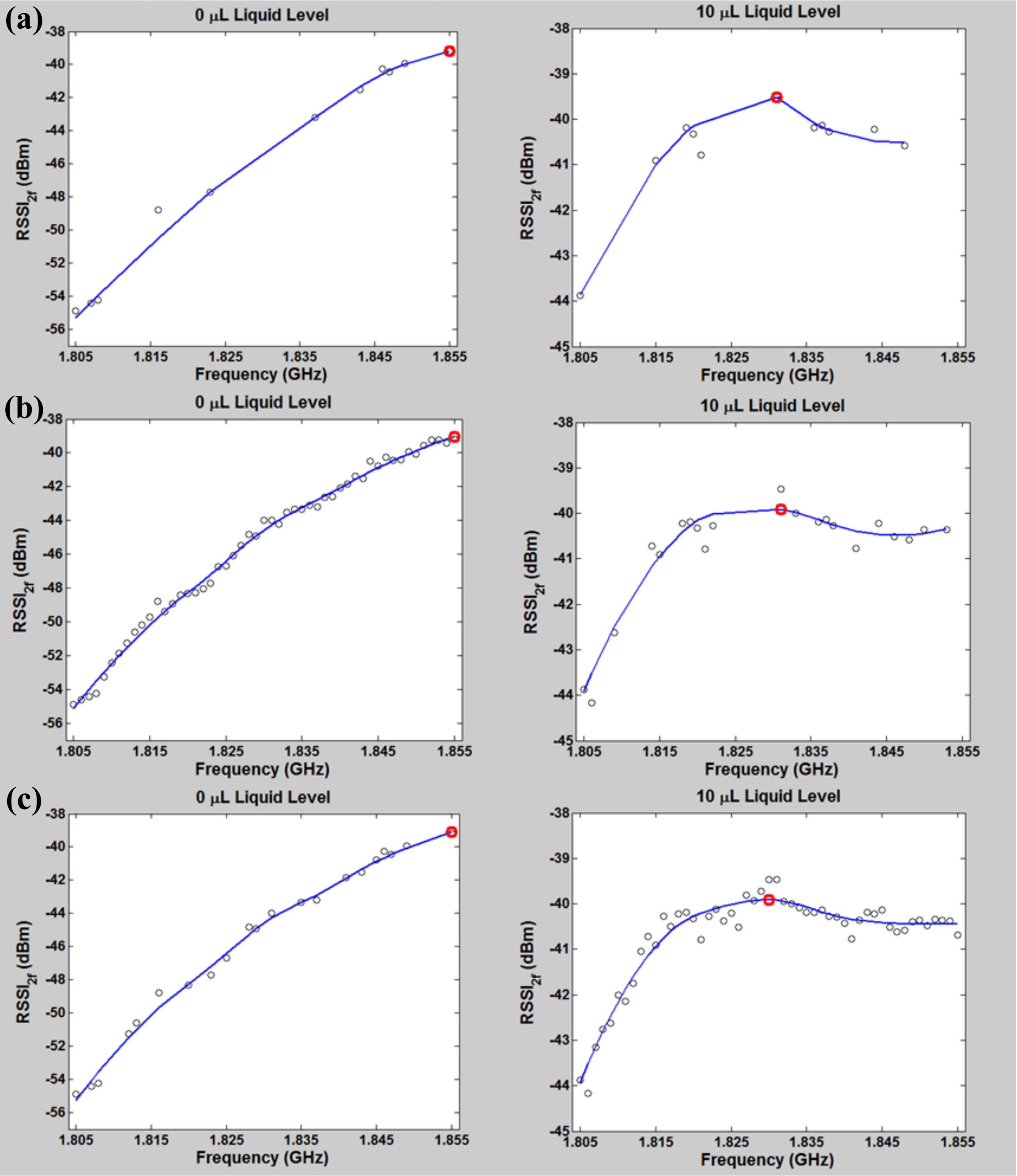

(Figure 4.9 continued next page)

Figure 4.9: Redundancy of the passive sensing from the frequency hopping spread spectrum. (a) The regression curve and the peak channel decision after 10 hops for liquid level of 0 μL (left) and 10 μL (right); (b) The regression curve and the peak channel decision after 20 hops for liquid level of 0 μL (left) and 10 μL (right). (c) The regression curve and the peak channel decision after 50 hops for liquid level of 0 μL (left) and 10 μL (right).

In body area networks, the human body is a time varying interferer that may severely degrade the wireless communication performance. This is another problem resolved by the multi-dimensional RSSI array. As shown in Figure 4.11, when a human body with constant movement is a few centimeters away from the sensor, the overall harmonic signal strength degrades, but the redundant information of the multi-dimensional output again ensures the robustness of the passive wireless sensing system. Similar benefits can be applied to implanted wireless sensors.

Another absolute sensing advantage we have verified is its independence of signal source. Transmitting signal power, signal modulation type, and signal frequency hopping channel width will not significantly affect the sensing performance. The measurement data in Figure 4.10(a) is associated with ASK-modulated signal, while that in Figure 4.10(b) is single tone sinusoidal signal. It is evidently seen that they present similar profiles and peak frequencies of the RSSI array. A more detailed comparison of the RSSI array with popular modulation types (single tone, ASK, FSK, PSK, AM and FM) is shown in Figure 4.12. In Figure 4.11, the frequency hopping channel width is 2 MHz instead of 0.5 MHz, and the resolution bandwidth of the receiver is 3 MHz instead of 0.5 kHz, the degradation on the sensor performance remains unnoticeable. This great flexibility may potentially lead to cross-system or cross-protocol platforms for the ubiquitous wireless networked monitoring.

Our demonstration presents a digital circuit free prototype at UHF RFID band, but the concept can be utilized and integrated with other technologies and systems for different applications. For example, having a conventional RFID IC chip on the transponder, identification may be performed at the same time with harmonic sensing, where the reflected ID data path is still picked up by the interrogator. Alternatively, if using a radar-like highly directional interrogator, localization information of the transponder may be retrieved along with the liquid level information. In addition, UHF RFID is not the only suitable platform, other communication protocols with spread spectrum techniques, such as Wifi, Bluetooth, and LTE, may all have their own transponders and sniffers. Overall, this work will have great potential to promote ubiquitous wirelessly networked monitoring in healthcare and other industrial fields.

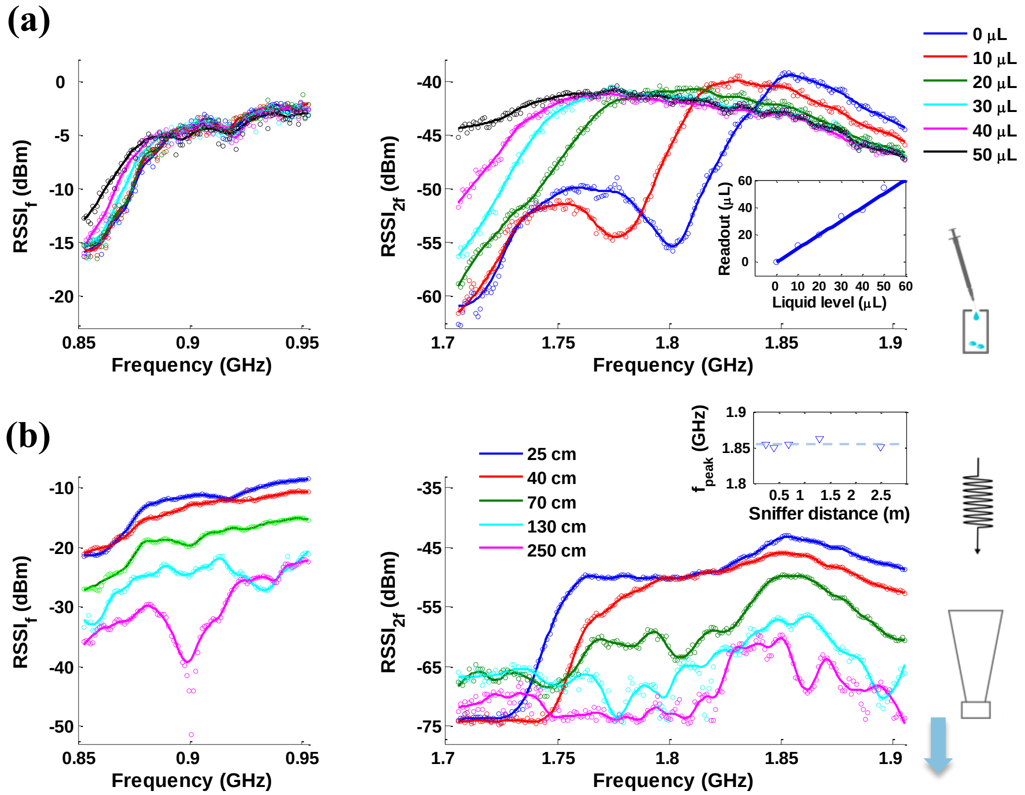

Figure 4.10: Comprehensive demonstration of the sensing system with wider frequency hopping range covering the whole global UHF RFID band as well as multi-dimensional output post-processing algorithm. (a) RSSI array variation at both fundamental tone (left) and second harmonic tone (right) for liquid-level applied from 0 μL to 50 μL. The sniffed fundamental tone cannot be used for sensing due to strong direct coupling and background scatters, while the second harmonic tone shows distinct variations when the liquid-level changes. The small subplot on the right summarizes the algorithm post-processed readout values, showing an overall linear passive sensing performance. (b) RSSI array variation for different sniffer-to-transponder distance from 25 cm to 250 cm, with liquid-level fixed at 0 μL. The peak frequency is consistent around 1.85GHz, indicating distance independence.

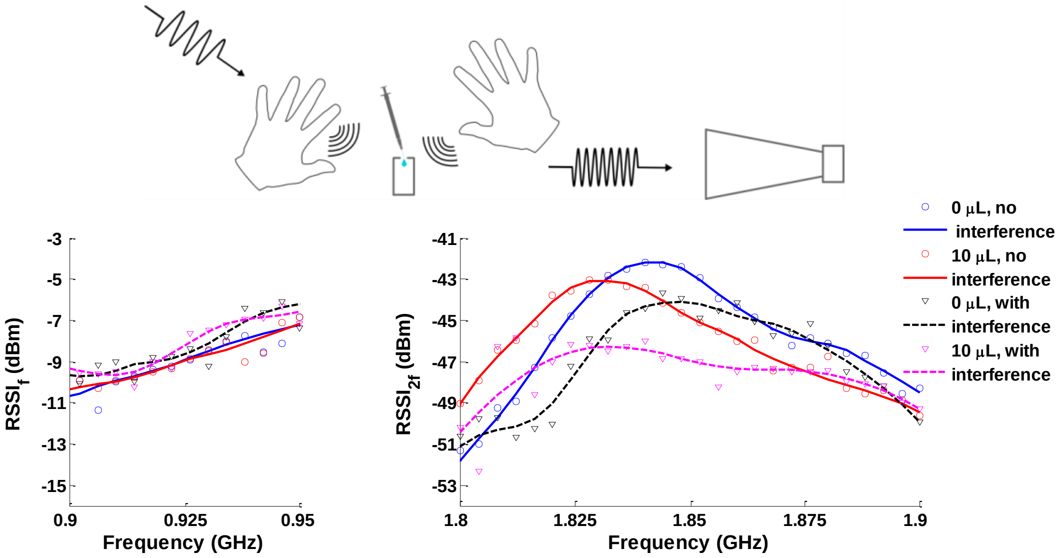

Figure 4.11: Effect of human body near field interference on passive sensor. The RSSI array variation at second harmonic tone (right) shows that human body interference affects the signal strength, but the peak position of the smoothed fitting curve is preserved and the peak shift is still distinct when liquid-level changes, demonstrating a robust sensing with absolute accuracy.

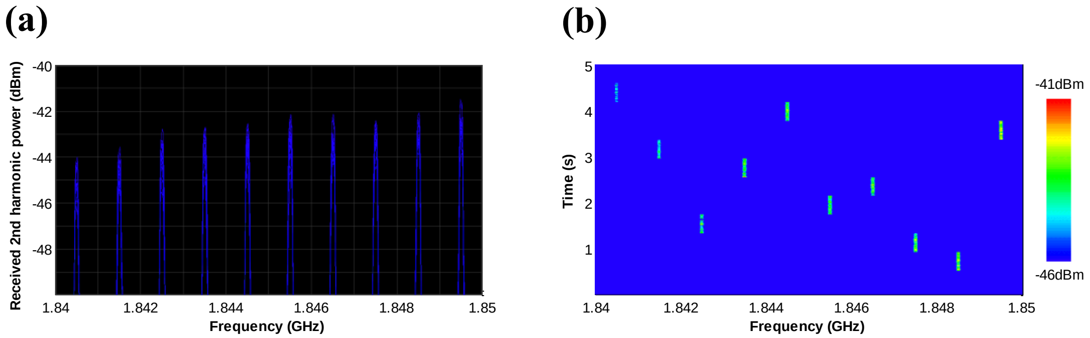

(Figure 4.12 continued next page)

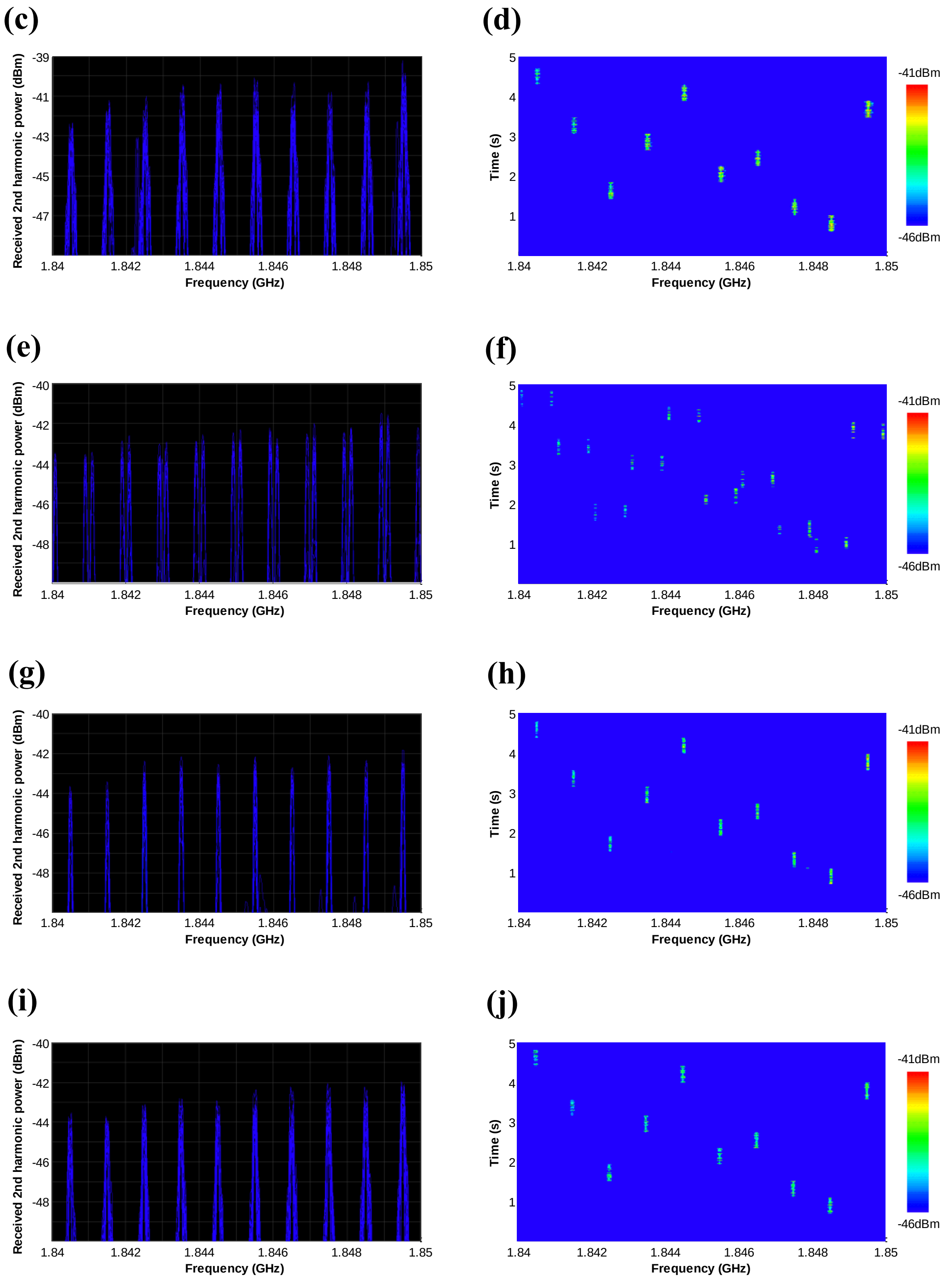

(Figure 4.12 continued next page)

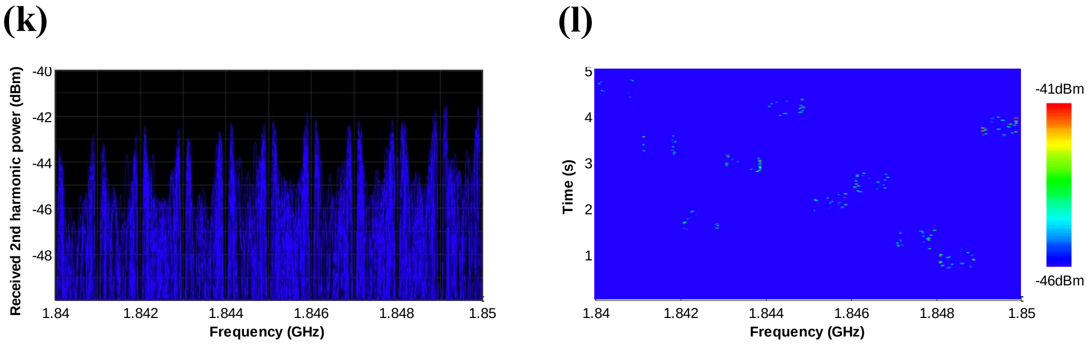

Figure 4.12: Compatibility verification of frequency hopped harmonic sensing mechanism with different digital and analog modulations. The hopping range is set to 920 MHz to 925 MHz (1.84 GHz to 1.85 GHz harmonic band) among 10 channels, the spectrum analyzer resolution bandwidth is set to 100 kHz to better view signal modulation details. (a) Spectrum density and (b) spectrogram of the received harmonic signal with single tone sinusoid. (c) Spectrum density and (d) spectrogram of the received harmonic signal with ASK signal (90% modulation depth with 100 kHz data rate). (e) Spectrum density and (f) spectrogram of the received harmonic signal with frequency shift key (FSK) signal (90% modulation depth with 100 kHz data rate). (g) Spectrum density and (h) spectrogram of the received harmonic signal with binary phase shift key (BPSK) signal (10 kHz data rate). (i) Spectrum density and (j) spectrogram of the received harmonic signal with amplitude modulation (AM) signal (90% modulation depth with 100 kHz data rate). (k) Spectrum density and (l) spectrogram of the received harmonic signal with frequency modulation (FM) signal (90% modulation depth with 100 kHz data rate).

4.6 CHAPTER SUMMARY

We have successfully realized zero-power wireless liquid-level monitoring at the μL-scale. The proposed sensor system employs a new concept of frequency hop harmonic transponder sensor, which uses frequency hopping signal to retrieve the response spectrum of a harmonic transponder antenna. The harmonic transponder receives frequency-hoped signal and coverts it to its second order harmonic, avoiding strong direct coupling and background scatters in the environment. The transponder antenna is a metamaterial-inspired, 3-D electrically-small resonant structure, for which the frequency response is designed to be highly sensitive to the liquid-level inside. The sensing system is experimentally demonstrated through a UHF RFID compatible prototype. To our knowledge, it is the first work that shows passive wireless liquid sensing with μL resolution. In addition, the absolute-accuracy sensing capability that tolerates distance variation as well as human body proximity interference is the new feature very important in on-body and implanted applications. This work will have great potential to promote ubiquitous wireless liquid monitoring in healthcare and other industrial fields.

Chapter 5: Chemically-Gated Graphene Modulator for Nanomaterial Harmonic Transponder Sensors

5.1 NANOMATERIAL BASED SENSORS FOR UBIQUITOUS NANOSENSOR NETWORKS

Advanced nanostructures like two-dimensional carbon nanomaterial graphene [136], with their single molecular level sensitivity in chemical and biosensors [137]–[142], may establish the foundation of future ubiquitous nanosensor networks [143], [144]. Normally, sensing and modulation are separate functions in a communication system [145], [146]. For example, a microphone in a Bluetooth headset [147] is detecting acoustic signals and integrated with other modulation (either digital or analog) interfaces at a reasonable cost. However, for nanostructure-based sensors [137]–[141], their small size and heterogeneous feature against conventional solid-state electronic devices make the integration challenging [148], [149]. In order to integrate nanomaterial sensors with commercial silicon based modulation interfaces, complicated post-transfer process must be performed [149].

Besides high mobility and high sensitivity, graphene devices also have special ambipolar electro-hole dispersion [136], [138], [141], which results in non-linear characteristic on its drain current to gate voltage dependence. Based on this unique property, special modulation functions such as full-wave rectifying, frequency mixing, amplitude modulation (AM), frequency modulation (FM), and phase modulation (PM), which are not directly achievable for conventional semiconductor materials [150]–[154], can be realized on a graphene device. Here, we propose an alternative modulation mechanism utilizing chemical gating effect instead of electrical gate voltage to modulate a carrier signal directly by the substance that a graphene field effect transistor (GFET) is exposed to. This monolithic all-graphene paradigm that virtually performs chemical sensing and signal modulation *in-situ* may be desired for ubiquitous sensor network applications to reduce their integration complexity and cost.

5.2 GRAPHENE CHEMICALLY-GATED MIXED MODULATION CONCEPT

For most real-time graphene sensor demonstrations, the sensor output is either in terms of direct current (DC) or resistance which is one-dimensional (1D) signal [137]–[142], [155]–[158]. Another advantage of the proposed chemically gated modulation for nanomaterial sensor application is its two-dimensional (2D) output signal. Lee et al. have demonstrated that the electrically gated modulation on graphene has a transition from AM to FM, i.e. from fundamental tone to second harmonic tone [154]. Here we will show that such transition is not abrupt, rather the fundamental and second harmonic tones coexist and vary gradually over a large range of chemical gate (or electrical gate) input levels, resulting in AM/FM mixed modulation. This way the amplitude on both frequencies constitute a 2D output that may provide redundant information to improve the overall reliability and tolerance to environmental noise and interference.

Calibration of charge neutrality point (V_{cnp}) is another important issue for practical graphene devices, especially in sensor applications. Previously reported methods include annealing of the device in high vacuum, heating in high temperature, or applying special gas/wet treatment after adsorption of substances on graphene [136], [138], [159], [160], but very precise calibration based on those methods is hardly possible yet. In nanomaterial sensor networks, it is unlikely to frequently replace the distributed sensors or heat them onsite after deployment. Therefore, it is preferable to have low-cost approaches that precisely calibrate the V_{cnp} of a graphene device.

Here we demonstrate the chemically-gated mixed modulation concept through an air exposure-ethanol treatment modulation cycle on a graphene transistor. Based on this concept, sensing and modulation may be performed on the same device, requiring no additional module because its high frequency output is compatible with communication media. In addition, by introducing gate voltage pulse sequence enabled electrochemical approach to control charge transfer and capacitive gating effects on graphene, precise calibration of V_{cnp} is achievable under air exposure or wet treatment, eliminating the need of costly temperature or vacuum control equipment. The chemically-gated mixed modulation, along with the precise electrochemical calibration on graphene, has promising potentials in ubiquitous healthcare, automobile, security, food preservation and other related industries.

As shown in an illustrative Figure 5.1(a), the carrier signal is a single-tone sinusoidal wave applied at the back-gate of a graphene transistor. The drain current output waveform under certain drain bias is modulated by chemical gating, consisting of modulation output components at both fundamental and harmonic frequencies. Adsorption to a first substance (e.g. oxidizer type gas molecules) gradually decreases the amplitude of both tones at the output but the harmonic tone will first get fully suppressed.

Meanwhile adsorption to a second substance (e.g. electron-donor type chemical) may reverse the modulation output to original condition. These two phases form a complete chemical modulation cycle, in which either phase could be utilized for sensing and the other for sensor reset, depending on the application. For instance, in oxidizer material sensing, some electron donor material may reset the sensor; while in electron donor material sensing, some oxidizer material may in turn take the role as a reset agent. As the modulation output is high frequency signal, it is more compatible with communication system comparing to DC signal, thus requiring less or no additional signal converting modules. From a system point of view, the unique chemically-gated modulation may simplify the hierarchical structure of nanosensor network system, as summarized and depicted in Figure 5.2.

The chemically-gated modulation mechanism can be explained by referring to the GFET gate input-drain output characteristic curve shift as shown in Figure 5.1(b). When a single tone input at frequency f is applied without DC bias at the gate, the modulation output will show variance as the V_{cnp} gets shifted by chemical gating: if V_{cnp} is around zero, the drain output will have vanished component at f and strong component at $2f$ (grey curve). If V_{cnp} is shifted higher to reach a critical point, the component at f will be significantly amplified and the $2f$ tone will start decreasing (blue curve). If V_{cnp} leaves the above mentioned critical point, the output starts to monotonically decrease, showing drops at both f and $2f$. As V_{cnp} shifts even higher, the $2f$ tone will be completely suppressed, leaving the f tone alone and keeping decreasing (red curve).

A theoretical analysis of the mixed modulation output curves depending on V_{cnp} is shown in Figure 5.1(c) using a compact GFET model. The GFET mixed modulation is evaluated using a physics based drift-diffusive transport model [161],[162] which includes effects such as field-dependent quantum capacitance, fixed velocity saturation, and fixed contact resistance [163]. The model has been validated to predict the behaviors of RFCVD back-gate graphene FETs[164] used in our experimental demonstration. For the purpose of graphene chemically-gated modulation analysis, the model is adjusted to represent I_{ds}-V_{cnp} dependence instead of I_{ds}-V_{gs} dependence. The drain current under and chemical gating induced charge neutrality point shift ΔV_{cnp} can be expressed as [162]:

$$\begin{aligned}
I_{ds} = q\frac{W}{L}\mu_{eff}\Bigg(& n_i V_{ds} \\
& + \Bigg(\frac{(\alpha+1)^2 (k_B T \ln 4)^2}{4\pi\hbar^2 v_f^2 (\alpha \ln 2 + 1)}\Bigg(-2V_{ds} + (V_{dg} \\
& + \Delta V_{cnp})\sqrt{1+\delta^2 (V_{dg}+\Delta V_{cnp})^2} + (V_{gs}-\Delta V_{cnp})\sqrt{1+\delta^2 (V_{gs}-\Delta V_{cnp})^2} \\
& + \frac{\sinh^{-1}\delta(V_{dg}+\Delta V_{cnp}) + \sinh^{-1}\delta(V_{gs}-\Delta V_{cnp})}{\delta}\Bigg)\Bigg)\Bigg)
\end{aligned}$$

Where $\mu_{eff} = \frac{\mu}{\sqrt{\left(1+\left(\frac{\mu V_{ds}}{L V_{sat}}\right)^2\right)}}$, $\alpha = \frac{C_{ox}}{C_{qi}}$ and $\delta = \frac{2\alpha\sqrt{\alpha \ln 2 + 1}}{(\alpha+1)^2}\frac{q}{k_B T \ln 4}$

Our model assumes electro-hole symmetry and also the contact resistance is equally distributed at the drain and source contact. The electrical gate bias V_{gs} is usually fixed or set to zero for chemically gated transistor simulation. Model parameters such as impurity concentration, saturation velocity as well as contact resistance are properly chosen to predict the modulation behavior of a RFCVD back-gate long channel graphene FET [164].

There are two points with best linearity corresponding to the peaks on the fundamental tone curve (blue line) and dips on the harmonic tone curve (red line) with V_{cnp} around ±1.4 V in Figure 5.1(c). Such nonlinearity variation is explained through an illustration of Figure 5.3(a). For graphene, V_{cnp} will be shifting higher (or lower) when continuously exposed to p-type (or n-type) doping material, so there is an operating region that both components are monotonic functions of V_{cnp} as highlighted in Figure 5.1(c).

Other than chemical gating induced V_{cnp} shift, the carrier mobility variation also affects the GFET output. In fact, even though most substances exposed to graphene affect its V_{cnp}, there are also materials with major impact on graphene carrier mobility [165]. Figure 5.3(b) shows the calculated two tone output through 2D vector mapping, which clearly separates the V_{cnp} shifting traces under different mobility values. The result indicates that the 2D output is able to retrieve the information of corresponding V_{cnp} even with variation of other parameters such as carrier mobility, which is a significantly enhanced robustness of sensing over conventional 1D output.

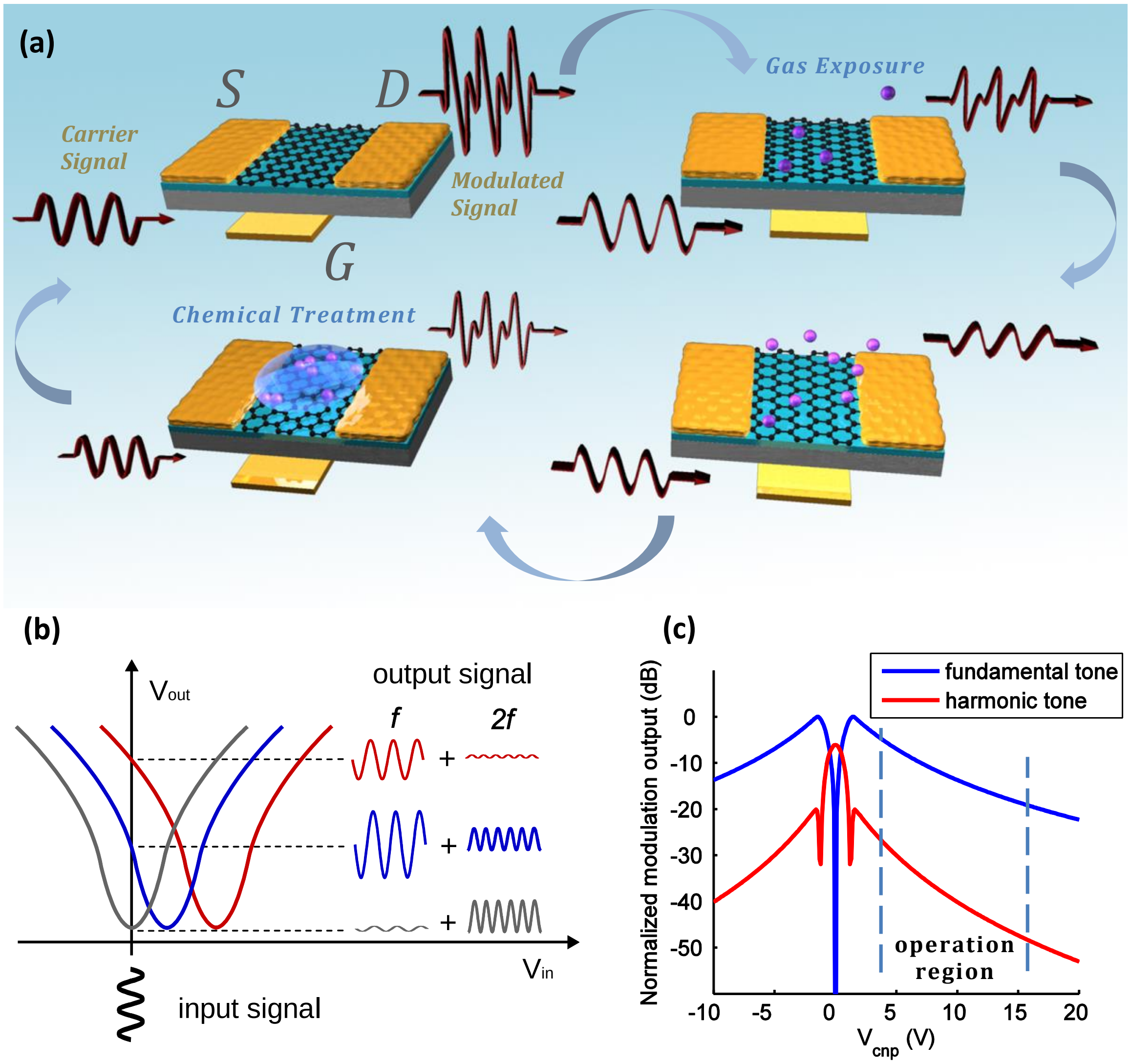

(Figure 5.1 continued next page)

Figure 5.1: Principle of chemically-gated graphene mixed modulation. (a) Conceptual illustration of chemically-gated modulation on a single graphene device, in which the input high frequency carrier signal is applied at the back gate without any gate DC bias, and the modulated output at drain varies during the gas exposure-chemical wet treatment modulation loop cycle. (b) Mechanism of GFET AM/FM mixed modulation; grey: if V_{cnp} is at zero, the output only consists of strong harmonic tone; blue: when V_{cnp} shifts away from 0, large fundamental tone exists and harmonic tone decreases; red: when V_{cnp} shifts higher, both the fundamental tone and harmonic tone decrease, but with the harmonic tone decreasing faster; (c) Physics based modelling result (assuming electro-hole symmetry) of two-dimensional modulation output (in term of normalized output voltage) depending on V_{cnp} shift; a region is outlined where both fundamental and harmonic tones monotonically decrease, which can be used as the operation region for chemical modulation demonstration.

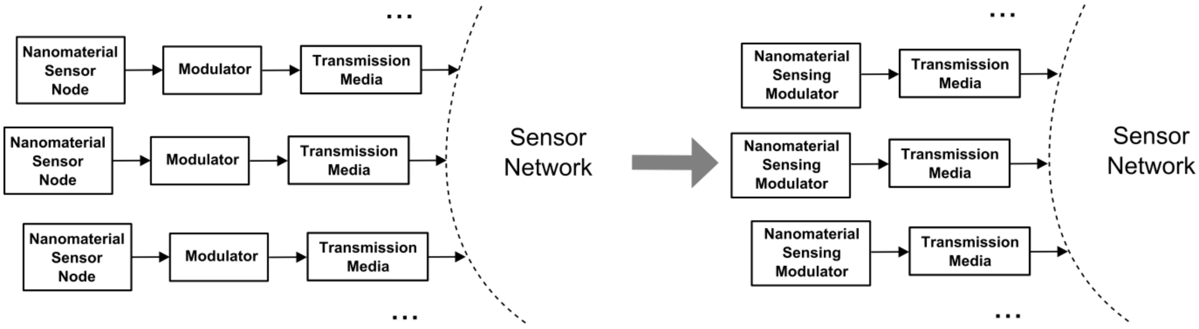

Figure 5.2: Potential improvement of nanosensor networks by utilizing nanomaterial sensing-modulation combined blocks as the nodes.

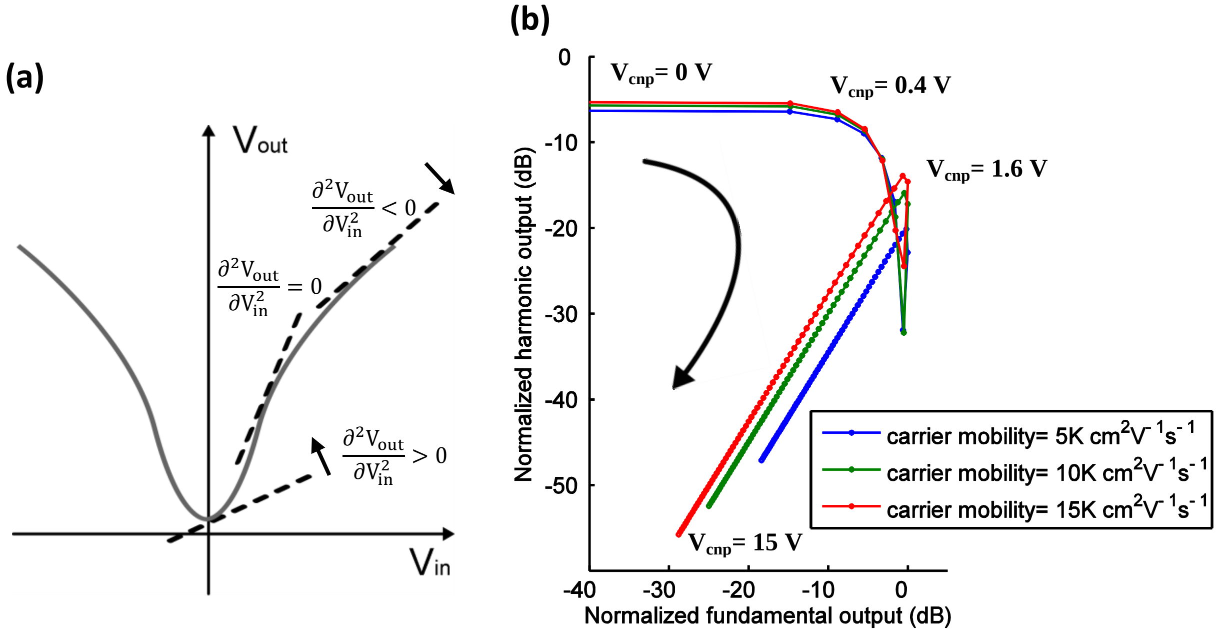

Figure 5.3: (a) Variation of tangent line angle along the GFET DC characteristic curve. The second order derivative is positive around zero where ambipolar field effect induced nonlinearity dominates, and becomes negative under large gate input where the contact resistance induced nonlinearity dominates. In transition there is an absolute linear point (around ±1.4 V according to simulation in Figure 5.1(c)) with zero second order derivative. (b) Simulated two-dimensional output mapping of graphene chemically-gated modulation for V_{cnp} shift traces under different carrier mobility values. The output is normalized so that the maximum fundamental tone on each curve is set at 0dB. The curved arrow shows the general output movement direction with V_{cnp} increasing. From V_{cnp} = 0 V to V_{cnp} = 0.4 V, the output position on the map moves right; from V_{cnp} = 0.6 V to V_{cnp} = 1.4 V the output moves downward; starting from V_{cnp} = 1.6 V the output moves toward lower left.

5.3 EXPERIMENTAL REALIZATION OF AIR EXPOSURE-ETHANOL TREATMENT MIXED MODULATION CYCLE

Chemical gating effect typically results from oxidizer (e.g. NO_2, O_2, ambient air) or electron donor (e.g. NH_3, NH_2) induced charge transfer between graphene and the adsorbed substances [141]–[143]. For instance, under ambient air the I_{ds}-V_{gs} curve of a graphene FET shifts rightward (p-type shift), as verified through a DC characteristic measurement shown in Figure 5.8(a).

The device under test is a photoresist-free shadow mask direct patterned large area back-gate single layer graphene FET (Figure 5.4), which is suitable for chemical gating test. In our experiment, we use large area GFETs fabricated by shadow mask without lithography step to preserve the pristine surface of graphene, because other than the H_2O/O_2 redox system, residues such as photoresist may also contribute to the formation of charge traps. This synthesized graphene was first transferred with poly methyl methacrylate (PMMA) as a support onto a SiO_2/Si substrate with 285nm thermal oxide. Raman spectroscopy with 442nm blue laser has been used to confirm the good quality of graphene after transfer (Figure 5.4(b)), showing G peak at 1582cm^{-1} and a symmetric 2D band at 2695cm^{-1} (bandwidth~32). Back-gated field effect transistors with electron-beam-evaporated Ti+Au metal contacts defined via a shadow mask were made to measure electrical properties. The metal contacts are 200 by 200 μm, with a channel length option of 25, 50, 100, and 200 μm, as shown in Figure 5.4(a). More details about the fabrication process can be found in our previous work [166]–[168].

In the chemically-gated modulation demonstration, the back-gate and drain contacts of a GFET with 100 μm channel length vacuum fixed on a probe station are connected to bias-Tees in order to combine and separate RF and DC signal, respectively. The input RF signal is generated from a function generator and the DC drain bias is from a voltage source; the output at the drain are measured by an Agilent DSO-X 3034A digital oscilloscope with spectrum analyzing function by fast Fourier transfer. In the V_{cnp} calibration demonstration, the DC I_{ds}-V_{gs} curves of the GFET with 100 μm channel length are recorded with an HP4145B semiconductor parameter analyzer under ambient conditions, with the drain to source bias at 100 mV. 200 proof ACS/USP ethyl alcohol (100% ethanol) droplets are directly applied to the device on the probe station under the ambient environment at room temperature as the wet treatment agent during the experiment.

The electron transfer rate from the graphene layer to the H_2O/O_2 redox system from ambient air is proportional to the overlap between the occupied states of graphene and the unoccupied state of the H_2O/O_2 solution [169]–[171] so that the rate of p-type shift of V_{cnp} is showing some exponential decay until the graphene density of states (DOS) and the H_2O/O_2 redox couple DOS reaches an equilibrium. In our test V_{cnp} has a shift from 3 V to 12 V after 10 minutes of air exposure.

Restoring the intrinsic electrical characteristic can be done by high vacuum annealing or high temperature heating which desorbs the substances on graphene [136], [159]. Wet chemical treatment is also able to reverse intrinsic graphene, though most studies are based on photoresist contaminated graphene FETs and the involved recovery chemicals are hazardous (BOE, HF, $CHCl_3$) [160], [172] . Here ethanol solution is used as a cost effective and relatively safe chemical to recover V_{cnp} of a photoresist-free graphene device. During the wet treatment, a temporarily p-doped graphene FET is treated by an ethanol droplet for 20 seconds, the droplet is then dried by nitrogen gun and the measured instant V_{cnp} is reduced from 16 V to 3V, as shown in Figure 5.9(a). The recovery mechanism is that the ethanol solution eliminates the H_2O/O_2 redox system near graphene, and hence moves the Fermi level of graphene to the original level before air exposure, as depicted in Figure 5.5. This is similar to BOE treatment [173];but unlike the chemical reaction between HF and H_2O [173], here the H_2O/O_2 redox system gets removed because it is readily soluble in ethanol, making it a chemical reaction free and environmental friendly process suitable for practical applications.

The chemically-gated mixed modulation is demonstrated through an air exposure-ethanol treatment modulation cycle, without loss of generality for other gases and wet chemicals which may also establish similar modulation functions on a GFET. Figure 5.6 shows the spectra of the modulated output under a 3 V peak-to-peak 25 kHz single tone input at the back-gate with 100 mV DC drain bias. Assuming negligible gate leakage, the power consumption of the modulator is coming from the drain bias. For an estimated average drain current of 50 μA, the input power is only about 5 mW. In a modulation cycle, the V_{cnp} is initially around 3 V, and the output vector consisting of fundamental tone at 25 kHz and second harmonic tone at 50 kHz is <50dB, 16dB> signal-to-noise ratio (SNR). Figure 5.6(a)-(b)-(c) is the air exposure modulation phase, during which the output vector drops to <43dB, 9.5dB> SNR after 2 minutes (Figure 5.6(b)), and to

<41dB, 0dB> SNR after another 2 minutes (Figure 5.6(c)). Figure 5.6(c)-(d)-(a) is the ethanol treatment phase, during which the output vector is reset back to <50dB, 16dB> SNR after the treatment. Figure 5.6 (d) is the output spectrum of an intermediate state during wet treatment; after ethanol has been dried the output is reset to its original. The spectra before and after a complete modulation cycle are compared in Figure 5.7. The 2D output provides redundant information that may benefit post signal processing in sensing systems, which potentially improves the robustness and enables absolute accuracy in sensing.

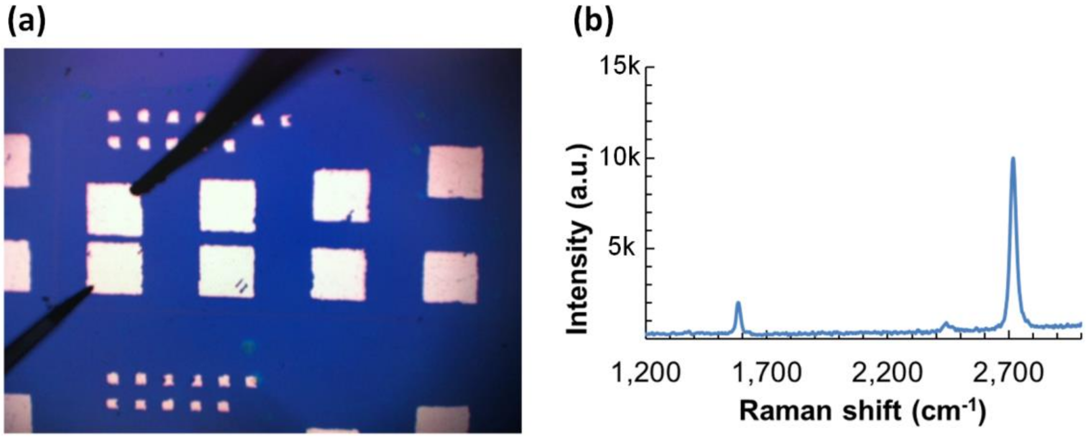

Figure 5.4: Fabricated graphene device. (a) Microscope picture for the graphene devices with 25, 50, 100, and 200μm channel length, 100μm device is used for this demonstration. (b) Raman spectrum of graphene after transfer onto SiO_2/Si device substrate.

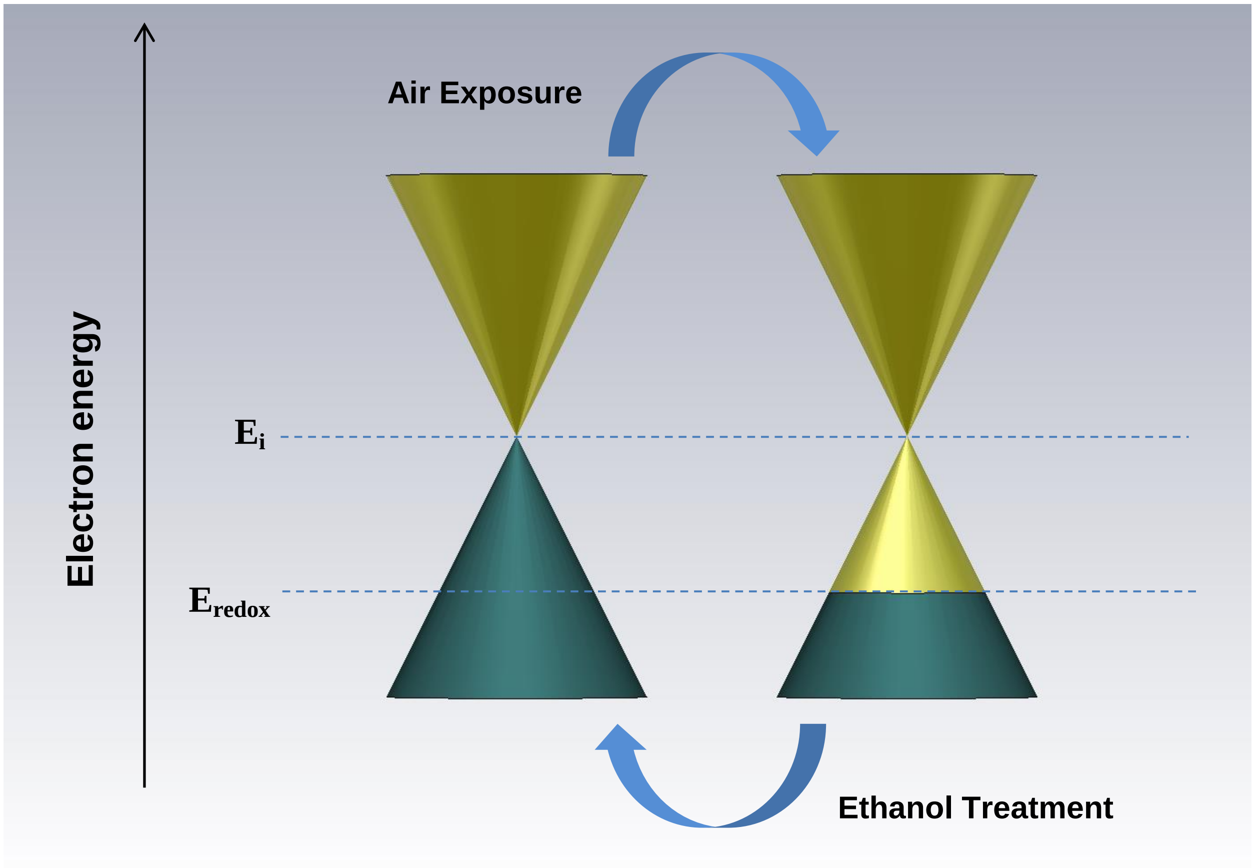

Figure 5.5: The change of graphene Fermi level by redox system induced charge transfer and ethanol treatment based wet recovery.

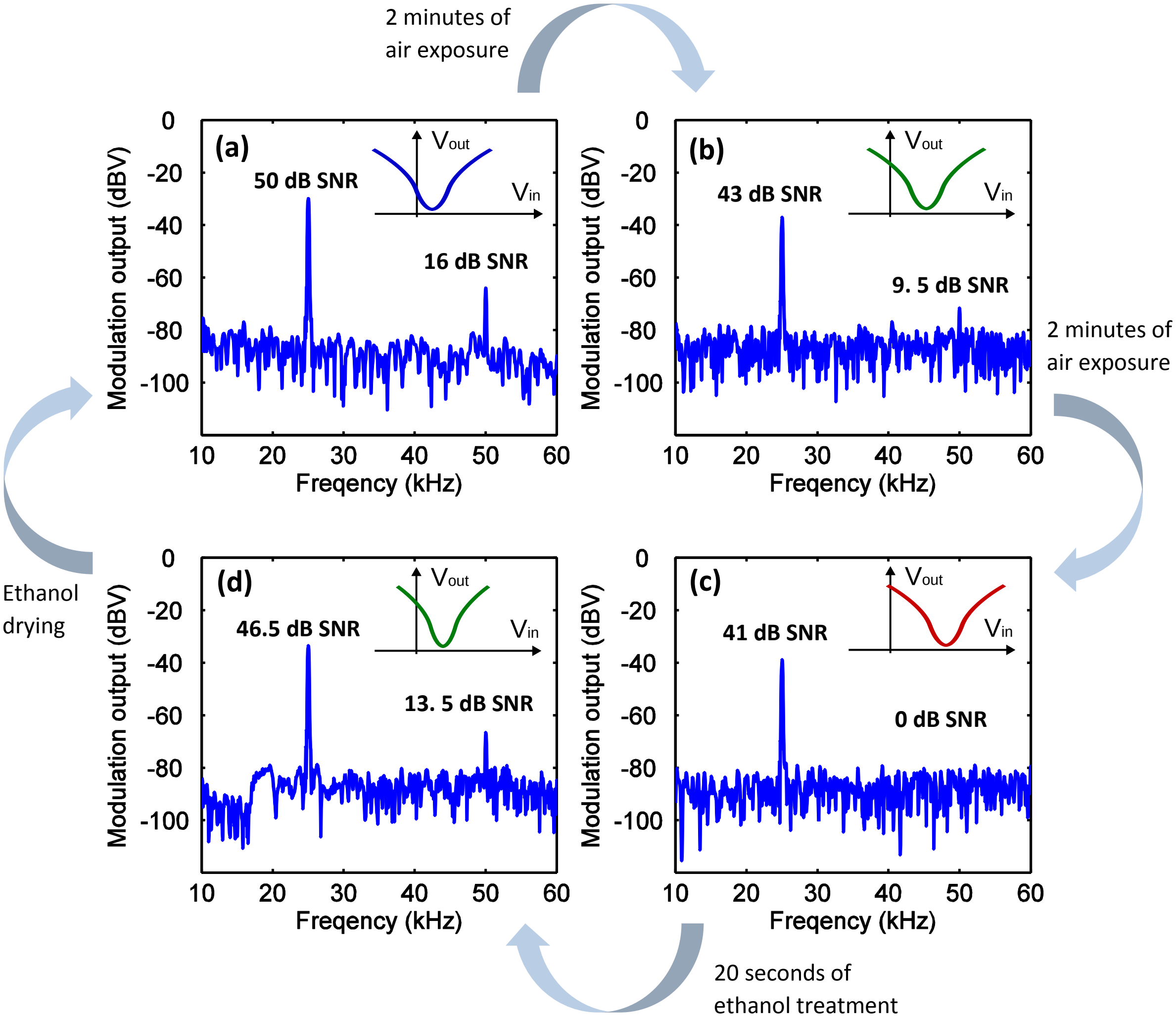

(Figure 5.6 continued next page)

Figure 5.6: Realization of air exposure-wet treatment AM/FM mixed modulation cycle on a chemically-gated GFET with a single tone back-gate input carrier signal at 25kHz. (a) Initially when V_{cnp} is around 3 V, the output vector is <50dB, 16dB> SNR, with the noise level at -80dBV. (b) V_{cnp} shifts to higher voltage after 2 minutes exposure and the output drops to <43dB, 9.5dB> SNR. (c) Further air exposure for another 2 minutes results in an even higher V_{cnp} and the output is <43dB, 0dB> SNR. (d) The operation condition can be reversed by the ethanol based wet treatment. At the moment an ethanol droplet is applied, the intermediate output is <46dB, 13.5dB> SNR. After 20 second treatment, the ethanol is dried and the device is reset to the original state <50dB, 16dB> (comparison before and after the cycle is shown in Figure 5.7).

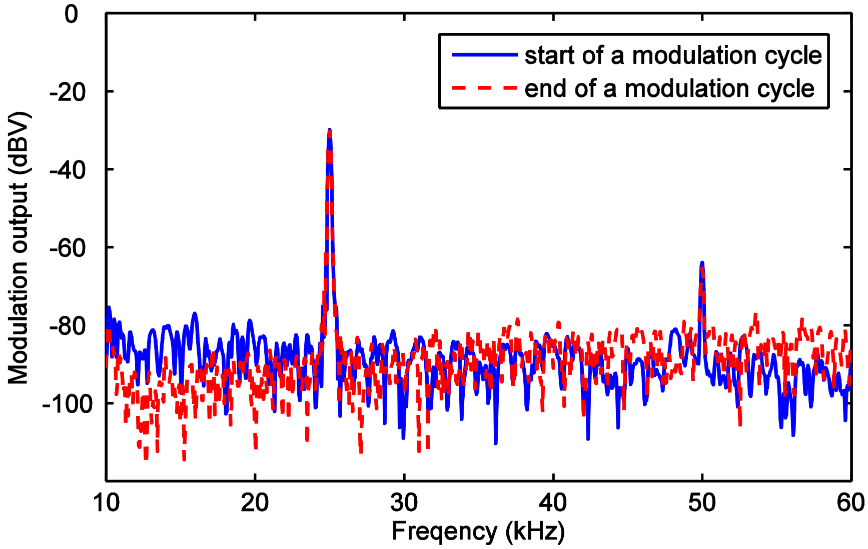

Figure 5.7: Comparison of chemically-gated modulation output spectrum of initial state before air exposure and after the ethanol recovery. Both fundamental and harmonic tones are matched, showing good reusability.

5.4 PULSE SEQUENCE ASSISTED ELECTROCHEMICAL CALIBRATION OF V_{CNP}

V_{cnp} of a graphene device can be calibrated during gas exposure or wet treatment phase with the assistance of voltage pulse sequence applied at the gate. It has been reported that when a forward voltage sweep is applied on a GFET, for example, from -80 V to 80 V, V_{cnp} will usually shift higher, and the shift is noticeable from the backward sweep of I_{ds}-V_{gs} curve from 80 V to -80 V [169]. Such hysteresis in graphene conductance is caused by variation of charge transfer rate from the graphene to charge traps [169], [170]; but under certain conditions, capacitive gating effect [169] could dominate over charge transfer.

Under ambient air exposure, the charge traps are the H_2O/O_2 redox systems near the graphene layer. Here we dynamically control the hysteresis behavior by repeatedly applying unidirectional positive (or negative) voltage pulse sequence, and it results in a faster (or slower) V_{cnp} movement during air exposure. Figure 5.8 shows the comparison of V_{cnp} shifts under the same air exposure condition and time duration but with voltage pulse sequence of different polarities applied at back-gate. Figure 5.8(a) shows I_{ds}-V_{gs} curve shift during air exposure with no gate pulse. Figure 5.8(b) shows I_{ds}-V_{gs} curve shift with positive gate voltage pulse sequence with each pulse sweeping from 0 V to 30 V (each cycle contains 1.5 sec positive pulse and 4.5 sec idle, i.e. 10 pulses per minute). Figure 5.8(c) shows the I_{ds}-V_{gs} curve shift with negative gate voltage pulse sequence with each pulse sweeping from -20 V to 0 V (each cycle contains 1 sec negative pulse and 0 sec idle, i.e. 60 pulses per minute). When the gate-to-source voltage pulse is positive, and the drain-to-source DC bias is negligibly small, the electrons temporarily pumped to graphene channel as well as the inward electric field near the graphene layer will accelerate electron charge transfer from graphene to the H_2O/O_2 charge traps. When the pulse stops, the accumulatively over transferred electrons from to graphene to the charge traps cause a stronger p-type shift of V_{cnp}, i.e. sensitized chemical gating. On the other hand, if the gate to source voltage is negative, there will be holes temporarily pumped to graphene channel by a pulse and the electric field direction at the graphene surface will be outward, resulting in weaker p-type shift during air exposure, hence tuning the graphene device toward a desensitized chemical gating modulator.

The wet chemical treatment phase in graphene chemical modulation cycle can also be calibrated by gate voltage pulse sequence. Ethanol may recover a p-doped GFET to nearly intrinsic state, while applying positive back gate voltage pulse sequence during ethanol treatment may push the V_{cnp} to even below the intrinsic value. Figure 5.9(a) to 4(c) compare V_{cnp} movement under the same ethanol wet treatment condition with no gate pulse, positive pulse and negative pulse sequence, respectively. In contrast with the V_{cnp} recovered at 3V in Figure 5.9(a), V_{cnp} in Figure 5.9(b) moved to -8V after ethanol drying when a 0-30V voltage pulse sequence was repeatedly applied during the 20 sec ethanol treatment (each cycle contains 1.5 sec pulse and 1.5 sec idle, i.e. there are totally 7 pulses during the treatment). We postulate that for ethanol treatment it is a capacitive gating dominant phenomenon: As ethanol is a polar solvent, when a positive pulse is applied, the inward electric field enforces dipole molecules in the ethanol droplet with orientations toward graphene layer, which significantly increases the electron carrier density on the graphene and results in stronger n-doping effect after the positive pulse. As more positive pulses are applied, the dipole moment is getting stronger accumulatively. On the other hand, experiment shows that applying negative back-gate voltage pulse sequence during ethanol treatment will remarkably reverse the V_{cnp} shift from n-type to strong p-type, with an achieved V_{cnp} higher than 50V as shown in Figure 5.9(c). This can be in turn explained by capacitive gating: under outward electric field, the dipole orientations are backward graphene layer, repelling free electrons to move away from graphene layer. A very high density of hole carriers is thus induced on the graphene layer as a result of the negative pulse, yielding a strong p-type doping process.

Although the exact mechanism of electrochemical control on chemical gating needs further investigations, the full calibration ability has been experimentally demonstrated and is summarized in Figure 5.10(a) as a practical guide for V_{cnp} tuning. Any desired V_{cnp} value, including a precise zero, can be achieved through the voltage pulse sequence-assisted electrochemical calibration, as shown in Figure 5.10(b). Other than ambient air and ethanol solution, different materials can also be applied to graphene chemical gating which may result in different patterns of modulation cycles. For example, water is compared with ethanol in recovering V_{cnp} of graphene as shown in the experimental results of Figure 5.11. In addition, exposure to some third material could affect the chemical gating cycle. For example, two different protein solutions, milk and ESAT-6 [174] (a biomarker of mycobacterium tuberculosis) are tested on and compared in Figure 5.12. As a result, this work illustrated GFET based versatile device that integrated chemically gated sensing and mix modulation functions into one single unit with precise calibration and reversibility.

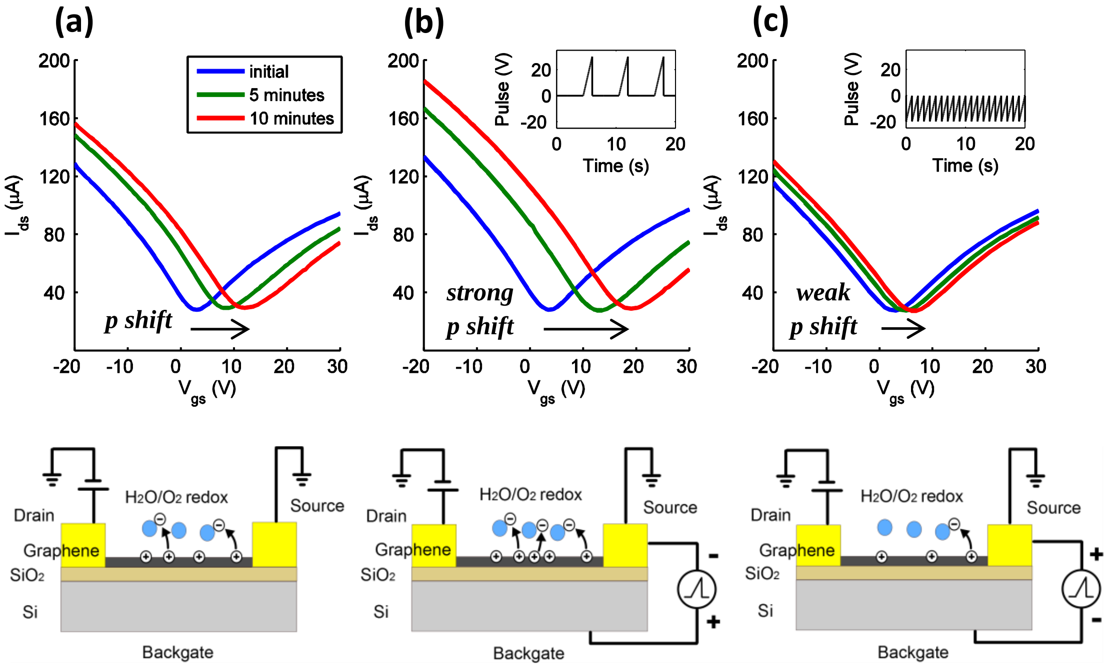

(Figure 5.8 continued next page)

Figure 5.8: Demonstration of pulse sequence induced electrochemical calibration of GFET chemical gating during 10 minute air exposure. (a) The H_2O/O_2 redox system from the air serve as charge traps that attracts electrons transferred from graphene, resulting in p-type shift of V_{cnp}. (b) With repeating positive gate voltage pulse sequence applied, electrons are temporarily pumped to graphene channel from the source metal contact and the electric filed is toward graphene layer, accelerating the electron charge transfer from graphene to the H_2O/O_2 charge traps during a positive voltage pulse. Because a large population of electrons have been transferred to charge traps, more holes are accumulated on graphene layer when the pulse stops, and it results in a stronger p-type shift of V_{cnp} than without the positive voltage pulse. (c) Similarly, with unidirectional negative gate voltage pulse sequence applied, holes are temporarily pumped to the graphene channel and the electric filed is outward near graphene layer, decelerating the charge transfer from graphene to the H_2O/O_2 charge traps and resulting in a weaker p-type shift of V_{cnp}.

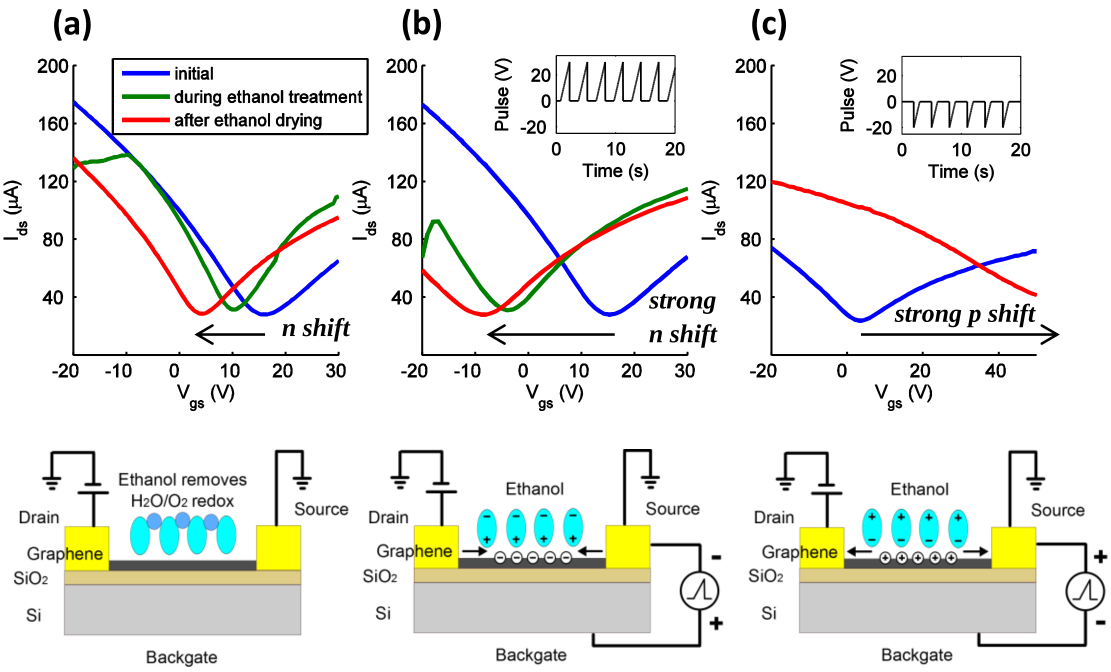

(Figure 5.9 continued next page)

Figure 5.9: Demonstration of pulse sequence-induced electrochemical calibration of GFET chemical gating during 20 second ethanol wet treatment. (a) The H_2O/O_2 residues on graphene are readily soluble in ethanol, and as the charge traps get removed after the ethanol is dried, the I_{ds}-V_{gs} curve is showing n-type shift and recovered from a p-doped GFET. (b) With repeating positive gate voltage pulse sequence applied, the dipole moment of ethanol molecules with its direction toward graphene is gradually enhanced, and the capacitive gating effect draws electrons from metal contacts to move and accumulate on graphene. Combining the effect in (a), overall the V_{cnp} is showing stronger n type shift after ethanol wet recovery with positive voltage pulse. (c) With unidirectional negative gate voltage pulse sequence applied, the dipole moment of ethanol molecules gets reversed, pushing electrons away from grapheme layer. Now the capacitive gating effect leaves a large number of holes accumulated on graphene and results in very strong p-type shift of V_{cnp}.

(a)

	Positive pulse	**No pulse**	**Negative pulse**
Air exposure	P^+	**P**	P^-
Ethanol	N^+	**N**	P^{++}

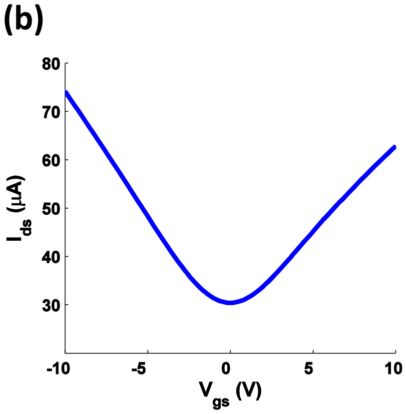

(Figure 5.10 continued next page)

Figure 5.10: Precise tuning of V_{cnp} of graphene FET. (a) Summary of the electrochemical calibration under air exposure and ethanol treatment. Letter P and N denote V_{cnp} shift direction, and the sign denote the relative extent of the shift, e.g. P^- is weak p-type shift and N^+ is strong n-type shift. (b) Realization of a precise zero V_{cnp} utilizing gate pulse sequence electrochemical calibration.

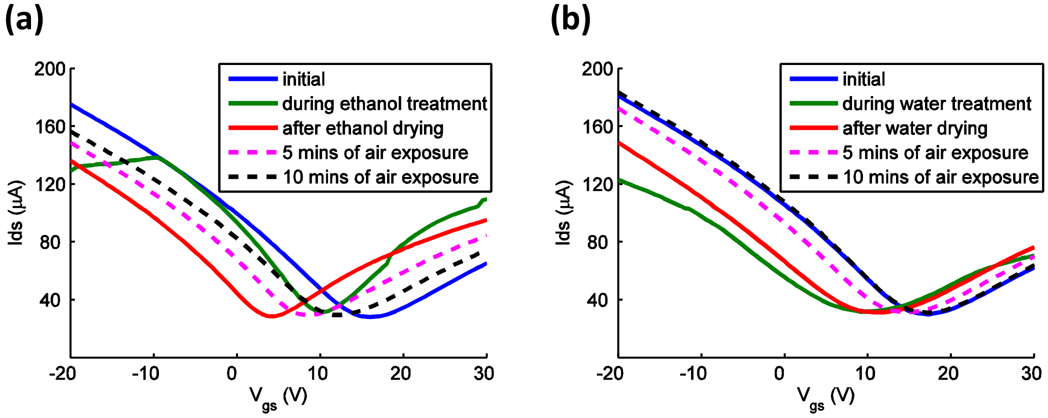

Figure 5.11: Comparison of (a) ethanol and (b) water droplets as wet treatment agent in a chemical gating cycle under no gate pulses. The water treatment (using cleanroom standard DI water) shows weaker n-doping effect compared to ethanol treatment, as its ability to remove H_2O/O_2 redox residues on graphene is weaker compared to ethanol.

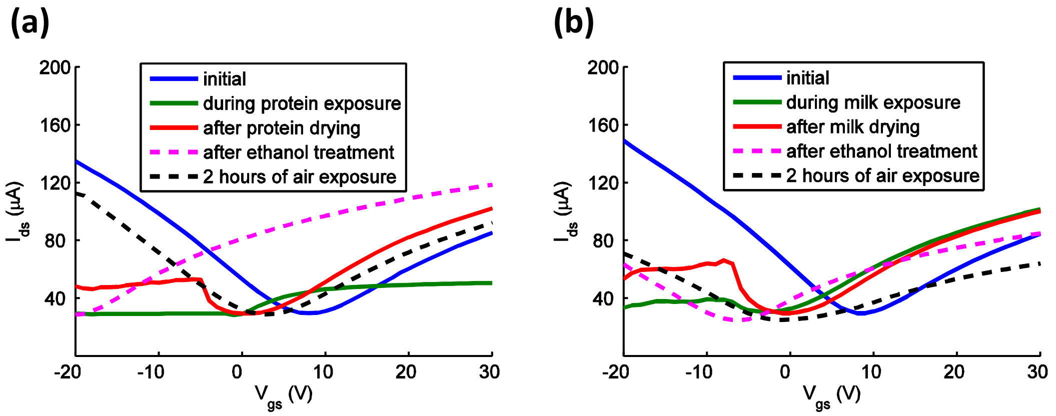

Figure 5.12: The use of (a) ESAT-6 [174] protein solution and (b) milk as a third material to break the reversibility of V_{cnp} in ethanol treatment-air exposure chemical-gating cycle. Initially the ESAT-6 protein solution or milk droplet is applied on the graphene sample, after the droplet gets dried, its solid state residues will stay on the graphene. Subsequent ethanol treatment will help remove the residues, but not completely. During the ethanol treatment, positive gate pulse sequence is applied to provide strong n-type shift of V_{cnp}. The comprehensive polarity of the ESAT-6 protein solution mixed with ethanol in (a) is different from milk liquid mixed with ethanol in (b), so the movement of V_{cnp} is also different (to -20 V for protein and -7 V for milk, respectively). Now as graphene has been covered by residues from the protein solution or milk, exposure to air no longer shows the same p-type shift as in Figure 5.8(a); rather, after 2 hours, V_{cnp} only moves from -20 V to 3V for the ESAT-6 contaminated sample, and from -7 V to 0V for the milk contaminated sample. This result shows its potential for point-of-care diagnosis and food quality monitoring applications.

5.5 PASSIVE GFET MIXER CIRCUITS BASED ALL-CARBON RFID TRANSPONDER SENSORS

As already evaluated in Chapter 4, for ubiquitous wireless sensor networks, passive sensor nodes without any battery or power-harvesting module will be an ultimate solution to minimize the cost and simplify the maintenance. A single device graphene transistor modulator sensor has limitation as it still needs drain DC bias, but it can serve as a building block for passive all graphene sensing/communication circuits specifically designed and optimized for different application scenarios.

Here we show a circuit design of a fully-passive graphene frequency doubler with a moderately high conversion gain, ideally approaching the physical limit of 30 % for conventional diode-based frequency multipliers, using the complete GFET model as the cell in the simulation. This graphene based doubler can be considered as the frequency conversion block in the harmonic transponder described in Chapter 4, but with the nanomaterial frequency doubler itself as a sensing agent instead of the antenna. A passive nonlinear transponder connected to each object is the unit that re-radiates the harmonic of the incoming interrogating signal. The all graphene circuit is based on the self-biased ring-quad passive mixer topology with four GFET as receptors shown in Figure 5.13(a). It can serve as a passive nonlinear sensing transponder whose harmonic output amplitude is modulated by chemical gating effect. Such tag, if connected to antennas (fundamental antenna at input and harmonic antenna at output), is not only tractable in position, but also re-radiating modulated output signals which carry sensing information in terms of harmonic amplitude. The simulated output waveforms under different V_{cnp} conditions are shown in Figure 5.13(b). The output fundamental tone at 900MHz is always blocked if all four graphene receptors are matched, and the conversion gain (here is in terms of voltage gain, to specify power gain matching network at both input and out is needed) of the output harmonic tone at 1.8GHz is dependent on the V_{cnp} shift as shown in Figure 5.13(c). The impact of input signal amplitude on the sensor performance is also included in the Remarkably, the passive graphene circuit as a rectifier can operate even when the input voltage is as low as 0.3V, which is hard for conventional semiconductor rectifiers (e.g. Si diode has a typical turn on voltage at 0.7 V). On the other hand, if the graphene receptors have mismatch, for example, V_{cnp} of receptor 2,3 and 4 are fixed at 0.8V while for receptor 1 it is shifted to 5V, the output will now have strong fundamental tone, as shown in the last curve in Figure 5.13(b). In this example, redundancy from the two dimensional output enables global sensing as well as localized sensing for the mismatch at each receptor. The local sensing curve depending on V_{cnp} of receptor 1 (when the other devices are fixed at V_{cnp} =0.8V) is compared to global sensing curve shown in Figure 5.13(d).

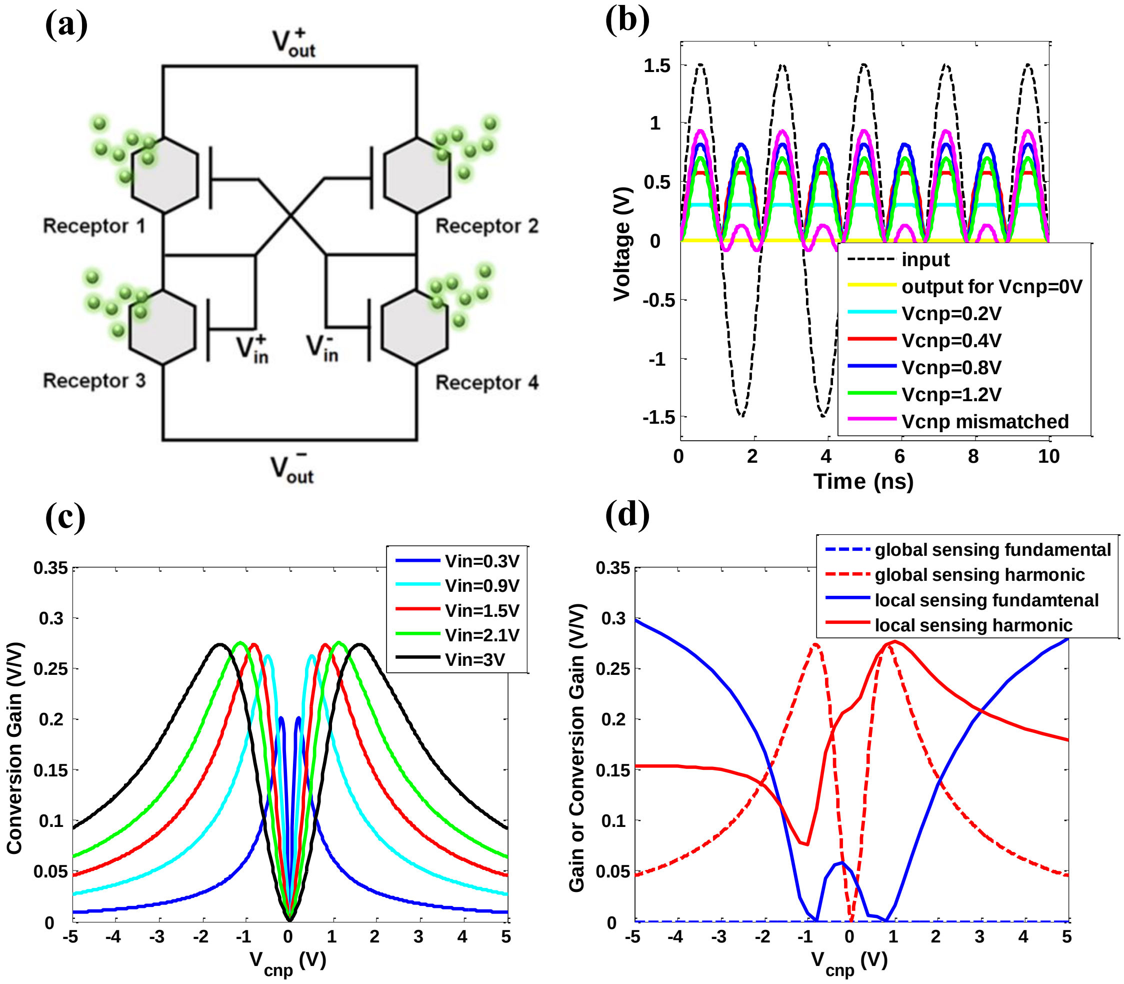

(Figure 5.13 continued next page)

Figure 5.13: Simulation (using Agilent ADS) of a passive multiple receptor all graphene modulator sensing system. (a) Circuit configuration utilizing ring mixer topology. (b). simulated waveforms of the modulated output variation under different V_{cnp} values and mismatched conditions: if all receptors are matched the output is frequency doubled, if receptor 1 is mismatched the output will contain strong fundamental tone. (c) Dependence of the harmonic tone conversion gain (voltage gain) on V_{cnp} shift under different RF input amplitude, assuming matched condition. (d) The two dimensional output can represent both global and local sensing information (input is fixed at 1.5V): dashed lines correspond to global sensing curve when all receptors are matched; solid line correspond to local sensing curve depending on V_{cnp} of receptor 1, assuming all other receptors have a fixed V_{cnp} at 0.8V.

Here we have theoretically validated that the output signal of the graphene based harmonic transponder will sensibly depend on the shift value of V_{cnp}, potentially caused by the electrochemical reactions. To realize a passive nanomaterial harmonic transponder, fabrication is challenging in terms of aligning the four graphene transistors with a two layer routing of the shared gate connection. In addition, matching the antenna impedance to the input and output impedance of the passive graphene frequency doubler will be tricky, as the graphene device size is a few hundred μm, comparing to typical 2 GHz antennas with at least a few centimeters in length. The graphene modulator that has been experimentally demonstrated can also connect with antennas to practically support a harmonic transponder sensor, a power source is required to provide only 0.1V DC bias at the drain. Resolving those issues would lead to a highly efficient and low cost chemical and biological wireless sensing platform, with a wide range of application potentials such as wireless hygiene monitoring and proteomic early diagnosis, as illustrated by Figure 5.14.

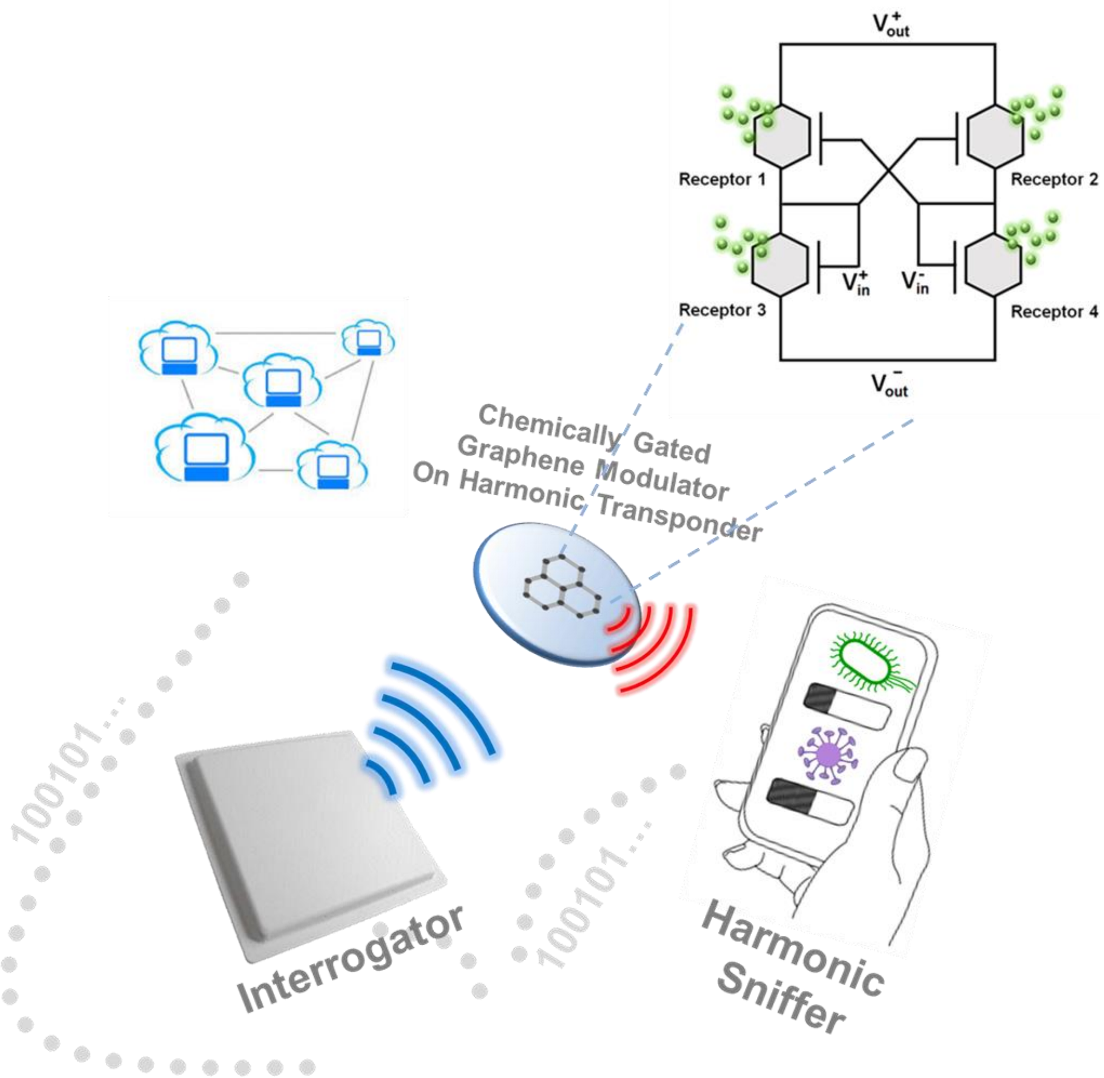

Figure 5.14: Potential usage of passive chemically gated graphene modulator based harmonic transponder in wireless hygiene monitoring and proteomic early diagnosis.

5.6 CHAPTER SUMMARY

In this chapter, the principle of chemically-gated mixed modulation on GFET, along with pulse sequence enabled electrochemical calibration of V_{cnp} is proposed and realized through a demonstration of air exposure-ethanol treatment chemically-gated modulation cycle. This new paradigm may enable development of practical graphene or other nanomaterial based sensor networks with improved reliability, reusability and system integrability. The low maintenance cost and low energy consumption features of the demonstrated graphene chemically-gated modulation based device are compatible with the demand of distributed and ubiquitous sensing applications. Specifically, the air exposure-ethanol treatment chemically-gated modulation may provide a platform for air quality monitoring [175]–[178] or hygiene compliance monitoring [179], [180] in healthcare facilities. Systematic investigation of a large variety of materials will be beneficial and future challenges to turn this concept into practical sensing products involve specificity enhancement of chemically-gated modulation on graphene and other nanomaterial devices. Integration of the graphene chemical gating modulator with antennas will potentially form a nanomaterial harmonic transponder sensor.

Chapter 6: Conclusions and Outlook

6.1 CONCLUSIONS

In this dissertation the author's research work related to several hardware aspects of wireless sensors for healthcare internet of things have been described. First is the development of 3-D electrical small antennae for medical telemetry, especially for implanted wireless health products. A new ESA design of folded ellipsoidal helix antenna has been introduced and fabricated using a selective laser sintering assisted molding process, which is mass procurable at very low cost comparing to conventional 3-D antenna fabrication process. The measurement result of the ellipsoidal helix ESA shows its advantage in turns of tunability, design flexibility and application compatibility for healthcare while maintaining its high bandwidth-to-size performance ratio comparing to other ESA designs.

Secondly, a concept of using 3-D ESA for drug delivery and other healthcare liquid monitoring has been proposed and experimentally verified. On the sensor design side, a few antenna sensor design methodologies including a meta-material inspired 3-D antenna sensor have been realized. On the wireless sensing system side, a zero-powered, HFSS harmonic RFID transponder sensing system has been developed to utilize the antenna sensors. The in-vitro measurement demonstrates its ability of μL resolution passive wireless liquid level sensing/drug delivery monitoring with absolute accuracy. Without the need of battery and additional sensor module, the antenna based harmonic RFID transponder sensing system has potential to support the ubiquitous healthcare monitoring.

Another work in this dissertation is nanomaterial based sensors for healthcare IoTs. Specifically, we have developed a graphene nanomaterial chemically sensitive modulator to simplify the architecture of wireless nanosensor network. Demonstration of graphene chemically-gated modulation along with its convenient V_{cnp} calibration is realized through an example of air exposure-ethanol treatment modulation cycle on a photolithography-free large area graphene field effect transistor. This special single transistor sensing/modulation dual function module, combining with the harmonic RFID tag, is able to support passive or semi-passive pervasive nanomaterial sensors for many healthcare and environmental applications such as point-of-care proteomic test, hygiene compliance assurance and air/gas detection.

6.2 OUTLOOK

Healthcare internet of things is a highly interdisciplinary research area. The work included in this dissertation focuses on providing some hardware foundation for building up healthcare application specific wireless sensor networks and cyber physical systems. Unlike most consumer products, medical and healthcare IoTs may require more application specific designs on antennas, sensors, circuits and communication systems. This dissertation work shows the potentials of some concepts and prototypes that can be further developed and investigated to better serve a large variety of applications in healthcare. The researches here can be also incorporated with innovations in other fields such as pervasive computing, big data, artificial intelligence, neuromorphic engineering etc., in order to provide better ubiquitous healthcare IoT platforms for the coming decades when global aging issue is going to be tremendous.

Bibliography

[1] T. S. Rappaport, *Wireless Communications: Principles and Practice*, vol. 207. 2002, pp. 1–707.

[2] R. R. Schaller, “Moore’s law: past, present and future,” *IEEE Spectr.*, vol. 34, 1997.

[3] P. F. Eder, “A History of the Internet and the Digital Future.,” *World Futur. Rev.*, vol. 4, pp. 105–108, 2012.

[4] L. Kleinrock, “History of the Internet and its flexible future,” *IEEE Wireless Communications*, vol. 15. pp. 8–18, 2008.

[5] N. Gershenfeld, R. Krikorian, and D. Cohen, “The Internet of things.,” *Sci. Am.*, vol. 291, pp. 76–81, 2004.

[6] K. Ashton, “That ‘Internet of Things’ Thing,” *RFID J.*, 2009.

[7] W. He, G. Yan, and L. Da Xu, “Developing vehicular data cloud services in the IoT environment,” *IEEE Trans. Ind. Informatics*, vol. 10, pp. 1587–1595, 2014.

[8] J. Gubbi, R. Buyya, S. Marusic, and M. Palaniswami, “Internet of Things (IoT): A vision, architectural elements, and future directions,” *Futur. Gener. Comput. Syst.*, vol. 29, pp. 1645–1660, 2013.

[9] K. Gill, S. H. Yang, F. Yao, and X. Lu, “A ZigBee-based home automation system,” *IEEE Trans. Consum. Electron.*, vol. 55, pp. 422–430, 2009.

[10] C. Gomez and J. Paradells, “Wireless home automation networks: A survey of architectures and technologies,” *IEEE Commun. Mag.*, vol. 48, pp. 92–101, 2010.

[11] Z. J. Z. Ji and Q. A. Q. Anwen, “The application of internet of things(IOT) in emergency management system in China,” *Technol. Homel. Secur. (HST), 2010 IEEE Int. Conf.*, 2010.

[12] C. Doukas and I. Maglogiannis, “Bringing IoT and cloud computing towards pervasive healthcare,” in *Proceedings - 6th International Conference on Innovative Mobile and Internet Services in Ubiquitous Computing, IMIS 2012*, 2012, pp. 922–926.

[13] R. S. H. Istepanian, S. Hu, N. Y. Philip, and A. Sungoor, “The potential of Internet of m-health Things m-IoT for non-invasive glucose level sensing,” in *Proceedings of the Annual International Conference of the IEEE Engineering in Medicine and Biology Society, EMBS*, 2011, pp. 5264–5266.

[14] V. M. Rohokale, N. R. Prasad, and R. Prasad, “A cooperative Internet of Things (IoT) for rural healthcare monitoring and control,” in *2011 2nd International Conference on Wireless Communication, Vehicular Technology, Information Theory and Aerospace and Electronic Systems Technology, Wireless VITAE 2011*, 2011.

[15] A. J. Jara, A. F. Alcolea, M. A. Zamora, A. F. Gómez Skarmeta, and M. Alsaedy, “Drugs interaction checker based on IoT,” in *2010 Internet of Things, IoT 2010*, 2010.

[16] A. Ghose, C. Bhaumik, D. Das, and A. K. Agrawal, “Mobile healthcare infrastructure for home and small clinic,” *Proc. 2nd ACM Int. Work. Pervasive Wirel. Healthc. - MobileHealth ’12*, vol. 2, p. 15, 2012.

[17] R. Valencia, “Keynote Speech by Qualcomm Life CEO,” in *IEEE Healthcare Innovation Conferenceconference, November 2012*, 2012.

[18] “World Aging Population.” [Online]. Available: http://www.un.org/esa/population/publications/ worldageing19502050/.

[19] H. Services, “Global Health and Aging,” *NIH Publ. no 117737*, vol. 1, pp. 273–277, 2011.

[20] K. Kinsella and D. R. Phillips, “Global Aging : The Challenge of Success,” *Popul. Bull.*, vol. 60, pp. 1–44, 2005.

[21] “Thomas P.M. Barnett’s Globlogization - Blog - Chart of the day: From population ‘pyramid’ to ‘kite.’” [Online]. Available: http://thomaspmbarnett.com/globlogization/2010/11/27/chart-of-the-day-from-population-pyramid-to-kite.html.

[22] “World population: The world in 2100 | The Economist.” [Online]. Available: http://www.economist.com/blogs/dailychart/2011/05/world_population.

[23] “NRC FLIS Interest Group - IG 18 - National Reference Centres for Forward Looking Information and Scenarios.” [Online]. Available:

http://forum.eionet.europa.eu/nrc-flis/library/consultation-countries/gmt-update-2013/gmt-1/global-megatrend-1/trends-population-size-and-structure.

[24] “India: Shifting Landscape | KKR.” [Online]. Available: http://www.kkr.com/global-perspectives/publications/india-shifting-landscape.

[25] “List of countries by median age - Wikipedia.” [Online]. Available: http://en.wikipedia.org/wiki/List_of_countries_by_median_age.

[26] “Sunny Life Group in Japan.” [Online]. Available: http://www.sunnylife-group.co.jp/.

[27] “Best Life in Japan.” [Online]. Available: http://bestlife.jp/.

[28] H.-J. Yoo and C. van Hoof, *Bio-Medical CMOS ICs*. 2011, p. 2.

[29] M. Holland and L. Dunbrack, “Will Remote Health Monitoring Create a Paradigm Shift in Healthcare?,” *Health Industry Insights Newsflash IDC*, 2006. .

[30] O. Mendoza, “Patient-centered healthcare,” *Nat. Biotechnol.*, vol. 17, p. BV15, 1999.

[31] J. F. Stichler, “Patient-Centered Healthcare Design,” *JONA: The Journal of Nursing Administration*, vol. 41. pp. 503–506, 2011.

[32] “Milestones in AT&T History - 1968| History| AT&T.” [Online]. Available: http://www.corp.att.com/history/milestone_1968.html.

[33] “Mobile phone use passes milestone as UN report reveals global growth | Technology | The Guardian.” [Online]. Available: http://www.theguardian.com/technology/2009/mar/03/mobile-phones1.

[34] “Skin in the game.” [Online]. Available: https://usafamilymedicine.wordpress.com/2010/11/15/skin-in-the-game/.

[35] “When your carpet calls your doctor.” [Online]. Available: http://www.economist.com/node/15868133.

[36] A. Garingo, P. Friedlich, L. Tesoriero, S. Patil, P. Jackson, and I. Seri, “The use of mobile robotic telemedicine technology in the neonatal intensive care unit.,” *J. Perinatol.*, vol. 32, no. 1, pp. 55–63, Jan. 2012.

[37] M. J. Ball and J. Lillis, “E-health: transforming the physician/patient relationship.,” *Int. J. Med. Inform.*, vol. 61, no. 1, pp. 1–10, Apr. 2001.

[38] “Healthcare new entrants.” [Online]. Available: http://www.pwc.com/us/en/health-industries/healthcare-new-entrants.

[39] M. Eisenstein, “Miniature wireless sensors presage smart phone medicine.,” *Nat. Biotechnol.*, vol. 30, no. 11, pp. 1013–4, Nov. 2012.

[40] “Bureau of Health Professions (BHPR).” [Online]. Available: http://bhpr.hrsa.gov/.

[41] R. Vedanthan and V. Fuster, “Urgent need for human resources to promote global cardiovascular health.,” *Nat. Rev. Cardiol.*, vol. 8, no. 2, pp. 114–7, Feb. 2011.

[42] S. Xu, Y. Zhang, L. Jia, K. E. Mathewson, K. Jang, J. Kim, H. Fu, X. Huang, P. Chava, R. Wang, S. Bhole, L. Wang, Y. J. Na, Y. Guan, M. Flavin, Z. Han, Y. Huang, and J. A. Rogers, “Soft Microfluidic Assemblies of for the Skin,” *Science*, vol. 344, pp. 70–74, 2014.

[43] J. Cafazzo, K. Leonard, A. Easty, P. Rossos, and C. Chan, “Bridging the Self-care Deficit Gap: Remote Patient Monitoring and the Hospital-at-Home,” *Electron. Healthc.*, vol. 0001, pp. 66–73, 2009.

[44] H. P. Chase, J. A. Pearson, C. Wightman, M. D. Roberts, A. D. Oderberg, and S. K. Garg, “Modem transmission of glucose values reduces the costs and need for clinic visits.,” *Diabetes Care*, vol. 26, no. 5, pp. 1475–9, May 2003.

[45] A. Martínez, E. Everss, J. L. Rojo-Alvarez, D. P. Figal, and A. García-Alberola, “A systematic review of the literature on home monitoring for patients with heart failure.,” *J. Telemed. Telecare*, vol. 12, no. 5, pp. 234–41, Jan. 2006.

[46] A. Pantelopoulos and N. G. Bourbakis, “A Survey on Wearable Sensor-Based Systems for Health Monitoring and Prognosis,” *IEEE Trans. Syst. Man, Cybern. Part C (Applications Rev.*, vol. 40, no. 1, pp. 1–12, Jan. 2010.

[47] P. A. Reynolds, J. Harper, A. M. Jenner, and S. Dunne, “Better informed: an overview of health informatics.,” *Br. Dent. J.*, vol. 204, no. 5, pp. 259–64, Mar. 2008.

[48] N. Andre, S. Druart, P. Gerard, R. Pampin, L. Moreno-Hagelsieb, T. Kezai, L. A. Francis, D. Flandre, and J.-P. Raskin, “Miniaturized Wireless Sensing System for

Real-Time Breath Activity Recording," *IEEE Sens. J.*, vol. 10, no. 1, pp. 178–184, Jan. 2010.

[49] W. Raghupathi and V. Raghupathi, "Big data analytics in healthcare: promise and potential," *Heal. Inf. Sci. Syst.*, vol. 2, no. 1, p. 3, Feb. 2014.

[50] "Sierra Wireless - Connectivity for wireless telemedicine and telehealth." [Online]. Available: http://www.sierrawireless.com/Solutions/Industries/healthcare.aspx. [Accessed: 12-Jan-2015].

[51] "How The Internet Of Things Is Revolutionizing Healthcare." [Online]. Available: http://www.rfglobalnet.com/doc/how-revolutionizing-healthcare-0001. [Accessed: 12-Jan-2015].

[52] "Freescale Semiconductor | Embedded Processing Solutions." [Online]. Available: http://www.freescale.com/. [Accessed: 12-Jan-2015].

[53] P. Soontornpipit, C. M. Furse, and Y. C. Chung, "Design of implantable microstrip antenna for communication with medical implants," *IEEE Trans. Microw. Theory Tech.*, vol. 52, pp. 1944–1951, 2004.

[54] J. Kim and Y. Rahmat-Samii, "Implanted antennas inside a human body: Simulations, designs, and characterizations," *IEEE Trans. Microw. Theory Tech.*, vol. 52, pp. 1934–1943, 2004.

[55] H. A. Wheeler, "Fundamental Limitations of Small Antennas," *Proc. IRE*, vol. 35, 1947.

[56] J. S. McLean, "A re-examination of the fundamental limits on the radiation q of electrically small antennas," *IEEE Trans. Antennas Propag.*, vol. 44, pp. 672–676, 1996.

[57] L. J. Chu, "Physical Limitations of Omni-Directional Antennas," *J. Appl. Phys.*, vol. 19, no. 12, p. 1163, Jan. 1948.

[58] R. C. Hansen, "FUNDAMENTAL LIMITATIONS IN ANTENNAS.," *Proceedings of the IEEE*, vol. 69. pp. 170–182, 1981.

[59] "AnandTech | Apple's iPhone 4: Thoroughly Reviewed." [Online]. Available: http://www.anandtech.com/show/3794/the-iphone-4-review/2.

[60] P. M. Izdebski, H. Rajagopalan, and Y. Rahmat-Samii, “Conformal ingestible capsule antenna: A novel chandelier meandered design,” *IEEE Trans. Antennas Propag.*, vol. 57, pp. 900–909, 2009.

[61] H. Rajagopalan, P. Izdebski, and Y. Rahmat-Samii, “A miniaturized ingestible antenna for capsule medical imaging system,” in *IEEE Antennas and Propagation Society, AP-S International Symposium (Digest)*, 2009.

[62] “Cockrell School Unveils First-of-its Kind 3-D Printing Vending Machine.” [Online]. Available: http://www.engr.utexas.edu/features/innovation-station.

[63] H. D. Foltz, J. S. McLean, and G. Crook, “Disk-loaded monopoles with parallel strip elements,” *IEEE Trans. Antennas Propag.*, vol. 46, pp. 1894–1896, 1998.

[64] E. E. Altshuler, “Electrically small self-resonant wire antennas optimized using a genetic algorithm,” *IEEE Trans. Antennas Propag.*, vol. 50, pp. 297–300, 2002.

[65] J. A. Dobbins and R. L. Rogers, “Folded conical helix antenna,” *IEEE Trans. Antennas Propag.*, vol. 49, pp. 1777–1781, 2001.

[66] C. Friedman, “Wide-band matching of a small disk-loaded monopole,” *IEEE Transactions on Antennas and Propagation*, vol. 33. pp. 1142–1148, 1985.

[67] S. R. Best, “The radiation properties of electrically small folded spherical helix antennas,” *IEEE Trans. Antennas Propag.*, vol. 52, pp. 953–960, 2004.

[68] S. Y. Lee, M. Y. Su, M. C. Liang, Y. Y. Chen, C. H. Hsieh, C. M. Yang, H. Y. Lai, J. W. Lin, and Q. Fang, “A programmable implantable microstimulator soc with wireless telemetry: Application in closed-loop endocardial stimulation for cardiac pacemaker,” in *IEEE Transactions on Biomedical Circuits and Systems*, 2011, vol. 5, pp. 511–522.

[69] A. S. Y. Poon, S. O’driscoll, and T. H. Meng, “Optimal frequency for wireless power transmission into dispersive tissue,” in *IEEE Transactions on Antennas and Propagation*, 2010, vol. 58, pp. 1739–1750.

[70] “NEC2.” [Online]. Available: http://www.nec2.org/.

[71] “Rapid Prototyping.” [Online]. Available: http://www.nsf.gov/about/history/nsf0050 /manufacturing/rapid.htm.

[72] C. Deckard, “Method and apparatus for producing parts by selective sintering,” *US Pat. 4,863,538*, 1989.

[73] J. J. Adams, E. B. Duoss, T. F. Malkowski, M. J. Motala, B. Y. Ahn, R. G. Nuzzo, J. T. Bernhard, and J. A. Lewis, “Conformal printing of electrically small antennas on three-dimensional surfaces,” *Adv. Mater.*, vol. 23, pp. 1335–1340, 2011.

[74] C. Pfeiffer, A. Grbic, X. Xu, and S. R. Forrest, “Novel methods to analyze and fabricate electrically small antennas,” in *IEEE Antennas and Propagation Society, AP-S International Symposium (Digest)*, 2011, pp. 761–764.

[75] G. Zhou, “A non-uniform pitch dual band helix antenna,” *IEEE Antennas Propag. Soc. Int. Symp. Transm. Waves Prog. to Next Millenn. 2000 Dig. Held conjunction with Usn. Natl. Radio Sci. Meet. (C*, vol. 1, 2000.

[76] I. Egorov and Z. Y. Z. Ying, “A non-uniform helical antenna for dual-band cellular phones,” *IEEE Antennas Propag. Soc. Int. Symp. Transm. Waves Prog. to Next Millenn. 2000 Dig. Held conjunction with Usn. Natl. Radio Sci. Meet. (C*, vol. 2, 2000.

[77] C. A. Balanis, *Antenna Theory: Analysis and Design, 3rd Edition*, 3rd Editio. Wiley, 2005.

[78] “IT IS Virtual Population.” [Online]. Available: http://www.itis.ethz.ch/.

[79] “SEMCAD X.” [Online]. Available: http://www.speag.com/products/semcad/.

[80] R. S. Kerbel and B. A. Kamen, “The anti-angiogenic basis of metronomic chemotherapy.,” *Nat. Rev. Cancer*, vol. 4, pp. 423–436, 2004.

[81] D. Fine, A. Grattoni, E. Zabre, F. Hussein, M. Ferrari, and X. Liu, “A low-voltage electrokinetic nanochannel drug delivery system.,” *Lab Chip*, vol. 11, pp. 2526–2534, 2011.

[82] D. Fine, A. Grattoni, S. Hosali, A. Ziemys, E. De Rosa, J. Gill, R. Medema, L. Hudson, M. Kojic, M. Milosevic, L. Brousseau Iii, R. Goodall, M. Ferrari, and X. Liu, “A robust nanofluidic membrane with tunable zero-order release for implantable dose specific drug delivery.,” *Lab Chip*, vol. 10, pp. 3074–3083, 2010.

[83] S. P. Woods and T. G. Constandinou, “Wireless capsule endoscope for targeted drug delivery: Mechanics and design considerations,” *IEEE Transactions on Biomedical Engineering*, vol. 60. pp. 945–953, 2013.

[84] S. Rahimi, E. H. Sarraf, G. K. Wong, and K. Takahata, “Implantable drug delivery device using frequency-controlled wireless hydrogel microvalves,” *Biomed. Microdevices*, vol. 13, pp. 267–277, 2011.

[85] I. Mansoor, U. O. Häfeli, and B. Stoeber, “Arrays of solvent cast hollow out-of-plane polymer microneedles for drug delivery,” in *Proceedings of the IEEE International Conference on Micro Electro Mechanical Systems (MEMS)*, 2011, pp. 1027–1030.

[86] Y. J. Yang, Y. J. Huang, H. H. Liao, T. Wang, P. L. Huang, C. W. Lin, Y. H. Wang, and S. S. Lu, “A release-on-demand wireless CMOS drug delivery SoC based on electrothermal activation technique,” in *Digest of Technical Papers - IEEE International Solid-State Circuits Conference*, 2009.

[87] J. R. Rajian, M. L. Fabiilli, J. B. Fowlkes, P. L. Carson, and X. Wang, “Drug delivery monitoring by photoacoustic tomography with an ICG encapsulated double emulsion,” *Optics Express*, vol. 19. p. 14335, 2011.

[88] D. J. Lurie and K. Mäder, “Monitoring drug delivery processes by EPR and related techniques - Principles and applications,” *Advanced Drug Delivery Reviews*, vol. 57. pp. 1171–1190, 2005.

[89] R. Weinstain, E. Segal, R. Satchi-Fainaro, and D. Shabat, “Real-time monitoring of drug release.,” *Chem. Commun. (Camb).*, vol. 46, pp. 553–555, 2010.

[90] “Ionto Patch.” [Online]. Available: http://www.iontopatch.com/.

[91] “Empi Action Patch.” [Online]. Available: http://www.empi.com/.

[92] “SmartPill.” [Online]. Available: http://www.smartpillcorp.com/.

[93] “Philips iPill.” [Online]. Available: http://www.research.philips.com/.

[94] “MicroCHIPS.” [Online]. Available: http://www.mchips.com/.

[95] N. Cho, J. Bae, and H. J. Yoo, “A 10.8 mW body channel communication/MICS dual-band transceiver for a unified body sensor network controller,” in *IEEE Journal of Solid-State Circuits*, 2009, vol. 44, pp. 3459–3468.

[96] B. Bianco, G. P. Drago, M. Marchesi, C. Martini, G. S. Mela, and S. Ridella, “Measurements of Complex Dielectric Constant of Human Sera and Erythrocytes,” *IEEE Trans. Instrum. Meas.*, vol. 28, 1979.

[97] D. M Pozar, *Microwave Engineering, 3rd*. 2005, p. 728.

[98] "Ansys HFSS." [Online]. Available: http://www.ansys.com/.

[99] H. Huang, K. Nieman, Y. Hu, and D. Akinwande, "Electrically small folded ellipsoidal helix antenna for medical implant applications," in *IEEE Antennas and Propagation Society, AP-S International Symposium (Digest)*, 2011, pp. 769–771.

[100] H. Huang, K. Nieman, P. Y. Chen, M. Ferrari, Y. Hu, and D. Akinwande, "Properties and applications of electrically small folded ellipsoidal helix antenna," *IEEE Antennas Wirel. Propag. Lett.*, vol. 11, pp. 678–681, 2012.

[101] L. Guo, K. W. Meacham, S. Hochman, and S. P. DeWeerth, "A PDMS-based conical-well microelectrode array for surface stimulation and recording of neural tissues," *IEEE Trans. Biomed. Eng.*, vol. 57, pp. 2485–2494, 2010.

[102] J. P. Curty, N. Joehl, C. Dehollain, and M. J. Declercq, "Remotely powered addressable UHF RFID integrated system," *IEEE J. Solid-State Circuits*, vol. 40, pp. 2193–2202, 2005.

[103] A. Rida, L. Yang, and M. Tentzeris, *RFID-Enabled Sensor Design and Applications*. Artech House, 2010, p. 212.

[104] S. DeWit, *Fundamental Concepts and Skills for Nursing*, 4th editio. Saunders, 2013, p. 960.

[105] P. Griffin, P. A. Potter, and W. Ostendorf, *Clinical Nursing Skills and Techniques*, 8th editio. Mosby, 2013, p. 1216.

[106] D. Fine, A. Grattoni, E. Zabre, F. Hussein, M. Ferrari, and X. Liu, "A low-voltage electrokinetic nanochannel drug delivery system.," *Lab Chip*, vol. 11, no. 15, pp. 2526–34, Aug. 2011.

[107] Yao-Joe Yang, Yu-Jie Huang, Hsin-Hung Liao, Tao Wang, Pen-Li Huang, Chii-Wan Lin, Yao-Hong Wang, and Shey-Shi Lu, "A release-on-demand wireless CMOS drug delivery SoC based on electrothermal activation technique," in *2009 IEEE International Solid-State Circuits Conference - Digest of Technical Papers*, 2009, pp. 288–289,289a.

[108] S. Rahimi, E. H. Sarraf, G. K. Wong, and K. Takahata, "Implantable drug delivery device using frequency-controlled wireless hydrogel microvalves.," *Biomed. Microdevices*, vol. 13, no. 2, pp. 267–77, Apr. 2011.

[109] H. Huang, P. Zhao, P.-Y. Chen, Y. Ren, X. Liu, M. Ferrari, Y. Hu, and D. Akinwande, “RFID Tag Helix Antenna Sensors for Wireless Drug Dosage Monitoring,” *IEEE J. Transl. Eng. Heal. Med.*, vol. 2, pp. 1–8, 2014.

[110] J. R. Rajian, M. L. Fabiilli, J. B. Fowlkes, P. L. Carson, and X. Wang, “Drug delivery monitoring by photoacoustic tomography with an ICG encapsulated double emulsion.,” *Opt. Express*, vol. 19, no. 15, pp. 14335–47, Jul. 2011.

[111] V. Philips, “Future of Healthcare: How Passive Sensors Will Support Patient Care Between Visits,” *Sensors by California HealthCare Foundation*, 2013.

[112] H. Kang, H. Park, Y. Park, M. Jung, B. C. Kim, G. Wallace, and G. Cho, “Fully roll-to-roll gravure printable wireless (13.56 MHz) sensor-signage tags for smart packaging.,” *Sci. Rep.*, vol. 4, p. 5387, 2014.

[113] J. Sidén, X. Zeng, T. Unander, A. Koptyug, and H. E. Nilsson, “Remote moisture sensing utilizing ordinary RFID tags,” in *Proceedings of IEEE Sensors*, 2007, pp. 308–311.

[114] S. Kim, C. Mariotti, F. Alimenti, P. Mezzanotte, A. Georgiadis, A. Collado, L. Roselli, and M. M. Tentzeris, “No Battery Required: Perpetual RFID-Enabled Wireless Sensors for Cognitive Intelligence Applications,” *IEEE Microw. Mag.*, vol. 14, no. 5, pp. 66–77, Jul. 2013.

[115] V. Lakafosis, A. Rida, R. Vyas, L. Yang, S. Nikolaou, and M. M. Tentzeris, “Progress Towards the First Wireless Sensor Networks Consisting of Inkjet-Printed, Paper-Based RFID-Enabled Sensor Tags,” *Proc. IEEE*, vol. 98, no. 9, pp. 1601–1609, Sep. 2010.

[116] R. Vyas, V. Lakafosis, A. Rida, N. Chaisilwattana, S. Travis, J. Pan, and M. M. Tentzeris, “Paper-Based RFID-Enabled Wireless Platforms for Sensing Applications,” *IEEE Trans. Microw. Theory Tech.*, vol. 57, no. 5, pp. 1370–1382, May 2009.

[117] R. Bhattacharyya, C. Floerkemeier, and S. Sarma, “RFID tag antenna based sensing: Does your beverage glass need a refill?,” in *2010 IEEE International Conference on RFID (IEEE RFID 2010)*, 2010, pp. 126–133.

[118] R. Bhattacharyya, C. Floerkemeier, and S. Sarma, “Low-Cost, Ubiquitous RFID-Tag-Antenna-Based Sensing,” *Proc. IEEE*, vol. 98, no. 9, pp. 1593–1600, Sep. 2010.

[119] P.-Y. Chen, F. Monticone, and A. Alu, “Suppressing the Electromagnetic Scattering With an Helical Mantle Cloak,” *IEEE Antennas Wirel. Propag. Lett.*, vol. 10, pp. 1598–1601, 2011.

[120] R. W. Ziolkowski and A. D. Kipple, “Application of double negative materials to increase the power radiated by electrically small antennas,” *IEEE Trans. Antennas Propag.*, vol. 51, no. 10, pp. 2626–2640, Oct. 2003.

[121] R. Fleury, J. Soric, and A. Alu, “Physical Bounds on Absorption and Scattering for Cloaked Sensors,” *Phys. Rev. B*, vol. 89, p. 045122, Sep. 2013.

[122] J. R. Riley, A. D. Smith, D. R. Reynolds, A. S. Edwards, J. L. Osborne, I. H. Williams, N. L. Carreck, and G. M. Poppy, “Tracking bees with harmonic radar,” *Nature*, vol. 379, no. 6560, pp. 29–30, Jan. 1996.

[123] R. Bhattacharyya, C. Floerkemeier, S. Sarma, and D. Deavours, “RFID tag antenna based temperature sensing in the frequency domain,” in *2011 IEEE International Conference on RFID*, 2011, pp. 70–77.

[124] N. Jones, “Computer science: The learning machines.,” *Nature*, vol. 505, no. 7482, pp. 146–8, Jan. 2014.

[125] D. H. Ballard, G. E. Hinton, and T. J. Sejnowski, “Parallel visual computation,” *Nature*, vol. 306, no. 5938, pp. 21–26, Nov. 1983.

[126] P.-Y. Chen and A. Alù, “Mantle cloaking using thin patterned metasurfaces,” *Phys. Rev. B*, vol. 84, no. 20, p. 205110, Nov. 2011.

[127] H. R. Stuart and A. Pidwerbetsky, “Electrically small antenna elements using negative permittivity resonators,” in *2005 IEEE Antennas and Propagation Society International Symposium*, 2005, vol. 1A, pp. 676–679.

[128] “CST MICROWAVE STUDIO.” [Online]. Available: https://www.cst.com/Products/CSTmws.

[129] N. Engheta, A. Salandrino, and A. Alù, “Circuit Elements at Optical Frequencies: Nanoinductors, Nanocapacitors, and Nanoresistors,” *Phys. Rev. Lett.*, vol. 95, no. 9, p. 095504, Aug. 2005.

[130] R. W. Ziolkowski, “Efficient electrically small antenna facilitated by a near-field resonant parasitic,” *IEEE Antennas Wirel. Propag. Lett.*, vol. 7, pp. 581–584, 2008.

[131] Y. Liao, T. H. Hubing, and D. Su, “Equivalent Circuit for Dipole Antennas in a Lossy Medium,” *IEEE Trans. Antennas Propag.*, vol. 60, no. 8, pp. 3950–3953, Aug. 2012.

[132] K. H. H. T. Su C., “A simplified model for Normal mode helical antennas,” *Appl. Comput. Electromagn. Soc. J.*, vol. 25, pp. 32–40, 2010.

[133] “Advanced Design System (ADS) | Keysight (formerly Agilent Test and Measurement).”

[134] “MiniCircuit MK-5 Frequency Multiplier.” [Online]. Available: http://www.minicircuits.com/pdfs/MK-5.pdf.

[135] “Class 1 Generation 2 UHF Air Interface Protocol Standard.” [Online]. Available: http://www.gs1.org/gsmp/kc/epcglobal/uhfc1g2.

[136] K. S. Novoselov, A. K. Geim, S. V Morozov, D. Jiang, Y. Zhang, S. V Dubonos, I. V Grigorieva, and A. A. Firsov, “Electric field effect in atomically thin carbon films.,” *Science*, vol. 306, pp. 666–669, 2004.

[137] P. G. Collins, “Extreme Oxygen Sensitivity of Electronic Properties of Carbon Nanotubes,” *Science,* vol. 287, pp. 1801–1804, 2000.

[138] A. K. Geim and K. S. Novoselov, “The rise of graphene.,” *Nat. Mater.*, vol. 6, pp. 183–191, 2007.

[139] J. Kong, N. Franklin, C. Zhou, M. Chapline, S. Peng, K. Cho, and H. Dai, “Nanotube Molecular Wires as Chemical Sensors,” *Science*, vol. 287, pp. 622–625, 2000.

[140] M. S. Mannoor, H. Tao, J. D. Clayton, A. Sengupta, D. L. Kaplan, R. R. Naik, N. Verma, F. G. Omenetto, and M. C. McAlpine, “Graphene-based wireless bacteria detection on tooth enamel,” *Nat. Commun.*, vol. 3, p. 763, 2012.

[141] F. Schedin, A. K. Geim, S. V Morozov, E. W. Hill, P. Blake, M. I. Katsnelson, and K. S. Novoselov, “Detection of individual gas molecules adsorbed on graphene.,” *Nat. Mater.*, vol. 6, pp. 652–655, 2007.

[142] C. A. Merchant, K. Healy, M. Wanunu, V. Ray, N. Peterman, J. Bartel, M. D. Fischbein, K. Venta, Z. Luo, A. T. C. Johnson, and M. Drndić, “DNA translocation through graphene nanopores.,” *Nano Lett.*, vol. 10, no. 8, pp. 2915–21, Aug. 2010.

[143] T. Le, T. Thai, V. Lakafosis, M. Tentzeris, Z. Lin, Y. Fang, K. Sandhage, and C. Wong, “Graphene enhanced wireless sensors,” *IEEE Sensors*, pp. 1–4, Oct. 2012.

[144] A. McWilliams, “Graphene: Technologies, Applications and Markets,” *BCC Res. Mark. Forecast.*, 2013.

[145] J. G. Proakis and M. Salehi, *Wireless Communications: Principles and Practice*. Prentice Hall; 2 edition, 2002.

[146] T. S. Rappaport, *Communication Systems Engineering*. Prentice Hall; 2 edition, 2001.

[147] Y. W. Bai and C. L. Chiang, “Design and implementation of the integration applications for a portable MP3 player with a Bluetooth hand-free/set,” *IEEE Trans. Consum. Electron.*, vol. 51, pp. 849–855, 2005.

[148] F. Schwierz, “Electronics: industry-compatible graphene transistors.,” *Nature*, vol. 472, no. 7341, pp. 41–2, Apr. 2011.

[149] D. Akinwande, G. F. Close, S. Yasuda, B. Paul, S. Fujita, and H.-S. P. Wong, “High-speed graphene interconnects monolithically integrated with CMOS ring oscillators operating at 1.3GHz,” *2009 IEEE Int. Electron Devices Meet.*, pp. 1–4, Dec. 2009.

[150] T. Palacios, A. Hsu, and H. Wang, “Applications of graphene devices in RF communications,” *IEEE Commun. Mag.*, vol. 48, pp. 122–128, 2010.

[151] H. Wang, D. Nezich, J. Kong, and T. Palacios, “Graphene frequency multipliers,” *IEEE Electron Device Lett.*, vol. 30, pp. 547–549, 2009.

[152] H. Wang, A. Hsu, J. Wu, J. Kong, and T. Palacios, “Graphene-based ambipolar RF mixers,” *IEEE Electron Device Lett.*, vol. 31, pp. 906–908, 2010.

[153] M. E. Ramn, K. N. Parrish, S. F. Chowdhury, C. W. Magnuson, H. C. P. Movva, R. S. Ruoff, S. K. Banerjee, and D. Akinwande, “Three-gigahertz graphene frequency doubler on quartz operating beyond the transit frequency,” *IEEE Trans. Nanotechnol.*, vol. 11, pp. 877–883, 2012.

[154] S. Lee, K. Lee, C.-H. Liu, G. S. Kulkarni, and Z. Zhong, “Flexible and transparent all-graphene circuits for quaternary digital modulations,” *Nat. Commun.*, vol. 3, p. 1018, 2012.

[155] Z. Cheng, Q. Li, Z. Li, Q. Zhou, and Y. Fang, "Suspended graphene sensors with improved signal and reduced noise," *Nano Lett.*, vol. 10, pp. 1864–1868, 2010.

[156] J. D. Fowler, M. J. Allen, V. C. Tung, Y. Yang, R. B. Kaner, and B. H. Weiller, "Practical chemical sensors from chemically derived graphene," *ACS Nano*, vol. 3, pp. 301–306, 2009.

[157] Y. Dan, Y. Lu, N. J. Kybert, Z. Luo, and A. T. C. Johnson, "Intrinsic response of graphene vapor sensors," *Nano Lett.*, vol. 9, pp. 1472–1475, 2009.

[158] Y. Ohno, K. Maehashi, Y. Yamashiro, and K. Matsumoto, "Electrolyte-gated graphene field-effect transistors for detecting ph and protein adsorption," *Nano Lett.*, vol. 9, pp. 3318–3322, 2009.

[159] Z. Cheng, Q. Zhou, C. Wang, Q. Li, C. Wang, and Y. Fang, "Toward intrinsic graphene surfaces: A systematic study on thermal annealing and wet-chemical treatment of SiO2-supported graphene devices," *Nano Lett.*, vol. 11, pp. 767–771, 2011.

[160] D.-W. Shin, H. M. Lee, S. M. Yu, K.-S. Lim, J. H. Jung, M.-K. Kim, S.-W. Kim, J.-H. Han, R. S. Ruoff, and J.-B. Yoo, "A facile route to recover intrinsic graphene over large scale.," *ACS Nano*, vol. 6, no. 9, pp. 7781–8, Sep. 2012.

[161] K. N. Parrish and D. Akinwande, "An exactly solvable model for the graphene transistor in the quantum capacitance limit," *Appl. Phys. Lett.*, vol. 101, 2012.

[162] K. N. Parrish, "Nanoscale graphene for RF circuits and systems," PhD. Dissertation, the University of Texas at Austin, 2013.

[163] K. N. Parrish and D. Akinwande, "Impact of contact resistance on the transconductance and linearity of graphene transistors," *Appl. Phys. Lett.*, vol. 98, 2011.

[164] L. Tao, J. Lee, H. Li, R. D. Piner, R. S. Ruoff, and D. Akinwande, "Inductively heated synthesized graphene with record transistor mobility on oxidized silicon substrates at room temperature," *Appl. Phys. Lett.*, vol. 103, 2013.

[165] A. K. M. Newaz, Y. S. Puzyrev, B. Wang, S. T. Pantelides, and K. I. Bolotin, "Probing charge scattering mechanisms in suspended graphene by varying its dielectric environment," *Nature Communications*, vol. 3. p. 734, 2012.

[166] L. Tao, J. Lee, H. Chou, M. Holt, R. S. Ruoff, and D. Akinwande, “Synthesis of high quality monolayer graphene at reduced temperature on hydrogen-enriched evaporated copper (111) films,” *ACS Nano*, vol. 6, pp. 2319–2325, 2012.

[167] L. Tao, J. Lee, M. Holt, H. Chou, S. J. McDonnell, D. A. Ferrer, M. G. Babenco, R. M. Wallace, S. K. Banerjee, R. S. Ruoff, and D. Akinwande, “Uniform wafer-scale chemical vapor deposition of graphene on evaporated Cu (111) film with quality comparable to exfoliated monolayer,” *J. Phys. Chem. C*, vol. 116, pp. 24068–24074, 2012.

[168] R. Piner, H. Li, X. Kong, L. Tao, I. N. Kholmanov, H. Ji, W. H. Lee, J. W. Suk, J. Ye, Y. Hao, S. Chen, C. W. Magnuson, A. F. Ismach, D. Akinwande, and R. S. Ruoff, “Graphene synthesis via magnetic inductive heating of copper substrates,” *ACS Nano*, vol. 7, pp. 7495–7499, 2013.

[169] H. Wang, Y. Wu, C. Cong, J. Shang, and T. Yu, “Hysteresis of electronic transport in graphene transistors,” *ACS Nano*, vol. 4, pp. 7221–7228, 2010.

[170] M. Lafkioti, B. Krauss, T. Lohmann, U. Zschieschang, H. Klauk, K. V. Klitzing, and J. H. Smet, “Graphene on a hydrophobic substrate: Doping reduction and hysteresis suppression under ambient conditions,” *Nano Lett.*, vol. 10, pp. 1149–1153, 2010.

[171] P. L. Levesque, S. S. Sabri, C. M. Aguirre, J. Guillemette, M. Siaj, P. Desjardins, T. Szkopek, and R. Martel, “Probing charge transfer at surfaces using graphene transistors,” *Nano Lett.*, vol. 11, pp. 132–137, 2011.

[172] A. K. M. Newaz, Y. S. Puzyrev, B. Wang, S. T. Pantelides, and K. I. Bolotin, “Probing charge scattering mechanisms in suspended graphene by varying its dielectric environment,” *Nat. Commun.*, vol. 3, p. 734, 2012.

[173] D. W. Shin, H. M. Lee, S. M. Yu, K. S. Lim, J. H. Jung, M. K. Kim, S. W. Kim, J. H. Han, R. S. Ruoff, and J. B. Yoo, “A facile route to recover intrinsic graphene over large scale,” *ACS Nano*, vol. 6, pp. 7781–7788, 2012.

[174] P. Brodin, I. Rosenkrands, P. Andersen, S. T. Cole, and R. Brosch, “ESAT-6 proteins: Protective antigens and virulence factors?,” *Trends Microbiol.*, vol. 12, pp. 500–508, 2004.

[175] M. A. Pillai, S. Veerasingam, and D. Yaswanth Sai, “CAN based smart sensor network for indoor air quality monitoring,” *2010 3rd Int. Conf. Comput. Sci. Inf. Technol.*, vol. 8, pp. 456–460, Jul. 2010.

[176] T. E. McKone, P. B. Ryan, and H. Ozkaynak, “Exposure information in environmental health research: current opportunities and future directions for particulate matter, ozone, and toxic air pollutants.,” *J. Expo. Sci. Environ. Epidemiol.*, vol. 19, no. 1, pp. 30–44, Jan. 2009.

[177] B. Predic, Z. Yan, J. Eberle, D. Stojanovic, and K. Aberer, “ExposureSense: Integrating daily activities with air quality using mobile participatory sensing,” *2013 IEEE Int. Conf. Pervasive Comput. Commun. Work. (PERCOM Work.*, pp. 303–305, Mar. 2013.

[178] Y. Xiang, R. Piedrahita, R. P. Dick, M. Hannigan, Q. Lv, and L. Shang, “A Hybrid Sensor System for Indoor Air Quality Monitoring,” *2013 IEEE Int. Conf. Distrib. Comput. Sens. Syst.*, pp. 96–104, May 2013.

[179] J. M. Boyce, “Hand hygiene compliance monitoring: current perspectives from the USA.,” *J. Hosp. Infect.*, vol. 70 Suppl 1, pp. 2–7, Oct. 2008.

[180] A. I. Levchenko, G. C. Hufton, V. M. Boscart, and G. R. Fernie, “Embedded System for Hygiene Compliance Monitoring,” *IEEE Trans. Autom. Sci. Eng.*, vol. 7, no. 3, pp. 695–698, Jul. 2010.